STM investigation of defects, charge density wave and superconductivity in 1T -CuxTiSe2 (0 ≤ x ≤ 0.07)

Novello, Anna Maria

UNIVERSITÉ DE GENÈVE
Département de Physique
de la Matière Quantique

FACULTÉ DES SCIENCES
Professeur Ch. Renner

STM investigation of defects, charge density wave and superconductivity in $1T$-Cu_xTiSe_2 ($0 \leq x \leq 0.07$)

THÈSE

présentée à la Faculté des Sciences
de l'Université de Genève
pour obtenir le grade de docteur ès Sciences,
mention Physique

par

Anna Maria Novello

de Udine (Italie)

Thèse N° 4832

GENÈVE
Atelier d'impression ReproMail
2015

UNIVERSITÉ
DE GENÈVE

FACULTÉ DES SCIENCES

Doctorat ès sciences
Mention physique

Thèse de *Madame Anna Maria NOVELLO*

intitulée :

"STM Investigation of Defects, charge Density Wave and Superconductivity in 1T-Cu_xTiSe_2 ($0 \leq x \leq 0.07$)"

La Faculté des sciences, sur le préavis de Monsieur Ch. RENNER, professeur ordinaire et directeur de thèse (Département de physique de la matière quantique), Monsieur F. BAUMBERGER, professeur ordinaire (Département de physique de la matière quantique), Monsieur I. MAGGIO-APRILE, docteur (Département de physique de la matière quantique) et Monsieur D. RODITCHEV, professeur (Institut des NanoSciences de Paris, Université Pierre et Marie Curie, Paris, France), autorise l'impression de la présente thèse, sans exprimer d'opinion sur les propositions qui y sont énoncées.

Genève, le 28 septembre 2015

Thèse - 4832 -

Le Doyen

To my family

Résumé

La supraconductivité est un phénomène découvert en 1911, ayant pour caractéristiques une perte totale de résistivité électrique et l'expulsion du champ magnétique dans certains matériaux, lorsqu'ils sont refroidis en dessous d'une certaine température "critique". Cette découverte a déjà été exploitée dans certaines applications pratiques comme, par exemple, les aimants supraconducteurs utilisés pour la résonance magnétique. Toutefois, de très basses températures sont encore nécessaires pour que ce phénomène se manifeste efficacement.

La découverte de la supraconductivité à haute température dans les cuprates a marqué une étape importante en direction de la supraconductivité à température ambiante, lorsque la limite théorique de température de $\sim$ 30 K a été franchie en 1986. Depuis cette découverte beaucoup d'efforts ont été faits pour comprendre le mécanisme à la base de cette nouvelle forme de supraconductivité.

Les cuprates révèlent un diagramme de phase très riche avec plusieurs états fondamentaux qui apparaissent en fonction de la température, du dopage ou de la pression. Une des nombreuses questions ouvertes est le lien entre la supraconductivité et ce qu'on appelle les ondes de densité de charge. Ces ondes apparaissent dans certains métaux au-dessous d'une température critique, lorsque les électrons interagissent avec un réseau périodique, avec pour conséquence une redistribution de leur densité et la formation de "vagues électroniques".

Observées depuis deux décennies dans plusieurs membres de la famille des cuprates, l'idée que la présence des ondes de densité de charge puisse être une propriété commune à tous les supraconducteurs à haute température commence actuellement à se développer, sans qu'il soit encore clairement établi s'il y a coexistence, compétition ou coopération de ce phénomène avec la supraconductivité.

Étant donné que la supraconductivité et les ondes de densité de charge sont des phénomènes également observés dans d'autres classes de matériaux, l'idée à la base de ce travail de thèse est l'étude d'un

composé dont le diagramme de phase présente les deux transitions, tout en se révélant être plus simple que celui des cuprates. Pour cette raison, notre choix s'est porté sur des monocristaux de la famille des dichalcogénures de métaux de transition, en particulier le $1T$-Cu_xTiSe_2 ($0 \leq x \leq 0.07$). Dans sa forme pure (x=0), ce matériau présente une transition d'ondes de densité de charge à 200 K. Cette température peut être réduite par l'introduction de cuivre, qui provoque également l'apparition de la supraconductivité à une température de transition maximale de 4.1 K (x=0.08). Comme la majorité de dichalcogénures de métaux de transition, la structure du $1T$-Cu_xTiSe_2 consiste en un empilement de feuillets constitués par une couche de métal de transition entourée de deux couches de chalcogènes (éléments de la colonne de l'oxygène ou groupe 16: soufre, sélénium ou tellure). Chaque feuillet est lié au suivant par de faibles liaisons de type van der Waals. Cette structure permet non seulement l'intercalation d'autres types d'atomes, mais également un clivage facile, ce qui rend possible la préparation de surfaces propres ou la fabrication d'échantillons qui ont seulement quelques couches atomiques d'épaisseur (ordre de $10^{-9}m$). Pour notre étude, nous avons utilisé un microscope à effet tunnel qui permet d'étudier des surfaces avec une résolution atomique.

Dans ce travail, nous avons tout d'abord identifié, avec l'aide de calculs théoriques, les différents types de défauts atomiques visibles à la surface de monocristaux purs, nous conduisant à une interprétation différente de ce qui était reconnu précédemment dans la littérature. Grâce à cette identification méticuleuse, nous avons établi que la surface visualisée par le microscope à effet tunnel est précisément le feuillet supérieur de sélénium, prouvant ainsi qu'une étude détaillée des défauts peut fournir des informations importantes sur la structure du matériau et peut aider à l'identification du polytype du cristal. Une approche similaire à été utilisée pour les monocristaux intercalés au cuivre, où nous avons pu reconnaître la signature des atomes de cuivre et relever leur position exacte dans la structure cristalline. Grâce à ce résultat, il est désormais possible d'établir avec précision la concentration locale de dopants. Nous avons ensuite étudié l'influence de ces défauts sur les ondes de densité de charge, en rassemblant des informations qui pourraient s'avérer également utiles dans la compréhension de l'origine de ces ondes dans ce matériau. Nous avons montré que les défauts intrinsèques n'ont pas un fort effet sur les ondes de densité de charge, tandis que les atomes de cuivre perturbent ces ondes même à très faibles concentrations (1%). Dans ce cas on assiste à l'apparition d'ondes de charge unidimensionnelles (*stripes*) en lieu et place de la redistribution de charge habituelle, ce qui implique un

diagramme de phase plus riche que prévu. De plus, la distribution désordonnée des atomes de cuivre est à l'origine de la formation de domaines d'ondes de densité de charge, qui survivent à des concentrations de cuivre supérieures à 4%. Enfin, nous avons effectué des mesures préliminaires dans la phase supraconductrice pour étudier le rôle du désordre (dû à la présence des défauts intrinsèques et à une distribution de cuivre irrégulière) et des domaines des ondes de densité de charge sur la supraconductivité. Nos mesures de spectroscopie du *gap* d'énergie sont compatibles avec la théorie standard de la supraconductivité décrite par Bardeen, Cooper et Shrieffer dans les années '50 pour les supraconducteurs à basse température, et en accord avec la littérature. De plus ce *gap* d'énergie ne disparaît pas en présence des domaines d'ondes de densité de charge. Tous les résultats obtenus dans ce travail montrent comment ce matériau peut être utilisé dans l'étude des effets induits par les défauts et les impuretés sur les ondes de densité de charge ou sur la supraconductivité, et comment ces différents phénomènes interagissent.

Contents

1 Introduction **1**

2 Theoretical Background **5**
2.1 Charge Density Wave Formation 5
2.1.1 The lattice instability 7
2.1.2 The electronic instability 8
2.1.3 The gap in the electronic spectrum 9
2.1.4 From 1D to 2D systems 10
2.2 Superconductivity basics 12
2.2.1 The BCS theory and the superconducting gap . . 12
2.2.2 Beyond BCS superconductors 14
2.3 Conclusions 16

3 The family of Transition Metal Dichalcogenides and two case studies: $1T$-$TiSe_2$ and $1T$-Cu_xTiSe_2 **17**
3.1 TMD family 17
3.2 $1T$-$TiSe_2$ 18
3.2.1 $1T$-$TiSe_2$: phase transitions 20
3.3 $1T$-Cu_xTiSe_2 23
3.3.1 $1T$-Cu_xTiSe_2: normal state 23
3.3.2 $1T$-Cu_xTiSe_2: CDW transition 24
3.3.3 $1T$-Cu_xTiSe_2: superconducting transition 25
3.3.4 $1T$-Cu_xTiSe_2: the phase diagram 26
3.4 Conclusion 27

4 Basic principles of Scanning Tunneling Microscopy and Spectroscopy **29**
4.1 Electron tunneling 29
4.2 Theory of tunneling 30
4.2.1 Tunneling current 32
4.2.2 Bardeen's tunneling matrix 32

4.2.3 The differential conductance and the LDOS . . . 34
4.3 Conclusion . . . 36

5 Experimental and Theoretical Methods **37**
5.1 Low temperature STM . . . 37
5.1.1 Topography . . . 38
5.1.2 Spectroscopy . . . 40
5.1.3 Spectroscopic imaging . . . 41
5.2 Sample growth, characterisation and surface preparation . . . 41
5.3 DFT modelling . . . 42

6 Intrinsic Defects and CDW in pristine 1T-TiSe$_2$ **45**
6.1 Defects characterisation . . . 46
6.1.1 Defects signature in topography . . . 46
6.1.2 Spectroscopic signature of defects . . . 51
6.2 CDW in presence of single atom defects . . . 52
6.2.1 Topography of single atomic defects in presence of CDW . . . 52
6.2.2 A new insight into the CDW phase . . . 55
6.3 Conclusion . . . 58

7 CDW phase in 1T-Cu$_x$TiSe$_2$ **59**
7.1 Copper signature . . . 60
7.2 CDW instabilities . . . 62
7.3 The role of disorder: CDW domains . . . 63
7.4 Scanning tunneling spectroscopy on 1T-Cu$_x$TiSe$_2$ . . . 66
7.5 Consequences for the phase diagram of 1T-Cu$_x$TiSe$_2$ . . . 68
7.6 Conclusion . . . 70

8 Superconductivity in 1T-Cu$_x$TiSe$_2$ **73**
8.1 Superconducting transition . . . 73
8.2 Measuring the superconducting gap . . . 74
8.2.1 The superconducting gap and the role of disorder 74
8.2.2 CDW and superconductivity . . . 75
8.3 Conclusion . . . 78

9 Conclusions and Outlooks **81**

A Some properties of superconductors **85**

Acknowledgements **89**

Bibliography **93**

List of Figures

2.1 Peierls model 6
2.2 Superconducting transition temperatures versus year of discovery 14
2.3 General phase diagram and angular dependence of the superconducting gap in cuprates 15

3.1 Periodic table 19
3.2 1T and 2H polytypes 19
3.3 CDW lattice distortion in 1T-$TiSe_2$ 22
3.4 Model of the band structure of $TiSe_2$ in the normal and CDW states 22
3.5 1T-$Cu_x TiSe_2$: phase diagram and Cu content dependent lattice parameters 23

4.1 Representation of tunneling 31

5.1 The STM laboratory 39
5.2 STM imaging: constant-current mode 40
5.3 1$T$$Cu_x Tise_2$ single crystal and terraces 43

6.1 1T-$TiSe_2$: resistivity measurements and model of the crystal structure 47
6.2 1T-$TiSe_2$: topography 48
6.3 1T-$TiSe_2$: defects characterisation through topography and DFT 49
6.4 1T-$TiSe_2$: defects signature in STS 51
6.5 1T-$TiSe_2$: topography and CDW superlattice 53
6.6 1T-$TiSe_2$: topography in presence of CDW and model representation of the inequivalent lattice sites 53
6.7 1T-$TiSe_2$: defect characterisation in presence of CDW (Se vacancy, I and O substitutions) 55

6.8 $1T$-$TiSe_2$: STM and DFT characterisation of intercalated Ti 56
6.9 Chiral Friedel oscillations in $1T$-$TiSe_2$ 56

7.1 $1T$-$TiSe_2$: STM topography at room and low temperature, FFT 60
7.2 $1T$-$Cu_{0.07}TiSe_2$: Surface characterisation at 1.2 K 61
7.3 $1T$-$Cu_{0.07}TiSe_2$: Surface characterisation at 1.2 K 62
7.4 Stripe-region at the surface of $1T$-Cu_xTiSe_2 at 78 K . . . 63
7.5 $1T$-$Cu_{0.066}TiSe_2$: Surface characterization at 78K 64
7.6 CDW domains at the surface of $1T$-Cu_xTiSe_2 65
7.7 $1T$-$Cu_{0.07}TiSe_2$: STS in the range $\pm 1.3V$ 66
7.8 $1T$-$Cu_{0.066}TiSe_2$: STM micrographs and dI/dV maps . . 67
7.9 $1T$-$Cu_{0.07}TiSe_2$: STS between -420 mV and 150mV . . . 68
7.10 Phase-diagram of $1T$-Cu_xTiSe_2 70

8.1 $1T$-$Cu_{0.066}TiSe_2$: Magnetic susceptibility 74
8.2 $1T$-$Cu_{0.066}TiSe_2$: Characterisation of the superconducting gap and the role of disorder 76
8.3 $1T$-$Cu_{0.066}TiSe_2$: Map of the Γ parameter 77
8.4 $1T$-$Cu_{0.066}TiSe_2$: Average superconducting spectrum . . 77
8.5 $1T$-$Cu_{0.07}TiSe_2$: CDW and superconductivity 78

List of Tables

3.1 Properties of transition metal dichalcogenides 20
3.2 Cu_xTiSe_2 superconducting parameters 27

Abbreviations

1D	One-Dimension(al)
2D	Two-Dimension(al)
ARPES	Angle Resolved Photoemission Spectroscopy
BCS	Bardeen-Cooper-Schrieffer
CDW	Charge Density Wave
DFT	Density Functional Theory
EDX	Energy Dispersive X-ray analysis
FFT	Fast Fourier Transform
JT	Joule-Thomson
LDOS	Local Density of States
LT	Low-Temperature
SQUID	Superconducting Quantum Interference Devices
STM	Scanning Tunneling Microscopy
STS	Scanning Tunneling Spectroscopy
T_C	Superconducting Transition Temperature
TMD	Transition Metal Dichalcogenide
UHV	Ultra High Vacuum
vdW	van der Waals
XRD	X-Ray Diffraction

Chapter 1

Introduction

Quasi two-dimensional (2D) systems host fascinating physics and complex phase diagrams including charge or spin density waves, superconductivity and Mott insulating phase to name a few [1]. The relation between these different ground states is still far from being understood. One example is the interplay between charge ordered phases and superconductivity, which is still a subject of debates [2–5]. Indeed, not only the mechanism leading to the charge density wave (CDW) is not fully understood in many compounds [6, 7], but it is also not always clear whether superconductivity and CDW are interacting, excluding each other or simply coexisting. This question about the relation between charge order and superconductivity has received a renewed interest due to the recent discovery of a CDW inside the pseudogap phase of several cuprates [8–14]. Since these two ground states are found closer to each other also in other materials, like $2H$-$NbSe_2$ [15], $2H$-Cu_xTaS_2 [16] or CaC_6 [17], it is crucial to understand their roles for a better comprehension of superconductivity itself.

In studying quasi-2D materials, we have always to take into consideration that their properties are usually highly sensitive to disorder. For instance, it has been shown that in a high temperature superconductor belonging to the Bi-family, variations in the pseudogap states can be attributed to disorder in the oxygen dopant concentrations [18]. Another source of disorder is represented by atomic defects. An example in this case is given by $2H$-$NbSe_2$ where intrinsic defects induce a local CDW modulation above the standard CDW transition temperature [19], thus revealing the importance of strong-coupling between the electron and the lattice in the CDW formation. Impurities and atomic defects are

actually extremely important since they can be employed as probes to have an insight into the electronic ordered phases looking at the local modification they introduce [20]. In cuprate superconductors, the oscillations of the local density of states around impurities have been studied in detail by scanning tunneling spectroscopy (STS) as they allow to gain access to information about the Fermi surface and the momentum dependence of the superconducting gap [3, 21–24]. Recently, extrinsic impurities (sulfur atoms) have been used as a spectroscopic tool to increase this quasi-particle interference signal in $2H$-$NbSe_2$ to investigate its Fermi surface. This study confirmed the fundamental role played by electron-phonon coupling in the CDW formation instead of Fermi surface nesting [25]. Finally, defects and impurities are not only useful tools to study the physical properties of these materials, but they can be also used to intentionally modify these properties at the local scale, which is an essential step for the development of new devices [26, 27].

Clean surfaces of quasi-2D materials can be easily prepared, since these compounds can be exfoliated even with simple adhesive tape due to the weak van der Waals forces that are keeping the layers together. This is a relevant advantage that makes these materials especially suitable for surface-probe techniques, like scanning tunneling microscopy (STM). In addition, this characteristic allows the fabrication of single layers [28]. Since the discovery of graphene [29], new perspective for basic research and future applications have been developed studying physical properties of materials as function of thickness [26, 30]. The final aim is to combine these materials, building heterostructures with new interesting features compared to the starting elements [31]. Hence, a complete knowledge of the properties of bulk and exfoliated crystals is becoming the base for the development of new technologies.

STM/STS is an ideal technique to study quasi-2D materials, as it gives the opportunity to explore charge order, superconductivity and disorder at the atomic scale. Comparing STM results with density functional theory (DFT), it is possible to reach chemical sensitivity [32]. Furthermore, as reported above, scattering induced by defects/impurities creates interference patterns in the quasi particle density of states, which can be used to have momentum space information [21–23, 25].

In this work we focus our attention on bulk crystals of the layered transition metal dichalcogenide $1T$-$TiSe_2$ and the intercalated compound $1T$-Cu_xTiSe_2. Pristine $1T$-$TiSe_2$ is known for undergoing a transition to a CDW perfectly commensurate with the lattice and characterised by a peak in resistivity, the intensity of which strongly depends on the quality of the crystals [33]. The origin of this CDW transition is still far from being understood, even if several models have been pro-

posed [34–37]. Moreover, starting from the pristine crystal, both CDW and superconducting transitions can be tuned varying the concentration of Cu atoms [38]. The resulting phase diagram is similar to the one of cuprates, with a superconducting dome emerging in proximity to a CDW order [38]. This characteristic, together with a surface which can be prepared easily for STM/STS measurements, makes it a good model system to investigate CDW and superconductivity.

Our combined STM/STS/DFT study [39,40] allows us to classify the intrinsic defects in pristine $1T$-$TiSe_2$ and to determine their signature both in topography and in spectroscopy. Through this accurate identification, we establish without any doubt that the surface seen in STM micrographs correspond to the Se layer at all energies, and we offer an alternative explanation to a possible chiral behaviour of Friedel oscillations reported in literature [41]. In addition, we demonstrate that defects can be used also to determine the crystal polytype, showing that the absence of $2H$ inclusions on the surface of $1T$-$TiSe_2$. A similar approach has been applied on Cu intercalated samples where we discover the specific signature of Cu atoms and their exact position in the crystal structure. Thanks to this result it is now possible to know exactly the local concentration of Cu.

We show that intrinsic defects do not have a strong effect on the CDW superlattice, while Cu atoms destabilise the CDW already at low concentrations (1%) inducing the appearance of one dimensional patterns (stripes) which replace the commensurate $2a_0 \times 2b_0$ superstructure. Furthermore the disordered distribution of Cu atoms induce the formation of CDW domains, which can survive even at Cu concentration higher than 4%, for which no signature of a CDW transition can be detected in transport measurements. Finally we report some preliminary measurements on the superconducting phase of $1T$-Cu_xTiSe_2, showing that all superconducting spectra belonging to different regions and samples can be fitted with a standard BCS fit for a single gap with an s-wave symmetry. We study the role of disorder and of CDW domains in this superconducting phase. We show hints that disorder, intended as intrinsic defects and/or non-uniform Cu distribution, could create domains with slightly different gap sizes, and that the presence of CDW domains does not lead to a local suppression of the superconducting gap.

This manuscript is divided in the following way. Fundamental concepts related to charge density waves and superconductivity are summarised in Chap. 2. In Chap. 3 we review the literature on the two crystals studied in this work, namely $1T$-$TiSe_2$ and $1T$-Cu_xTiSe_2. The basic principles of the tunneling process and the scanning tunneling

microscopy are introduced in Chap.4. The experimental technique, the crystal growth and theoretical methods applied to simulate our STM micrographs are presented in Chap.5. A detailed defect characterisation in pristine $1T$-$TiSe_2$ in the absence and presence of charge density waves (CDW) is reported in Chap. 6. In Chap. 7 we present a study of the CDW phase in $1T$-Cu_xTiSe_2. Finally, in Chap. 8 we report a preliminary study of the superconducting gap in $1T$-Cu_xTiSe_2 ($x \sim 0.07$) single crystals.

Chapter 2

Theoretical Background

The physics of quasi-two dimensional systems is particularly rich of intriguing phenomena. These materials often present a complex phase diagram where the relationship between different ground states – such as charge or spin density waves, superconductivity or Mott insulator-phase – is still far from being understood [1]. This chapter gives a brief theoretical introduction into charge density waves (CDW) and superconductivity. Further details can be found in the reviews of Grüner [42,43], Rossnagel [6] and Berthod's lecture notes [44] for the CDW and in Tinkham's book [45] for superconductivity.

2.1 Charge Density Wave Formation

A CDW is a periodic modulation of the electron density, which often develops in low dimensional materials and it is usually due to electron-phonon interactions. In this new ground state the electron density $\rho(\boldsymbol{r})$ is periodically modulated and accompanied by a periodic lattice distortion u_n:

$$\rho(\boldsymbol{r}) = \rho_0(\boldsymbol{r})[1 + \underbrace{\rho_m \cos(\boldsymbol{q}_0 \boldsymbol{r} + \phi)}_{\text{CDW}}], \tag{2.1a}$$

$$u_n = u_0 \sin(n|\boldsymbol{q}_0|a + \phi), \tag{2.1b}$$

where $\rho_0(\boldsymbol{r})$ is the electron density without perturbation, ρ_m, $\boldsymbol{q}_0$ and ϕ are the amplitude, wavevector and phase of the electron density modulation respectively; n is an integer that defines the position of the ions

and u_0 is the amplitude of the lattice modulation, which is small compared with the lattice constant a. As a consequence of the development of a CDW, strong modifications of the electron and phonon spectra are expected.

This phenomenon is usually represented using a 1D model consisting in a linear chain of atoms with a regular lattice spacing a (Fig. 2.1) [6, 42, 43, 46, 47]. We assume a half-filled band, meaning that if the Brillouin zone extends to $\pm\pi/a$ then the band is filled up to $\pm k_F = \pm\pi/2a$. These two "Fermi points" at $\pm k_F = \pm\pi/2a$ are therefore connected by the *nesting vector* $q_{CDW} = 2k_F$. Peierls [46] has been the first one to suggest that this system is unstable in the presence of an electron-phonon interaction. Introducing a periodic lattice distortion consisting in a doubling of the lattice constant, the size of the Brillouin zone is divided by 2 and it now extends to $\pm k_F$. The consequence of this distortion is the creation of a additional potential and therefore a gap Δ opens at $\pm k_F$, which are the zone boundaries of the new 2-atom unit cell. Within this model, the presence of this gap will lower the electronic energy, and the system will become insulating. At the same time a periodic modulation of the electron density with the same wavelength q_{CDW} will develop. The main hypothesis underlying this model is that this gain in electronic energy is higher than the elastic energy spent for the lattice deformation. In the general case of an arbitrary band filling, the CDW wavelength ($2\pi/q_{CDW}$) will be incommensurate with the underlying lattice.

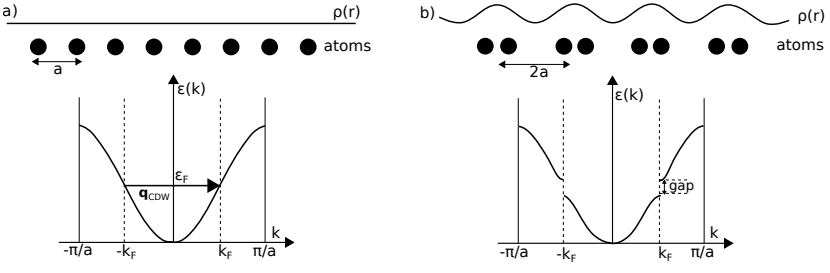

Figure 2.1: Peierls distortion in a 1D metallic chain. a) Undistorted lattice b) Distorted lattice and opening of the gap. *Adapted from Grüner et al. [43].*

A coupled electron-lattice system can be described by the following Hamiltonian based on the independent electrons, harmonic and adia-

batic approximations:

$$\mathscr{H}_P = \sum_{\boldsymbol{k\sigma}} \epsilon_{\boldsymbol{k}} a^\dagger_{\boldsymbol{k\sigma}} a_{\boldsymbol{k\sigma}} + \sum_{\boldsymbol{q\lambda}} \hbar\omega_{\boldsymbol{q}\lambda} b^\dagger_{\boldsymbol{q}\lambda} b_{\boldsymbol{q}\lambda} + \sum_{\boldsymbol{k}\sigma} \sum_{\boldsymbol{q}\lambda} g_{\boldsymbol{q}\lambda} a^\dagger_{\boldsymbol{k}+\boldsymbol{q}\sigma} a_{\boldsymbol{k}\sigma} (b^\dagger_{-\boldsymbol{q}\lambda} + b_{\boldsymbol{q}\lambda}), \tag{2.2}$$

where:

- the first term is the kinetic energy of the electrons, expressed in terms of the single-electron energies $\epsilon_{\boldsymbol{k}}$, and $a^\dagger_{\boldsymbol{k}\sigma}$ and $a_{\boldsymbol{k}\sigma}$ are the creation and annihilation operators for state $\boldsymbol{k}$ with spin σ;
- the second term is the energy of the free phonons with $\omega_{\boldsymbol{q}\lambda}$ the frequency of the normal mode $\boldsymbol{q}$ with polarization λ, and $b^\dagger_{\boldsymbol{q}\lambda}$ and $b_{\boldsymbol{q}\lambda}$ are the creation and annihilation operators for phonon $\boldsymbol{q}$ with polarization λ;
- the third term describes the electron-phonon interaction with $g_{\boldsymbol{q}\lambda}$ the electron-phonon coupling constant considered independent of $\boldsymbol{k}$.

In the following, starting from this Hamiltonian, a many body theory approach will be used to derive the conditions driving the lattice and the electron instabilities and to calculate the CDW gap in the electronic band dispersion [44].

2.1.1 The lattice instability

Using the Hamiltonian in Eq. 2.2 it is possible to calculate the phonon propagator with perturbation theory. This phonon propagator is given by:

$$\mathscr{P}_\lambda(\boldsymbol{q}, \tau) = -\langle T_\tau b_{\boldsymbol{q}\lambda}(\tau) b^\dagger_{\boldsymbol{q}\lambda}(0) \rangle \tag{2.3}$$

where λ is the polarization of the phonon, τ is the imaginary-time variable and T_τ is the time-ordering operator defined as:

$$T_\tau A(\tau) B(0) = \theta(\tau) A(\tau) B(0) + \eta\theta(-\tau) B(0) A(\tau) \tag{2.4}$$

with A and B two operators, θ is the Heavyside theta function, and $\eta = +1$ for bosons and $\eta = -1$ for fermions. In the presence of interaction the phonon propagator becomes:

$$\mathscr{P}_\lambda(\boldsymbol{q}, i\Omega_n) = \frac{1}{i\Omega_n - \hbar\omega_{\boldsymbol{q}\lambda} - \Sigma^{ph}_\lambda(\boldsymbol{q}, i\Omega_n)} \tag{2.5}$$

where $i\Omega_n$ is the bosonic Matsubara frequency and $\Sigma^{ph}_\lambda(\boldsymbol{q}, i\Omega_n)$ is the *self-energy*, which describes the renormalisation and the damping of the

phonons. This self energy can be calculated [44] and at leading order is given by:

$$\Sigma_{\lambda}^{ph}(\boldsymbol{q}, i\Omega_n) = |g_{\boldsymbol{q}\lambda}|^2 \chi_0(\boldsymbol{q}, i\Omega_n), \tag{2.6}$$

where $\chi_0(\boldsymbol{q}, i\Omega_n)$ is the *non-interacting charge susceptibility*.

The renormalised phonon frequency $\omega^*_{\boldsymbol{q}\lambda}$ (*Kohn anomaly*) is defined as:

$$\omega^*_{\boldsymbol{q}\lambda} \equiv \omega_{\boldsymbol{q}\lambda} + |g_{\boldsymbol{q}\lambda}|^2 \chi_0(\boldsymbol{q}, 0). \tag{2.7}$$

When $\omega^*_{\boldsymbol{q}\lambda} = 0$ (*phonon softening*) we have a pole in the phonon Green's function (2.5) at zero energy ($i\Omega_n = 0$), which is the signature of a lattice instability.

2.1.2 The electronic instability

The condition for an electronic instability driven by nesting is a divergence of the *charge susceptibility* $\chi(\boldsymbol{q}, \omega)$ at zero energy. To be able to calculate $\chi(\boldsymbol{q}, \omega)$ with the Hamiltonian (2.2), we need to consider an effective phonon-mediated interaction between electrons:

$$V_{el-el}^{ph}(\boldsymbol{q}, i\Omega_n) = \sum_{\lambda} |g_{\boldsymbol{q}\lambda}|^2 \mathscr{D}_{\lambda}^0(\boldsymbol{q}, i\Omega_n), \tag{2.8}$$

where $\mathscr{D}_{\lambda}^0(\boldsymbol{q}, i\Omega_n)$ is the propagator for a combination of two phonons at wave vectors q and $-q$. The charge susceptibility is defined as the density-density correlation function:

$$\chi(\boldsymbol{q}, \tau) = -\langle T_\tau n(\boldsymbol{q}, \tau) n(-\boldsymbol{q}, 0) \rangle, \tag{2.9}$$

where $n(\boldsymbol{q})$ is the density operator given by $n(\boldsymbol{q}) = \sum_{\boldsymbol{k}\sigma} a^\dagger_{\boldsymbol{k}\sigma} a_{\boldsymbol{k}+\boldsymbol{q}\sigma}$.

Usually $\chi(\boldsymbol{q}, i\Omega_n)$ cannot be calculated exactly but there are approximations like the *random-phase approximation* (RPA) [44]. Within this approximation and considering a non-adiabatic limit with a static interaction $V_{el-el}^{ph}(\boldsymbol{q}, 0)$, the susceptibility is given by:

$$\chi_{RPA}(\boldsymbol{q}, i\Omega_n) = \frac{\chi_0(\boldsymbol{q}, i\Omega_n)}{1 - V_{el-el}^{ph}(\boldsymbol{q}, 0)\chi_0(\boldsymbol{q}, i\Omega_n)}. \tag{2.10}$$

A divergence of the susceptibility at zero energy ($i\Omega_n = 0$) is the signature of a charge instability, which leads the the CDW formation. χ_{RPA} is divergent when the following condition is satisfied:

$$0 = 1 - V_{el-el}^{ph}(\boldsymbol{q}, 0)\chi_0(\boldsymbol{q}, 0) = 1 + 2\left(\sum_{\lambda} \frac{|g_{\boldsymbol{q}\lambda}|^2}{\omega_{\boldsymbol{q}\lambda}}\right) \chi_0(\boldsymbol{q}, 0) \tag{2.11}$$

We notice that Eq. 2.11 and Eq. 2.7 for the lattice instability are identical except for a factor 2 if we consider only one phonon branch, such that the two conditions would yield different transition temperatures. The factor 2 difference may be due to the fact that we used two distinct approximations. The condition (2.7) based on phonon softening is valid in the adiabatic limit where the phonons are slow compared to the electrons, and the lattice dynamics is controlled by the phonons. The condition (2.11) assumes an instantaneous phonon-mediated interaction between the electrons, and is therefore valid in the opposite anti-adiabatic limit where the phonons are fast compared to the electrons. This means that at this level of approximation we cannot determine which of the two instabilities appears first when lowering the temperature, but only that these instabilities can happen if their respective conditions are satisfied (Eq. 2.7 and Eq. 2.11).

2.1.3 The gap in the electronic spectrum

We now consider the ordered phase. To describe its electronic properties the starting point is the electronic Hamiltonian:

$$H = \sum_{\boldsymbol{k}\sigma} \epsilon_{\boldsymbol{k}} a^{\dagger}_{\boldsymbol{k}\sigma} a_{\boldsymbol{k}\sigma} + \frac{1}{2} \sum_{\boldsymbol{k}_1\sigma_1\boldsymbol{k}_2\sigma_2\boldsymbol{q}} V^{ph}_{el-el}(\boldsymbol{q}, 0) a^{\dagger}_{\boldsymbol{k}_1+\boldsymbol{q}\sigma_1} a^{\dagger}_{\boldsymbol{k}_2-\boldsymbol{q}\sigma_2} a_{\boldsymbol{k}_2\sigma_2} a_{\boldsymbol{k}_1\sigma_1}. \tag{2.12}$$

We perform a mean-field approximation with respect to the phonon mediated interaction, and we assume that a CDW potential develops with a single wave vector $\boldsymbol{Q}$. It is then possible to calculate the electron Green's function. This Green's function at the leading order is:

$$\mathscr{G}^{(1)}_{\boldsymbol{k}\boldsymbol{k}}(i\omega_n) = \frac{1}{i\omega_n - \xi_{\boldsymbol{k}} - \frac{V^2(\boldsymbol{Q})}{i\omega_n - \xi_{\boldsymbol{k}-\boldsymbol{Q}}} - \frac{V^2(\boldsymbol{Q})}{i\omega_n - \xi_{\boldsymbol{k}+\boldsymbol{Q}}}}, \tag{2.13}$$

where $i\omega_n$ is the fermionic Matsubara frequency, $\xi_k = \epsilon_k - \mu$ is the dispersion measured from the chemical potential μ and $V(\boldsymbol{Q})$ is the periodic potential correspnding to the Hartree and exchange fields of the phonon-mediated interaction.

The excitations energies ω are given by the condition:

$$\omega - \xi_{\boldsymbol{k}} - \frac{V^2(\boldsymbol{Q})}{\omega - \xi_{\boldsymbol{k}-\boldsymbol{Q}}} - \frac{V^2(\boldsymbol{Q})}{\omega - \xi_{\boldsymbol{k}+\boldsymbol{Q}}} = 0. \tag{2.14}$$

and the gap opens at points $\boldsymbol{k}$ that are connected by the CDW vector $\boldsymbol{Q}$ (*nesting vector*) to other points with the same energy, such that $\xi_{\boldsymbol{k}} = \xi_{\boldsymbol{k}-\boldsymbol{Q}} = \xi_{\boldsymbol{k}+\boldsymbol{Q}}$ and Eq. 2.14 reduces to $(\omega - \xi_{\boldsymbol{k}})^2 - 2V^2(\boldsymbol{Q}) = 0$. In this

way we obtain a CDW gap given by:

$$2\Delta = 2\sqrt{2}V(\boldsymbol{Q}) \tag{2.15}$$

where $V(\boldsymbol{Q}) = V^{ph}_{el-el}(\boldsymbol{Q})n(\boldsymbol{Q})$. To determine the order parameter Δ below the transition, one uses the fact that the potential $V(Q)$ is proportional to the Fourier component of the electron density $n(Q)$. The latter can be expressed in terms of the Green's function, leading to a self-consistency equation for Δ. The resulting gap equation reduces to a "BCS-type" equation for a one-dimensional tight-binding dispersion $\xi_k = 2t\cos(ka)$ with $Q = k_F = \pi/a$. In the next section we will look more in details into this 1D case.

2.1.4 From 1D to 2D systems

Consider the specific case of a 1D solid with a single half-filled [6, 43, 48] band and assume a tight-binding band dispersion of the form:

$$\epsilon_{\boldsymbol{k}} = -E_F\cos(ka) \tag{2.16}$$

where $-\pi/a \leq k \leq \pi/a$ and E_F is the Fermi energy. For a 1D system, the non-interacting electronic susceptibility χ_0 has a logarithmic divergence at $2Q = 2k_F$. At finite temperature this singularity is smoothed and in the limit of small temperature ($k_BT \ll \epsilon_F$), the non interacting susceptibility at $2Q$ becomes:

$$\chi_0(2k_F, T) = \frac{1}{2}N(0)\ln\left(\frac{2.28E_F}{k_BT}\right) \tag{2.17}$$

where $N(0)$ is the density of electron states at the Fermi energy E_F.

From Eq. 2.7 and using Eq. 2.17, we see that a softening of the $2Q$ phonon mode ($\omega^*_{2Q} = 0$) happens at a finite temperature T_{CDW} given by:

$$k_BT_{CDW} = 2.28E_F\exp\left(-\frac{1}{\lambda}\right) \tag{2.18}$$

where $\lambda \propto |g_{2Q}|^2N(0)/\omega_{2Q}$ is the *electron-phonon coupling constant*.

The electronic instability [6, 43], in the weak coupling limit ($\Delta \ll \epsilon_F$) $\Delta(T)$ follows a "BCS type" temperature dependence. Rice and Strässler [48] showed that this gap Δ vanishes at the temperature of the lattice instability (Eq.2.18). In this formulation Δ at $T = 0$ is given by:

$$\Delta(0) = 4E_F\exp\left(-\frac{1}{\lambda}\right), \tag{2.19}$$

and using Eq. 2.18 and Eq. 2.19 we can obtain a “BCS-type" ratio:

$$2\Delta(T=0) = 3.52 k_B T_{CDW} \tag{2.20}$$

In case of strong coupling, deviations from this behaviour are expected and Eq. 2.20 will be substituted by $2\Delta(T=0) > 3.52 k_B T_{CDW}$.

Transferring this model to higher dimensions is not an easy task [7, 49]. Indeed, considering for instance quasi 2D materials, there are already many differences compared to this specific 1D case:

- Fermi surface nesting: this is not satisfied everywhere on the Fermi surface [47, 49], the gap is only partial and the material is not becoming insulating; on the contrary it can become even a better metal [7];
- Non-interacting electronic susceptibility χ_0: it is usually not divergent, the Kohn anomaly is smoothed and not easily observable [6, 7, 42, 49];
- Electron-phonon coupling: it is usually strong and can play an important role in the CDW transition [7, 49–52];
- CDW gap: it differs from a “BCS type" gap as soon as we are not considering a 1D system with a tight binding dispersion (see section 2.1.3 and [44]);

Therefore deviations from the ideal 1D case are expected and, in spite of the fact that CDW in low-dimensional materials is an old topic [46, 53, 54], the reasons of their formation, especially in quasi-two dimensional systems, is still a subject of debates. In the last twenty years [7, 47, 49] it has been repeatedly suggested that nesting is probably not the best model to describe CDW in transition metal dichalcogenides, one of the main families of quasi 2D-materials. Recently, Johannes *et al.* proposed that a new theory should be developed, based on the fact that the $\boldsymbol{q}$-dependent electron-phonon coupling ($g_{\boldsymbol{q}\lambda}$) plays a fundamental role. This hypothesis is supported by x-ray scattering and scanning tunneling microscope measurements on transition metal dichalcogenides [52, 55], but no final conclusion has been reached yet. Other models also exist, like a band Jahn-Teller effect [35, 36] or an excitonic insulator mechanism [34] and they will be briefly introduced in chapter 3 since they are particularly relevant for the material studied in this work. However a coherent microscopic general theory is missing and the field is still open.

2.2 Superconductivity basics

In the rest of this chapter some basic concepts regarding superconductivity are presented. A short overview of the main properties shown by superconductors from an historical perspective is reported in the appendix at the end of this work. Here will focus on the BCS theory and the expression for the superconducting gap, which is the quantity that we will measure in scanning tunneling spectroscopy (see chapter 4 and 8). Finally we will briefly introduce non-conventional superconductors and in particular the special case represented by hole-doped cuprates. These quasi-two dimensional materials not only cannot be described by a standard BCS-theory, but they are also characterised by an interesting phase diagram with spin and charge ordering close to the superconducting dome.

2.2.1 The BCS theory and the superconducting gap

In 1957 Bardeen, Cooper and Schrieffer published their famous theory of superconductivity "based on the fact that the interaction between electrons resulting from virtual exchange of phonons is attractive when the energy difference between the electrons states involved is less than the phonon energy, $\hbar\omega$" [56]. They constructed a wavefunction of a combination of these pairs of electrons (*Cooper pairs*) and they discovered a stable ground state with a gap in the density of states. This ground states wave function is:

$$|\Psi_{BCS}\rangle = \prod_{\boldsymbol{k}} (u_{\boldsymbol{k}} + v_{\boldsymbol{k}} c^{\dagger}_{\boldsymbol{k}\uparrow} c^{\dagger}_{-\boldsymbol{k}\downarrow})|0\rangle, \tag{2.21}$$

with

$$|u_{\boldsymbol{k}}|^2 + |v_{\boldsymbol{k}}|^2 = 1 \tag{2.22}$$

where $c^{\dagger}_{\boldsymbol{k}\uparrow}/c^{\dagger}_{-\boldsymbol{k}\downarrow}$ are the creation operators for an electron of momentum $\boldsymbol{k}$/- $\boldsymbol{k}$ and spin $\uparrow/\downarrow$ and $|0\rangle$ is the vacuum state. Eqs. 2.21 and 2.22 imply that the probability of the pair state ($\boldsymbol{k}\uparrow, -\boldsymbol{k}\downarrow$) to be occupied is $|v_{\boldsymbol{k}}|^2$, while the probability that it is unoccupied is given by $|u_{\boldsymbol{k}}|^2 = 1 - |v_{\boldsymbol{k}}|^2$. After a variational calculation, they obtained:

$$|v_{\boldsymbol{k}}|^2 = 1 - |u_{\boldsymbol{k}}|^2 = \frac{1}{2}\left(1 - \frac{\xi_{\boldsymbol{k}}}{E_{\boldsymbol{k}}}\right) \tag{2.23}$$

where $\xi_{\boldsymbol{k}}$ is the single particle energy relative to the Fermi energy, $\Delta_{\boldsymbol{k}}$ is the size of the gap (minimum energy required to break a pair), and

$E_{\boldsymbol{k}}$ is the excitation energy of a quasi-particle of momentum $\hbar\boldsymbol{k}$ defined by:

$$E_{\boldsymbol{k}} = \sqrt{\xi_{\boldsymbol{k}}^2 + |\Delta_{\boldsymbol{k}}|^2}. \tag{2.24}$$

In the original BCS theory, Δ is independent of $\boldsymbol{k}$, but this is not valid for all materials, like for example cuprates (see next section). If we now consider the temperature dependence of the gap, $\Delta(T)$, we clearly see from Eq. 2.24 that for $T = T_C$, where $\Delta(T) \to 0$, $E_{\boldsymbol{k}} \to |\xi_{\boldsymbol{k}}|$. Therefore for $T \geq T_C$ the excitation spectrum coincides with the one of the normal state. It can be shown [45] that in the weak coupling limit ($\hbar\omega_D/k_B T_c \gg 1$ with ω_D the Debye frequency), $\Delta(T)/\Delta(0)$ is a universal function of T/T_C. This function decreases monotonically from 1 at $T = 0$ to zero at $T = T_C$. For a temperature close to T_C, $\Delta(T)$ drops to zero approximately as:

$$\frac{\Delta(T)}{\Delta(0)} \approx 1.74\sqrt{\left(1 - \frac{T}{T_C}\right)}, \tag{2.25}$$

while close to $T = 0$, the temperature variation is exponentially slow and $\Delta(T)$ approaches its limiting value $\Delta(0)$ given by the famous relation:

$$2\Delta(0) = 3.528 k_B T_C. \tag{2.26}$$

Finally, we are interested in computing the superconducting DOS (D_s), since this is the quantity measured by scanning tunneling spectroscopy, as we will see in chapter 4. At energies close to E_F, D_s can be directly related to the normal state DOS (D_n) using the fact that there is a one-to-one correspondence between the points in k-space in the superconducting and the normal states. Furthermore, close to E_F we can assume that $D_n(\xi_{\boldsymbol{k}})$ has a constant value $D_n(0)$ and write:

$$D_s(E_k)dE_k = D_n(\xi_k)d\xi_k \approx D_n(0)d\xi_k. \tag{2.27}$$

Hence, the density of quasi-particle states within the BCS framework at zero temperature is:

$$\frac{D_s(E_k)}{D_n(0)} = \frac{d\xi_{\boldsymbol{k}}}{dE_{\boldsymbol{k}}} = \begin{cases} \dfrac{E_k}{\sqrt{E_k^2 - \Delta^2}} & E_k > \Delta \quad \text{(2.28a)} \\ 0 & E_k < \Delta \quad \text{(2.28b)} \end{cases}$$

meaning that no states exist in the gap.

2.2.2 Beyond BCS superconductors

Over the years the number of materials showing superconductivity notably increased: heavy fermion superconductors [57], organic superconductors [58], cuprates [59], ruthenates [60], MgB_2 [61], iron based superconductors [62], and very recently hydrogen rich compounds under very high pressure [63] (see Fig. 2.2). In the majority of them superconductivity is “unconventional" in the sense that it cannot be described by the standard BCS theory. The most studied family of unconventional superconductors is the one of cuprates, which is also the class of materials with one of the highest T_C (165K for a Hg-based copper oxide under pressure [64]). Cuprates have a layered structure made of CuO_2 planes separated by charge reservoir layers, which control the carrier concentration in the CuO_2 planes [65]. A typical phase

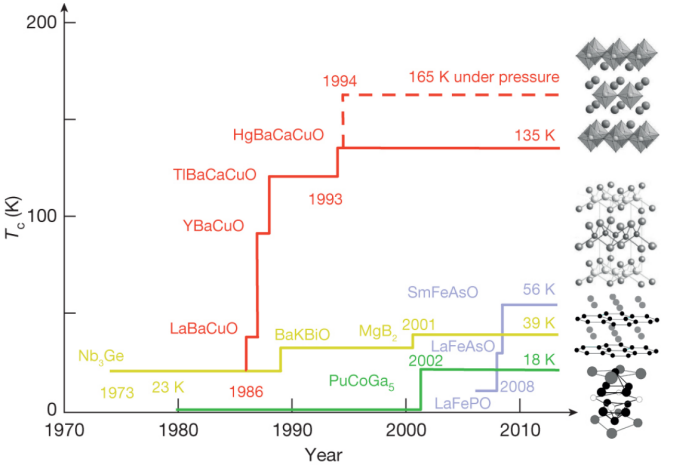

Figure 2.2: Superconducting transition temperatures versus year of discovery. On the right crystal structures of representative materials from each family of superconductors. [5].

diagram is reported in Fig 2.3a for an hole doped cuprate [5]. Increasing the hole-doping, the antiferromagnetic Mott insulating phase disappears and a superconducting dome emerges, characterised by a strong momentum dependent gap with a *d-wave* symmetry [66] (Fig. 2.3b) instead of a standard *s-wave* BCS gap. Between T_C and T^* there is the so called *pseudogap phase*, where a substantial suppression of the electron density of states is observed at low energy [3–5, 67]. Like the superconducting gap, the pseudogap in underdoped cuprates has a strong momentum dependence (Fig. 2.3b) while T^* has the opposite

behaviour compared to T_C, decreasing with increasing hole concentration [3, 4, 67]. Whether the endpoint of the T^* line is inside or outside the superconducting dome is still not clear [3, 4, 68, 69]. Above T^* and for a large range of hole-doping, a non-Fermi liquid behaviour is observed (*strange-metal phase*), and only for even higher hole-doping the standard Fermi liquid behaviour is recovered. A similar phase diagram can be drawn also for electron-doped cuprates, but in this case the antiferromagnetic phase is more robust, T_C is lower and no pseudogap is observed.

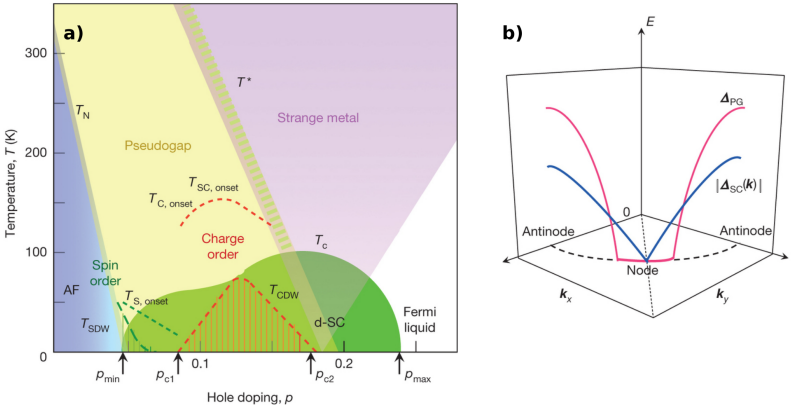

Figure 2.3: a) Phase diagram for the copper oxides (temperature versus hole doping). $T_{S,onset}$: onset temperature for spin fluctuations; $T_{C,onset}$ onset temperature for charge fluctuations; $T_{SC,onset}$: onset temperature for superconducting fluctuations; T^* pseudogap transition temperature; T_N: Néel transition temperature for the antiferomagnetic (AF) order; T_C: transition temperature for a d-wave superconducting order (d-SC); T_{CDW}: transition temperature for fully developed charge order; T_{SDW}: transition temperature for incommensurate spin density wave order. Arrows the quantum critical points for superconductivity and charge order [5]. b) Angular dependence of the superconducting gap Δ_{SC} and pseudogap Δ_{PG} along the normal-state Fermi surface (dashed line). Around the superconducting node, the pseudogap has a gapless region, forming the so called *Fermi-arcs* [5].

Understanding the nature of the pseudogap phase in hole-doped cuprates is of particular interest, since superconductivity is emerging from this state. There are mainly two possible origins suggested for this unusual phase. In the first theory, the pseudogap has been associated with superconducting fluctuations [3–5, 45, 70–72]. According to this

model, supported by many experiments [73–76], Cooper pairs already form at T^* but their phase get locked only at T_C allowing the emergence of superconductivity. An alternative model suggests the presence of another ordered phase [3–5, 77]. Indeed, in the last twenty years, different kinds of charge orders have been observed inside this pseudogap region. Stripes, charge order coexisting with spin order, have been first detected in La-based cuprates by neutron scattering [78–81], and a peculiar checkerboard order has been observed by STM in Bi-based [22, 82–87] and Ca-based cuprates [24]. Few years ago, a CDW order has been discovered also in Y-based cuprates by nuclear magnetic resonance [8, 88] and high energy X-ray diffraction in magnetic field [9] and by resonant soft X-ray scattering in absence of magnetic field [10, 89]. Later, high resolution non-resonant inelastic X-ray scattering [90], and sound velocity measurements [91] have revealed that the charge order is static, probably due to the pinning of correlated charge fluctuations by defects [92]. It is still under debate whether this charge order is unidirectional (stripe) or bidirectional (checkerboard) [91, 93]. A similar charge order has been found in Bi-based copper oxides [4, 11, 12] and Hg-based cuprates [13], and even in an electron doped cuprate ($Nd_{2-x}Ce_xCuO_4$) [14]. If and how this charge order is related to the presence of the pseudogap, to superconducting fluctuations and/or to the emergence of superconductivity are all open questions [2–5], and scanning tunneling microscopy and spectroscopy are well suited to contribute in finding an answer [3].

2.3 Conclusions

In this chapter we have shown a basic model for CDW. We have seen the difficulties in transferring this model from 1D to 2D. In the second part we have introduced some basics concepts regarding superconductivity, and especially an expression for the density of states, which is the quantity measured in scanning tunneling spectroscopy. These two physical phenomena, CDW and superconductivity, manifest themselves in high-T_C superconductors, but their relationship is still far from being understood. A possible way to improve our understanding is to study simpler systems, where it could be easier to discern the respective roles.

Chapter 3

The family of Transition Metal Dichalcogenides and two case studies: $1T$-$TiSe_2$ and $1T$-Cu_xTiSe_2

Nowadays the attention towards the family of transition metal dichalcogenides (TMDs) is rising exponentially [26, 28, 30, 31, 94, 95]. Indeed, many TMDs have a layered structure and, like graphite [29], they can be easily exfoliated [28] opening a new field in technological innovation. These materials have been studied for decades [96–100], but still many of their properties are not fully understood. A detailed investigation of these compounds, from bulk to monolayer, is becoming necessary for their possible future applications. In the following chapter, after a short review on the family of TMDs, we will focus on the crystal structure and physical characterisation of the materials studied in this work: $1T$-$TiSe_2$ and $1T$-Cu_xTiSe_2.

3.1 TMD family

TMDs are compounds represented by the general formula MX_2, where M is a transition metal coming from groups 4-10 in the periodic table, and X is a chalcogen atom belonging to group 16 (S, Se, or Te) (Fig. 3.1). Due to the large amount of possible combinations of these elements, this class of materials exhibits a broad variety of properties:

they can be semiconductors or metals, or they can show more intriguing phenomena, like superconductivity and charge ordering transitions (Tab. 3.1). Many of them crystallise in a layered structure made of "sandwiches" of transition metal atoms between two chalcogen atom layers (S, Se, or Te); consecutive layers are then kept together thanks to van der Waals forces. Different polytypes, i.e. different stacking orders, are possible. The most common are $1T$ and $2H$ polytypes, where the digit stays for the number of layers in the unit cell and the letter represents the crystal system, trigonal (T) or hexagonal (H). In the first case the metal atom is in an octahedral site, while in the second it sits in a trigonal prismatic site (Fig. 3.2). If the crystal system is the same, a lower case letter is added to distinguish between stacking sequences corresponding to different layer alignments: $2Ha$, $2Hb$, $2Hc$ [101]. For example in the $2Ha$ polytype, like $NbSe_2$ (Fig. 3.2, right), metal atoms belonging to consecutive layers are exactly on top of each other (stacking sequence BaB/CaC), while in other $2H$-polytypes, like $2Hc$-MoS_2, this alignment is kept each two layers and the metal atom in between is shifted (stacking sequence BcB/CbC). The typical one-layer-thickness is about $\sim$6-7Å ([96]), and the absence of dangling bonds at the surface chalcogen layer makes TMDs crsytals quite stable in standard ambient conditions.

Together with composition and structure, dimensionality plays an important role in determining the material properties. In fact, due to weak van der Waals bonding between layers and strong covalent bonding between metal and chalcogen atoms, a single crystal can be exfoliated down to single layer quite easily. Studying physical properties as a function of thickness is opening new perspectives for basic research and future applications. The most known example is $2H$-MoS_2, where the semiconducting indirect band gap of bulk crystals becomes a direct gap in the monolayer [103]. This characteristic makes it suitable for building transistors, light emitting diodes, photo-detectors, solar cells or chemical sensors [26, 30]. Furthermore, it is possible to combine these materials building heterostructure exhibiting new interesting features compared to the starting elements [31].

3.2 1T-$TiSe_2$

$TiSe_2$ crystallises in the $1T$-phase (Fig.3.2, left) with unit cell parameters: a_0 = 3.54Å, c_0 = 6.00Å [96]. At room temperature the band structure of 1T-$TiSe_2$ (Fig. 3.4) consists of a Se 4p-valence band at the Γ point and a Ti 3d-conduction band at the L point of the Brillouin zone [104–106]. Many attempts have been made to determine the rela-

1																	18
H	2											13	14	15	**16**	17	He
Li	Be											B	C	N	O	F	Ne
Na	Mg	3	**4**	**5**	**6**	**7**	8	**9**	**10**	11	12	Al	Si	P	**S**	Cl	Ar
K	Ca	Sc	**Ti**	**V**	Cr	Mn	Fe	**Co**	**Ni**	Cu	Zn	Ga	Ge	As	**Se**	Br	Kr
Rb	Sr	Y	**Zr**	**Nb**	**Mo**	**Tc**	Ru	**Rh**	**Pd**	Ag	Cd	In	Sn	Sb	**Te**	I	Xe
Cs	Ba	La-Lu	**Hf**	**Ta**	**W**	**Re**	Os	**Ir**	**Pt**	Au	Hg	Tl	Pb	Bi	Po	At	Rn
Fr	Ra	Ac-Lr	Rf	Db	Sg	Bh	Hs	Mt	Ds	Rg	Cn	Uut	Fl	Uup	Lv	Uus	Uuo

Figure 3.1: Periodic table. Dark grey: chalcogens. Medium grey: transition metals that form layered crystals. Light grey: transition metals that can crystallise in a layered structure or in a different structure, according to the chalcogen atom they are bonded with (adapted form Chhowalla *et al.* [30]).

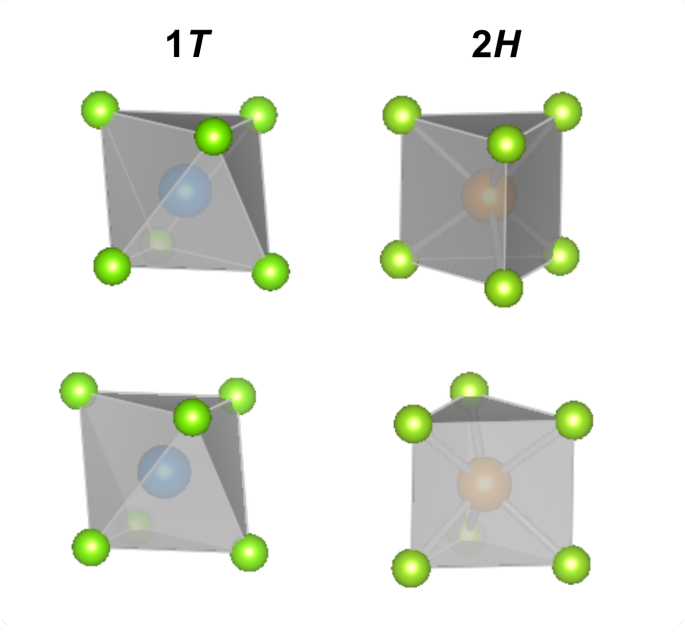

Figure 3.2: 1T and 2H polytypes [102].

Group	M	Properties
4	Ti, Zr, Hf	Semiconductors/semimetals. TiSe2: CDW
5	V, Nb, Ta	Metals/semimetals, superconductors, CDW
6	Mo, W	Sulfide/selenides: semiconducting Tellurides: semimetallic
7	Tc, Re	Small-gap semiconductors
10	Pd, Pt	Sulfides/selenides: semiconducting Tellurides: metallic. PdTe2: superconducting.

Table 3.1: Properties of transition metal dichalcogenides [30, 96].

tive energy positions of conduction and valence bands, but it is still not clear if this compound should be considered a semi-metal or a semiconductor [107]. From Hall coefficient measurements, the estimated number of carriers for stoichiometric samples is $\sim 10^{20}$ cm^{-3} [33], 10 order of magnitude greater than the one in silicon [108] and 2 order of magnitude lower than in standard metals like copper [109]. A detailed study by Di Salvo et $al.$ [33] shows that the sample stoichiometry is highly dependent on the temperature used for the growth. This temperature range can vary between 570°C to 1000°C and the amount of Ti in excess is increasing with this temperature, reaching the maximum value of $\sim$2%.

3.2.1 1T-TiSe$_2$: phase transitions

Below $\sim$200K, TiSe$_2$ undergoes a phase transition to a commensurate CDW with periodicity $2a_0 \times 2b_0 \times 2c_0$ [33, 110]. This second order phase transition is characterised by a peak in resistivity measurements and it is associated with a contraction of the Ti-Se bond of about 0.08Å (atomic displacements in Fig. 3.3: 0.085Å for Ti atoms and 0.028Å for Se atoms) [33]. In ARPES (Angle Resolved Photoemission Spectroscopy) measurements, this transition is seen as backfolded bands (Fig. 3.4): the Γ and L points are in fact connected by the new reciprocal lattice vectors due to the CDW transition [104]. This backfolding allows direct interaction between the p and d bands. Recently, it has been suggested that CDW in TiSe$_2$ can have a chiral symmetry based on STM and polarized optical reflectometry [41, 111, 112]. According to this model there is a different stacking along the c_0 direction

of three 1D-CDW, with density peaks shifted by $2c_0/3$ with respect to one another. A detailed theoretical description has been developed by van Wezel [113–115]. An excess of Ti has a strong influence on the CDW transition: the typical CDW peak in resistivity is slowly vanishing while the transition temperature is shifting towards slightly lower values – maximum temperature reduction of $\sim$30% for crystals grown at 1000°C – with the increase of the amount of intercalated Ti. The role of this excess of Ti will be discuss more in details in chapter 6 of this manuscript.

The origin of this CDW transition is still controversial. The first possible explanation was given by di Salvo $et\ al.$ [33] who suggested a nesting mechanism. However, early theoretical calculations [118–120] and ARPES measurements [106, 121–126] revealed that large parallel Fermi surface portions are not available. Another explanation was given by Hughes [35] who concentrated his attention on the lattice deformation induced by the CDW transition. He proposed a Jahn-Teller mechanism driven by a structural distortion from 1T towards 2H induced when lowering the temperature (green lines in Fig.3.3). In fact in an ideal octahedron ($1T$) the three lowest d-levels are degenerate, while they are split in two in a trigonal prism ($2H$) [36]. The slight twisting of the Se atoms is thus changing the lattice coordination inducing a down-shift of the Ti $3d$-bands and therefore lowering the total energy. A slightly different view suggests that the transition is driven by the shortening of the Ti-Se bond (dashed green lines in Fig.3.3) [36]. In this case the energy lowering does not occur in the Ti $3d$-bands but in the Se $4p$-bands, i.e. there is a lowering of the Ti-Se bonding levels. This second model is usually referred to as second-order [36] or indirect [37, 127] Jahn-Teller effect. A complete different point of view is at the base of the excitonic model proposed by Wilson [34]. This model is based on the electron-hole interactions between valence and conduction band separated by a very small indirect gap (semi-conductor) or band overlap (semi-metal). The low number of charge carriers induces a low screening of the Coulomb interaction between bands and makes it possible for excitons to condensate at sufficiently low temperature [104, 128]. A cooperation between a Jahn-Teller type mechanism and electron-hole coupling has also been proposed based on ARPES measurements [129] and theoretical models [37].

Pristine $TiSe_2$ becomes superconducting only under high pressure with a maximum transition temperature of 1.8 K at 3GPa [130]. X-ray scattering measurements under pressure show the existence of an incommensurate CDW phase transition above the superconducting dome [131].

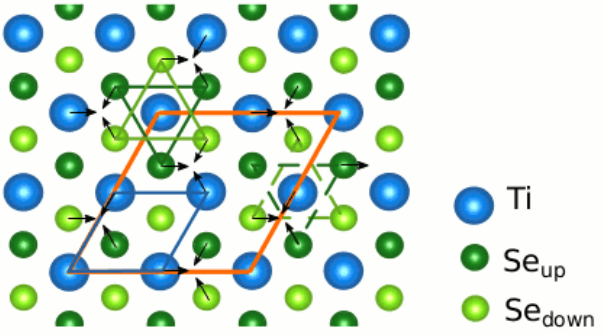

Figure 3.3: CDW lattice distortion in 1T-TiSe$_2$ (adapted from [33]). Small parallelogram: crystal unit cell; large parallelogram: CDW unit cell. Black arrows: atom displacements after the CDW transition. Triangles: Ti environments considered in the Jahn-Teller and indirect (dashed lines) Jahn-Teller mechanisms.

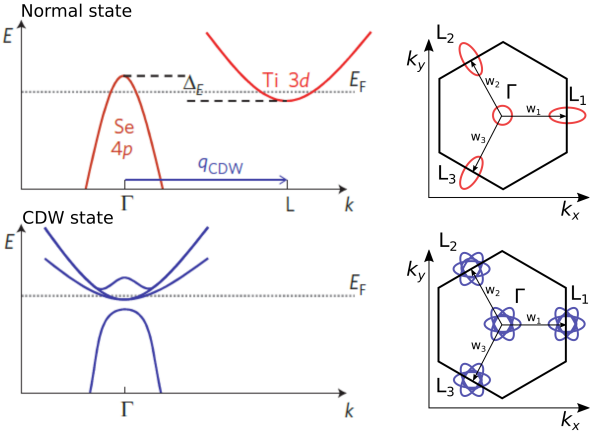

Figure 3.4: Model of the band structure of TiSe$_2$ in the normal and CDW states. After the CDW transition the L and Γ points become perfectly equivalent. In this schematic representation the spectral weight of the different bands is not considered (adapted from [116, 117]).

3.3 1T-Cu$_x$TiSe$_2$

As other TMDs, 1T-TiSe$_2$ can be intercalated with foreign species tuning the physical properties of the pristine material [38, 132, 133]. The main consequence of intercalation is a progressive suppression of the CDW transition, and, when copper is used [38], a new superconducting phase is induced as well, with a maximum T$_C$ of 4.1K at an optimal Cu concentration of x=0.08. The phase diagram of Cu$_x$TiSe$_2$ (Fig. 3.5a) is thus quite similar to the one of high temperature superconductors, heavy fermion and Fe-base superconductors [3, 134]. All these materials have in common the emergence of superconductivity close to an ordered phase with broken translational or spin rotational symmetry (see chapter 2). Cu$_x$TiSe$_2$ gives us the rare opportunity to study the transition from CDW to superconductivity on a surface suitable for STM and as a function of an easily controllable parameter: the amount of intercalated Cu. In the following we will revise what it is known about normal state, CDW and superconducting properties of this particular intercalated TMD.

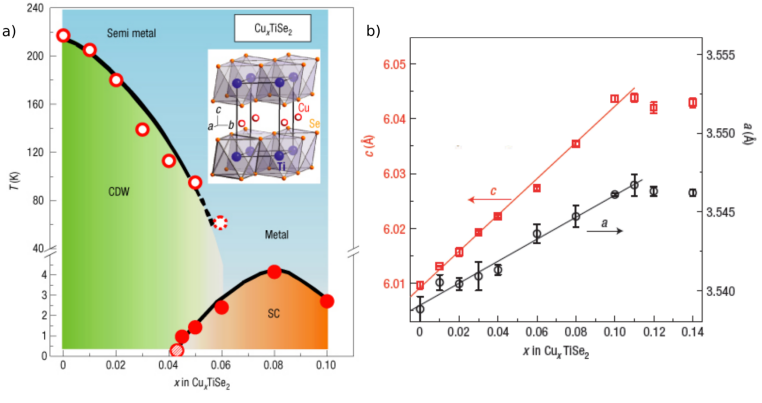

Figure 3.5: a) Phase diagram of Cu$_x$TiSe$_2$. Inset: Crystal structure. b) Cu content dependent lattice parameters c_0 (left scale) and a_0 (right scale) [38].

3.3.1 1T-Cu$_x$TiSe$_2$: normal state

X-ray powder diffraction measurements on intercalated crystals reveal a linear increase of the lattice parameters a_0 and c_0 [38, 135–137] up to x∼0.02, and no sign of Cu ordering in the lattice [136] (Fig. 3.5b). X-ray resonant photoemission and absorption spectroscopy [138, 139]

show no change neither in the chemical bond between Ti and Se atoms nor in the local symmetry and suggest that Cu atoms behave almost like free ions with both $3d$ and $4s$ electrons participating in the conduction process. Theoretical calculations [140] indicate that the formation of Cu-Se bonds can stabilize the transferred charge on Se atoms leading to a lowering of the Se-bands.

Cu intercalated samples are characterised by a high number of free carriers (10^{21} cm$^{-3} \leq n \leq 10^{24}$ cm^{-3} [38, 141–143]) compared to the pristine compound ($\sim 10^{20}$ cm^{-3} [33]), an increase in the normal state susceptibility [38], a decrease in the overall resistivity and a linear metallic resistivity curve for temperatures higher than the CDW transition [38, 135]. Cu intercalation mainly enhances the in-plane conductivity, increasing the anisotropy between the ab plane and the c direction [38, 135], as observed in cuprates [135, 144]. The residual resistivity ratio (RRR=ρ(300K)/ρ(5K)) increases from $\sim$2 to $\sim$5 with increasing Cu concentration from 0.015 to 0.11 [38, 135], a quite small value compared with the one of other superconducting dichalcogenide such as $2H$-$NbSe_2$ [135]. This is consistent with an enhanced scattering in the ab-plane due to the presence of a disordered distribution of Cu atoms [145]. Seebeck (S) [38, 135, 146] and Hall coefficients (R_H) [135, 136] measurements indicate that the charge carriers are n-type, thus compatible with electron doping from Cu to the Ti conduction band at the L point of the Brillouin zone. In addition, for crystals with no CDW transition - i.e. high Cu concentration - the absolute value of S decreases linearly with temperature and R_H shows a T-independent behaviour as expected for metallic compounds. The general decrease of the absolute value of R_H with increasing Cu concentration is another signature of a large number of charge carriers. Consistently with this picture, ARPES measurements at room temperature show the presence of an electron pocket at the L point, which is growing with the increase of Cu concentration [105, 147].

Local moment magnetism is not observed, confirming that the oxidation state of Cu is +1, since only Cu^{+2} is magnetic [38, 138, 146].

3.3.2 $1T$-Cu_xTiSe_2: CDW transition

X-ray diffraction studies [38] show that intercalation does not introduce any change in the CDW wave vector, and for Cu concentration higher than 0.04 [38, 135, 146] all the typical features of the CDW transition vanish. First of all, the peak in resistivity associated with the formation of the CDW superlattice, broadens and moves towards lower temperatures with increasing Cu concentration [38, 135]. Above the superconducting transition and in the absence of a CDW, the re-

sistivity displays a quadratic dependence on temperature, signature of a Fermi-liquid behaviour [135, 145]. Secondly, the drop in the susceptibility related to the CDW transition disappears with increasing Cu concentration [38]. In the pristine sample this drop is attributed to the reduction in electronic density of states that occurs on opening a gap at the Fermi level: hence adding Cu corresponds to a smaller number of gapped states. These changes in transport and magnetic properties are associated with a decrease in the folding of the Se $4p$ bands at L attributed to the CDW transition [105,106,147,148], sign of a lost long range order or a complete disappearing of CDW.

An STM study [149] shows that the proposed CDW chiral phase [111, 112] seems to be preserved even in presence of Cu up to a concentration of x=0.06, which is around the critical value at which CDW disappears. This would suggest that the transition between chiral and non-chiral phase could lie in proximity to the CDW critical point.

3.3.3 1T-Cu$_x$TiSe$_2$: superconducting transition

Specific heat measurements have been performed [38, 150] in order to determine if Cu$_x$TiSe$_2$ is a conventional superconductor following the Bardeen-Cooper-Schrieffer (BCS) theory [45]. Indeed the ratio $\Delta C_e(T_C)/\gamma T_C$ - where ΔC_e is the jump in the electronic contribution to the specific heat between normal and superconducting state and γ is proportional to the density of states at the Fermi energy - gives a value of 1.68, quite close to the BCS value of 1.43 [38]. In addition, magnetization and magnetoresistance measurements present the usual behaviour of type-II superconductors. Characteristic values of superconducting transition temperature T_C, BCS ratio, upper critical field H_{C_2}, superconducting anisotropy γ, London penetration depth λ and coherence length ξ are reported in Tab.3.2. Typical values for the Ginzburg-Landau parameter κ are found to be between 44 (6% Cu [141]) and 100 (8% Cu [38]) where $\kappa=\lambda/\xi\approx H_{C_2}/H_{C_1}$ and H_{C_1} is the lower critical field [38, 141, 145]. The estimated electronic mean free path l is $\sim$2nm [141, 142, 151] placing this material in the dirty limit ($l<\xi$), even if the temperature dependence of the penetration depth λ might be compatible with the clean limit [141]. The superconducting anisotropy $\gamma=H^{ab}_{C_2}(T=0)/H^{c}_{C_2}(T=0)$ is $\sim$1.7 except for underdoped samples (x$\leq$0.06) where it has a slightly higher value of $\sim$1.9 [145, 150, 151]. This value is lower than the one typically observed in other superconducting TMD (2H-NbSe2: $\gamma\approx$3) [151]. Thermal conductivity measurements [152] gave the first evidence for conventional s-wave symmetry, justified by the absence of a residual linear term in the in-plane thermal conductivity at temperatures approaching

zero. However, as it can be easily seen from Tab. 3.2, no consensus has been reached regarding the value of the BCS ratio $2\Delta/k_BT_C$ at least in the case of low Cu concentrations. As reported by muon-spin rotation, below x=0.08 the BCS ratio is doping dependent and lower than the standard BCS value of 3.5 [141, 146], revealing a possible multiple superconducting gap [146]. This is supported by a weak field dependence of the magnetic penetration depth λ, observed in underdoped samples [146]. A possible explanation is that a small superconducting gap might exist on the hole pocket at Γ with a decreasing contribution to the overall superfluid density at higher Cu concentrations. An alternative scenario is a single anisotropic gap at L: this gap might become more isotropic as charge is added to the system and the CDW vanishes, i.e. when larger portions of the Fermi surface are available for superconductivity [146]. In contrast, heat capacity measurements [150] reveal a constant BCS ratio of ~ 3.7, independent from Cu concentration, indicating the existence of a single s-wave superconducting gap that scales with T_C. Field dependent measurements of the thermal conductivity [152], the constant value of the anisotropy ratio γ and the temperature dependence of λ [141] are all compatible with a single gap s-wave BCS superconductor. Furthermore, ARPES measurements show that most of the electrons coming from Cu are filling the Ti $3d$-band: since the Se $4p$ band is fully occupied, only the Ti $3d$ band is left available for superconductivity possibly ruling out a multiple gap scenario [105, 152]. The vortex phase diagram [151] shows a broad doping-independent region of vortex liquid phase. Despite the atomic disorder induced by Cu atoms, only weak bulk pinning is observed even far from T_C [151] suggesting a uniform amplitude of the superconducting order parameter. This pinning remains weak also in the vortex solid phase.

3.3.4 1T-Cu$_x$TiSe$_2$: the phase diagram

One of the key questions regarding Cu_xTiSe_2 is whether CDW and superconductivity are interacting, coexisting or excluding each other. The phase diagram (Fig. 3.5a) of this material suggests a competition between the two phenomena, with the slow disappearance of the CDW dome giving way to the emergence of a superconducting dome [38]. The higher anisotropy value for x$\leq$0.06 might be also a sign of competition, since at this level of intercalation the CDW signature is still strong [151]. On the other hand, it is possible to describe a picture in which the rise of the chemical potential suppresses the CDW in an excitonic model while the increase of the density of states favours the superconductivity according to the BCS-Eliashberg scenario [45]. In

Parameter	x=0.06	x=0.07	x=0.08	x=0.1
$T_C(K)$	2.5 * 2.3 $^\bullet$ 2.8 †	3.9 $^\circ$	4.17 $^\triangleleft$	3.9 $^\diamondsuit$
$2\Delta/k_BT_C$	2.5 * 3.7 †	–	3.34$^\triangleleft$	–
2Δ (meV)	0.54 * 0.89 †	–	1.2 $^\triangleleft$	–
$H^c_{C_2}$ (T)	0.55 $^\bullet$ †	0.8 $^\circ$	0.85 $^\triangleleft$	0.6 $^\diamondsuit$
γ	1.8 †	1.7 $^\circ$	1.7 $^\diamondsuit$	–
λ_c(nm)	660 *	584 $^\circ$	441$^\triangleleft$	610 $^\diamondsuit$
ξ_{ab} (nm)	15 * 29 $^\flat$	21.3 $^\circ$	18$^\triangleleft$	23 $^\diamondsuit$

Table 3.2: Summary of Cu_xTiSe_2 superconducting parameters. T_C = superconducting transition temperature, $2\Delta/k_BT_C$ = BCS ratio, $H^c_{C_2}$ = upper critical field in the c direction, $\gamma = H^{ab}_{C_2}(T=0)/H^c_{C_2}(T=0)$ = superconducting anisotropy, λ = penetration depth, ξ_{ab} = coherence lenght in the ab plane. * [141], $^\bullet$ [152], † [150],$^\circ$ [145], $^\triangleleft$ [146], $^\diamondsuit$ [143], $^\flat$ [147]. Note: in Zaberchik *et al.* [146] x=0.081; in Kacmarcik *et al.* [150]: x=0.061); in Morosan et al. [38]: polycrystalline samples i.e. the value for H_{C_2} is intermediate between $H^{ab}_{C_2}$ and $H^c_{C_2}$.

this case CDW and superconductivity are unrelated and the presence of a dome is simply coming from two simultaneous effects due to doping: the shift of the chemical potential into the conduction band due to the donor character of Cu and the enhanced scattering for higher Cu concentrations [105, 152]. Finally, Raman scattering measurements [153] suggest the presence of a transition region ($0.04 < x < 0.07$ with x the Cu concentration) where there is a coexistence between superconductivity and a fluctuating CDW order. The x-dependent mode softening, associated with the reduction of the electron-phonon coupling, is attributed to the existence of a quantum critical point located around x=0.07. Further investigations are clearly necessary to have a complete understanding of the phase diagram of this compound.

3.4 Conclusion

In this chapter, after a short overview on TMDs, we have revised the properties of pristine $TiSe_2$ and Cu-intercalated $TiSe_2$. Even if this ma-

terial has been studied since the '60s, many questions still remain open, and only an exhaustive analysis with different techniques can help us in finding all the answers. Our contribution in this work is focusing on some of these questions, mainly related to the role of defects and excess Ti, the origin of the CDW transition, the local effects of intercalated Cu, and the relationship between CDW and superconductivity in Cu_xTiSe_2. Our point of view will be the one given by scanning tunneling microscopy and spectroscopy.

Chapter 4

Basic principles of Scanning Tunneling Microscopy and Spectroscopy

Based on quantum mechanical tunneling, the scanning tunneling microscope (STM) allows not only to collect images with atomic resolution, but also to perform spectroscopic studies at the atomic scale. After its invention in 1982 by Binnig and Rohrer [154], it became feasible to look at single atom impurities and to search for electronic homogeneities/inhomogeneities at the surface: Friedel oscillations [155, 156], CDW [100], gap and vortices in superconductors [3] are just some of the possible physical phenomena accessible with this instrument. In this chapter we present a basic theory of tunneling, which will be used to calculate the single-particle current. A more detailed theoretical description can be found in Chen's book [157] or in Berthod's lecture notes [44].

4.1 Electron tunneling

The physical concept behind an STM is quantum mechanical tunneling of electrons through a potential barrier [157]. While in classical mechanics, in order to have a flow of electrons between two metals in close proximity it is necessary to apply a potential difference higher than the work function ϕ of the metals, in quantum mechanics this is not necessary and electrons can tunnel through a potential barrier

(Fig. 4.1a). Indeed in quantum mechanics, we describe an electron by its wave function $\Psi(x)$. In one spatial dimension and in the presence of a potential $U(x)$, this electron wave function satisfies the following Shrödinger equation:

$$-\frac{\hbar^2}{2m}\frac{d^2}{dx^2}\Psi(x) + U(x)\Psi(x) = E\Psi(x). \tag{4.1}$$

In contrast to the classical case, this equation has a solution also for E smaller than $U(x)$. For a potential step such that $U(x < 0) = 0$ and $U(x > 0) = U$, this solution is:

$$\Psi(x) = \Psi(0)e^{-\kappa x} \tag{4.2a}$$

$$\kappa = \frac{\sqrt{2m(U-E)}}{\hbar}. \tag{4.2b}$$

This means that there is a finite probability ($|\Psi(x)|^2$) for the electron to penetrate the barrier in the $+x$ direction, and this probability decays exponentially with the barrier height. In addition to the physical solution reported in Eq. 4.2a for $x > 0$, the Schrödinger equation also admits a solution $\Psi(0)e^{\kappa x}$. In the case considered (potential step), this solution is unphysical, because not normalizable. However, for a potential barrier of finite width, both solutions are valid, and the wave function in the barrier is a linear superposition of them. The solution $\Psi(0)e^{\kappa x}$ describes an electron penetrating the barrier in the $-x$ direction, taking into account the fact that tunneling is a bidirectional process.

In an STM, this potential barrier is represented by a thin insulating layer (vacuum) between tip and sample. The bias difference between the two sides of the barrier is kept constant to have a net tunneling current in one direction. In summary, the main parameters in a tunneling experiment are: the tunneling current I_t, the bias voltage V, the tip-sample distance z and the work function ϕ.

4.2 Theory of tunneling

A tunneling experiment can be modelled as follow [44, 157]. Consider two isolated systems maintained at a fixed chemical potential, μ_L and μ_R, and each of them connected to an infinite charge reservoir (Fig. 4.1). We call them *left* (L,λ) and *right* (R,ρ) systems and, to have a concrete example in mind, they can be associated to tip and sample respectively. In this picture, each system can be described through its own Hamiltonian, $\mathscr{H}_L$ and $\mathscr{H}_R$, while the many body states in the L and R systems can be represented by the one-particle wave functions $\varphi_\lambda(\boldsymbol{l})$

and $\varphi_\rho(\boldsymbol{r})$ and their corresponding creation operators $c_\lambda^\dagger$ and $c_\rho^\dagger$. These systems are then brought together, avoiding the electrical short-circuit using an insulating layer – vacuum in our case – thus lowering the tunnel barrier from infinity to a finite value. In this way we can make cal-

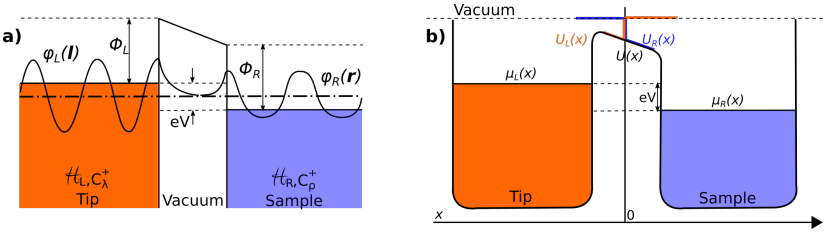

Figure 4.1: a) Schematic representation of a tunneling junction. b) Schematic representation of the potentials of the two systems (L and R).

culations based on two isolated systems instead of working with a more complicated coupled junction. However, the two parts are maintained at different chemical potentials. Hence, there is no thermal equilibrium between the two, making calculations too complicated. The solution is to assume that the two systems are always independent. Mathematically this means that the electron operators, $c_\lambda^\dagger$ and $c_\rho^\dagger$, always commute on both sides, even if the two systems are in contact: $[c_\lambda^\dagger, c_\rho] = 0$ and consequently $[\mathscr{H}_L, \mathscr{H}_R] = 0$. It has to be kept in mind that this is a tricky point, since it implies that the wave functions $\varphi_\lambda(\boldsymbol{l})$ and $\varphi_\rho(\boldsymbol{r})$ are orthogonal, though we need their overlap inside the barrier in order to have tunneling.

Using these assumptions, we can now write the Hamiltonian describing the tunneling of electrons from L to R:

$$\mathscr{H}_T = \sum_{\lambda\rho} T_{\lambda\rho} c_\lambda^\dagger c_\rho + h.c. \equiv \chi + \chi^\dagger \tag{4.3}$$

where the matrix element $T_{\lambda\rho}$ represents the amplitude for an electron to be transferred from R to L, or in other words from the state $|\varphi_\rho\rangle$ to the state $|\varphi_\lambda\rangle$.

In the next section, we will first introduce an expression for the tunneling current and then we will look more in details at how to calculate the tunneling matrix element. We will see that calculating this term is not obvious, since it cannot be derived from the properties of the two isolated systems for the reason mentioned above (orthogonal wave function).

4.2.1 Tunneling current

The tunneling current I_t can be defined as the rate of change of the number of electrons in the right system, $\dot{N}_R$, multiplied by the electron charge:

$$I_t = +e\langle \dot{N}_R \rangle \tag{4.4}$$

with $\langle ... \rangle$ a thermal average. Here and in the following we will use the convention $e = |e|$ and that the current is positive when electrons flow from left to right, i.e. from tip to sample. This current can be expressed in terms of the correlation functions of $\dot{N}_R$ and $\mathscr{H}_T$ and using the linear response theory it is possible to find that I_t can be split in two terms: the time-independent single-particle current I and the time-dependent Josephson current. This second term is different from zero only if both tip and sample are superconducting, so it will be ignored since we are only using normal metal tips. Using the assumption of two independent sub-systems to write the retarded correlation functions in terms of the spectral functions in the left and right systems, the current can be expressed as:

$$I = \frac{2\pi e}{\hbar} \sum_{\lambda\rho} |T_{\lambda\rho}|^2 \int_{-\infty}^{\infty} \mathrm{d}\omega [f(\omega - eV) - f(\omega)] A_\lambda(\omega - eV) A_\rho(\omega) \tag{4.5}$$

where $f(\omega)$ is the Fermi-Dirac function; A is the single particle spectral function, one for each system; $eV = \mu_L - \mu_R$ is the applied voltage.

In order to calculate this single-particle current it is thus necessary to have an expression for the matrix element $T_{\lambda\rho}$.

4.2.2 Bardeen's tunneling matrix

The tunneling matrix element has been first derived by Bardeen [158]. The essential idea [44, 157] is to deal with the two systems separately and use perturbation theory to solve the problem for the whole system. Therefore, instead of considering the total local potential of the junction $U(x)$ we will use the potential $U_L(x)$ and $U_R(x)$ (Fig. 4.1b) defined as:

$$U_L(x) = U(x) \;\; and \;\; U_R(x) = 0 \quad if \;\; x < 0 \tag{4.6a}$$

$$U_L(x) = 0 \;\; and \;\; U_R(x) = U(x) \quad if \;\; x > 0 \tag{4.6b}$$

implying that:

$$U(x) = U_L(x) + U_R(x) \tag{4.7a}$$

$$U_L(x) U_R(x) = 0 \tag{4.7b}$$

The wave functions $\varphi_\lambda(x)$ and $\varphi_\rho(x)$ are then satisfying the Schrödinger equation:

$$\left[\frac{p^2}{2m} + U_{L,R}(x)\right] \varphi_{\lambda,\rho}(x) = \varepsilon_{\lambda,\rho}\varphi_{\lambda,\rho}(x). \tag{4.8}$$

The potentials $U_{L,R}$ and the wave functions $\varphi_{\lambda,\rho}(x)$ are clearly different from $U^0_{L,R}$ and $\varphi^0_{L,R}(x)$ in the isolated systems, but we can assume that this difference is small allowing us to use standard time-independent perturbation theory. Considering the left system, after having closed the junction the perturbation acting on the state φ_λ is U_R. Performing a perturbative calculation, the only relevant term is:

$$\sum_{\rho\lambda} \langle\rho|U_R|\lambda\rangle c^\dagger_\rho c_\lambda + h.c. \tag{4.9}$$

where $\langle\rho|U_R|\lambda\rangle$ corresponds exactly to the matrix element we were looking for in Eq. (4.3). Using Eq. (4.8), and restricting ourselves to the region R where U_R is non zero and to the case of $elastic\ tunneling$ (ε_λ=ε_ρ), it is possible to find a general expression for this element:

$$\begin{aligned}
T_{\lambda\rho} &= \langle\rho|U_R|\lambda\rangle \\
&= \int_R dx \quad \left[\varphi_\lambda(x)\left(\varepsilon_\rho - \frac{p^2}{2m}\right)\varphi^*_\rho(x)\right] \\
&= \int_R dx \quad \left[\varphi^*_\rho \frac{p^2}{2m}\varphi_\lambda(x) - \varphi_\lambda(x)\frac{p^2}{2m}\varphi^*_\rho(x)\right] \\
&= -\frac{\hbar^2}{2m}\int_R dx[\varphi^*_\rho(x)\nabla^2\varphi_\lambda(x) - \varphi_\lambda(x)\nabla^2\varphi^*_\rho(x)] \qquad (4.10a) \\
&= -\frac{\hbar^2}{2m}\int_R dx\nabla\cdot[\varphi^*_\rho(x)\nabla\varphi_\lambda(x) - \varphi_\lambda(x)\nabla\varphi^*_\rho(x)] \\
&= -\frac{\hbar^2}{2m}\int_S [\varphi^*_\rho(x)\nabla\varphi_\lambda(x) - \varphi_\lambda(x)\nabla\varphi^*_\rho(x)]\cdot dS. \qquad (4.10b)
\end{aligned}$$

Eq. 4.10b means that the matrix element is related to the single-particle current through a surface separating the two electrodes. The last step is to have a model for the STM junction in order to be capable of writing the tip and sample wave functions, which appear in Bardeen's formula.

4.2.3 The differential conductance and the Local Density of States

Following Chen's approach, we can describe the STM junction as a contact between the apex atom of the tip and one atom from the sample surface [44, 157]. Hence, the wave functions in Bardeen's formula can be written as combination of atomic orbitals describing the atoms involved in the junction. The Schrödinger equation for electrons in vacuum is:

$$\frac{\hbar^2\nabla^2}{2m}\varphi_{\lambda,\rho}(x) - \frac{\hbar^2\kappa_{\lambda,\rho}^2}{2m}\varphi_{\lambda,\rho}(x) = 0 \tag{4.11a}$$

$$\text{with} \qquad \frac{\hbar^2\kappa_{\lambda,\rho}^2}{2m} = \phi_{L,R} - \xi_{\lambda,\rho} \tag{4.11b}$$

where $\phi_{L,R}$ are the tip and sample work functions. The easiest way to solve this problem is to use spherical coordinates and later to expand the wave functions on spherical harmonics. Therefore, if we consider an s-state ($l = m = 0$), we can write:

$$\varphi_s(x) \equiv \varphi_{00}(x) = C_{00}k_0(\kappa_s x)Y_{00}(\theta,\varphi) \tag{4.12}$$

$Y_{00}(\theta,\varphi)$ has a constant value, equal to $1/\sqrt{4\pi}$, while $k_0(\kappa_s x)$ is a Bessel function which can be rewritten using the Green's function of the operator $(\nabla^2 - \kappa^2)$:

$$(\nabla^2 - \kappa^2)g(x) = -\delta(x) \tag{4.13a}$$

$$g(x) = \frac{\mathrm{e}^{-\kappa x}}{4\pi x} = \frac{\kappa}{4\pi}k_0(\kappa x). \tag{4.13b}$$

Finally, the wave function for an s-state becomes:

$$\varphi_s(x) = \frac{\sqrt{(4\pi)}C_{00}}{\kappa_s}g(x). \tag{4.14}$$

Using this wave function, we can now calculate the matrix element $T_{s\rho}$ applying Eq. 4.10a. We have:

$$\begin{aligned}\nabla^2\varphi_s(x) &= \frac{\sqrt{4\pi}C_{00}}{\kappa_s}\nabla^2 g(x) \\ &= \frac{\sqrt{4\pi}C_{00}}{\kappa_s}(\kappa_s^2 g(x) - \delta(x)) = \kappa_s^2\varphi_s(x) - \frac{\sqrt{4\pi}C_{00}}{\kappa_s}\delta(x),\end{aligned} \tag{4.15}$$

and:

$$\nabla^2 \varphi_\rho^*(x) = \kappa_\rho^2 \varphi_\rho^*(x). \tag{4.16}$$

Inserting Eq. 4.15 and Eq. 4.16 in Eq. 4.10a, we obtain the following expression for the matrix element for an s-state tip:

$$T_{s\rho} = \frac{\hbar^2}{2m} \frac{\sqrt{4\pi} C_{00}}{\kappa_s} \varphi_\rho^*(0) - \frac{\hbar^2}{2m} \int_R \mathrm{d}x (\kappa_s^2 - \kappa_\rho^2) \varphi_\rho^*(x) \varphi_s(x). \tag{4.17}$$

In the case of elastic tunneling: $\kappa_s^2 = \kappa_\rho^2$ and the second term vanishes. Hence, we remain with:

$$T_{s,\rho} \propto \varphi_\rho^*(\mathbf{0}) \tag{4.18}$$

where $\mathbf{0}$ is the position of the apex atom. This result was found by Tersoff and Hamann, who first reported a calculation for the Bardeen's matrix element for a model of STM junction [159], and it is a fundamental step in order to interpret the differential conductance as the local density of states (LDOS) of the sample at the tip position. In fact, using this matrix element (Eq. 4.18) to calculate the single-particle current (Eq. 4.5), we obtain:

$$I \propto \int_{-\infty}^{\infty} d\omega [f(\omega - eV) - f(\omega)] \sum_\lambda A_\lambda(\omega - eV) \sum_\rho |\varphi_\rho(0)|^2 A_\rho(\omega). \tag{4.19}$$

By definition of the density of states we have:

$$\sum_\lambda A_\lambda(\omega - eV) = N_L(\omega - eV) \tag{4.20a}$$

$$\sum_\rho |\varphi_\rho(0)|^2 A_\rho(\omega) = N_R(\mathbf{0}, \omega) \tag{4.20b}$$

where N_L is the density of states of the left system (tip) and N_R is the local density of states of the right system (sample). Furthermore, if the tip has a structureless density of states, $N_L(\omega) = N_L(0)$, we obtain for the differential conductance at zero temperature:

$$\sigma = \frac{dI}{dV} \propto N_R(\mathbf{0}, eV) \tag{4.21}$$

which, as anticipated before, means that the differential conductance σ is directly related to the sample LDOS at the position 0 of the tip apex.

The fact that the LDOS is measured at the tip position, meaning few Å outside the surface, is an important point to take into account while

performing experiments. Indeed, as the wave functions decay exponentially outside the sample, the tunneling conductance also decreases exponentially when the tip-sample distance is increased. For a similar reason, if different states are involved in determining the sample LDOS, the differential conductance might change with the distance, since each of these states will decay on a different length scale.

4.3 Conclusion

In this chapter we did present a basic theory of tunneling starting from a tunneling Hamiltonian. Using the Bardeen's formula for the tunneling matrix element, we have been able to calculate the single-particle current in the specific case of a tip in an s-state. The main result is the theoretical proof that the differential tunneling conductance is proportional to the sample LDOS measured at the tip position.

Chapter 5

Experimental and Theoretical Methods

Low temperatures are fundamental ingredients for surface characterisation and for studying CDW and superconducting states and an ultra-high vacuum (UHV) environment is extremely useful to avoid contaminations. In this chapter, after an overview of our low-temperature STM laboratories, the growth technique used to fabricate TMD single crystals will be introduced, together with theoretical methods applied to simulate the STM data.

5.1 Low temperature STM

Samples surface analyses were performed in ultra high vacuum using an Omicron low temperature (LT) STM and a SPECS Joule-Thomson (JT) STM. Typical base pressures were in the low 10^{-11} mbar for the LT-STM and low 10^{-10} mbar for the JT-STM. TMDs do not have a highly reactive surface [30], however UHV is still of extreme importance to study intrinsic defects avoiding any external contamination. At the same time, low temperature measurements are necessary to study CDW and superconductivity. In addition they guarantee low thermal vibration and better spatial and energy resolution. To reach low temperatures, the STM head is thermally connected to a two vessels cryostat. The inner one is in direct contact with the head and it can be refilled with liquid nitrogen (77 K) or helium (4.2 K), while the outer one is always refilled with liquid nitrogen. In the case of superconducting crystals (Cu_xTiSe_2 with $x > 0.04$), measurements at temperature be-

low 4K were required in order to study the superconducting gap. For this reason, these measurements were performed in the JT-STM where a base temperature of 1.1K can be reached. Such a low temperature is achieved using the Joule-Thomson effect, which describes a peculiar behaviour of non-ideal gases. In short, this effect consists in a temperature lowering induced by an adiabatic expansion of a gas (He in our gas) from a high pressure region to a low pressure region kept at a temperature below the gas *inversion temperature* ($\sim$40K for He) [160–162]. To isolate the head from the rest of the chamber preventing heat transfer, two (LT-STM) or three (JT-STM) radiation shields are attached to the vessels. Fig. 5.1 shows an overview of the JT-STM laboratory. In both LT- and JT-STM systems, samples are inserted through a load lock connected to a roughing pump and a turbo molecular pump in order to obtain a good level of vacuum (10^{-8} mbar) in half day. The load lock is connected to a preparation chamber equipped with a heating stage, evaporators and, in the case of the Omicron systems, other surface analysis instruments: reflection high energy electron diffraction (RHEED), low energy electron diffraction (LEED) and X-ray photospectroscopy (XPS). From the preparation chamber, samples can be easily moved with a transfer arm to the STM chamber where they are measured. In the LT-STM, the sample is kept fixed while the tip is mounted on a standard piezo-tube scanner [157] and can be moved in the plane thanks to a xy-table actuated by slip-stick piezo motors that allow coarse motion. In the JT-STM, the tip is at a fixed position in the xy-plane while the sample can be moved in the x-direction. At the end of this work, the JT system has been upgraded with a new Tyto head from SPECS, which allows also non-contact atomic force microscopy. Since the measured tunneling current is given by a convolution of the DOS of both sample and tip (Eq. 4.19), tips with a featureless DOS are generally chosen to study the intrinsic properties of a material. The metal used to fabricate tips are usually W, PtIr, Ir or Au. To avoid vibrations and consequently noise, the entire system is suspended on air-legs, and the head is suspended with springs and damped by an Eddy current damping stage.

The main parameters we can control in an STM experiment are the tunneling current I_t, the bias voltage V and the tip-sample distance z. In the following sections we will see how to tune these parameters to perform different kind of measurements [3, 157].

5.1.1 Topography

In the topographic mode, an image is reconstructed using the dependence of the tunneling current I_t from the tip-sample distance z. In Fig. 5.2 is reported a sketch of the most used *constant-current mode*

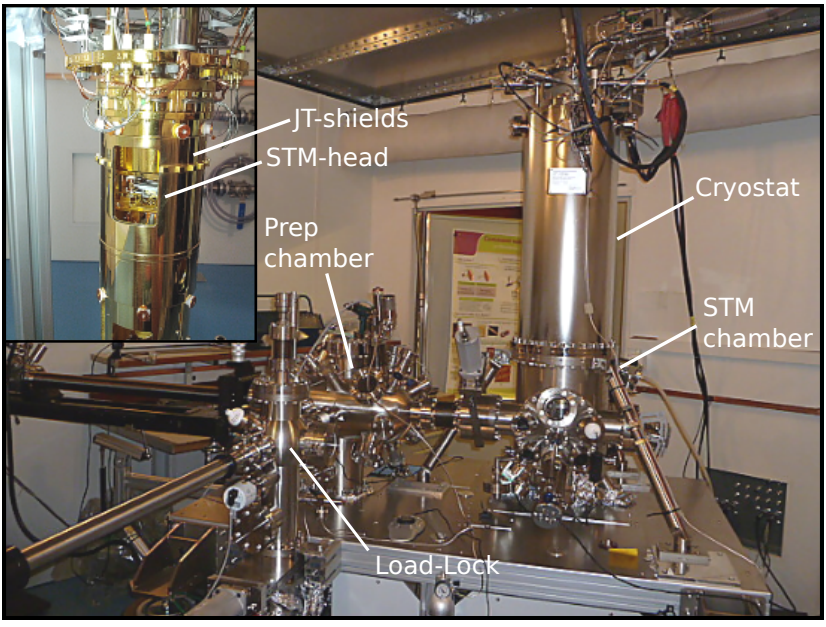

Figure 5.1: Overwiew of the SPECS-JT laboratory. Inset: The JT-STM head with JT-shields on.

together with two examples of real data. In this case, after applying a certain bias, the current between tip and sample is kept constant thanks to an electronic feedback loop that controls the tip-sample distance. In the perfect case of an homogeneous density of states (DOS), we can use the distance adjustment induced by the feedback to reconstruct the surface topography. In this operating mode, the scan speed is limited by the feedback loop bandwidth (kilohertz range).

A second operating mode consists in keeping the distance fixed (feedback loop turned off) and registering the variation in the current. In the ideal situation, recording I_t as a function of position will correspond to the surface topography. This method, called *constant-height mode*, allows faster image acquisition since we are not limited by the feedback loop response rate, but only by the bandwidth of the preamplifier and amplifier system. However, it can be used only on extremely flat surfaces to avoid any damage to the tip apex, as it could happen in presence of high surface steps running perpendicular to the scan direction. The information in the z-direction is lost, unless we know the local work-function ϕ, which can be used to reconstruct the surface corrugation since $z(x, y) \sim \ln I_t(x, y)/\sqrt{\phi}$.

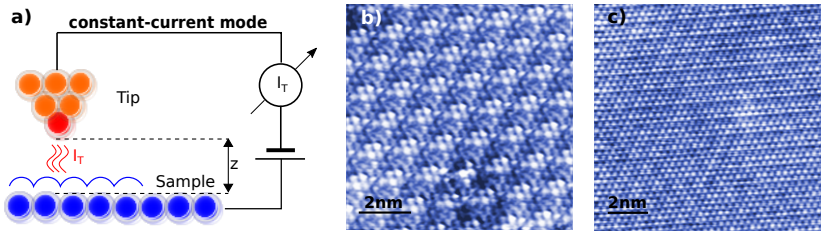

Figure 5.2: a) Constant current mode: the tip is scanning the surface while the current is kept constant adjusting the tip position in the z direction through a feedback loop. b) and c) are STM image examples obtained in the constant current mode. b) $1T$-TaS_2: atomic corrugation and commensurate CDW with wavelength $\lambda_{CDW} \simeq 3.606a_0$ (V=500mV , I_t=50pA, T=78K, cut PtIr tip). c) $2H$-$NbSe_2$: atomic corrugation and nearly commensurate CDW with wavelength $\lambda_{CDW} \simeq 3.05a_0$ (V=-100mV , I_t=100pA, T=5K, cut PtIr tip).

5.1.2 Spectroscopy

An STM can be used also to perform scanning tunneling spectroscopy (STS). In this case the tunneling current is recorded as function of the bias voltage. During the acquisition of an $I(V)$ curve, the feedback loop is turned off to keep the tip-sample distance constant. Applying a positive bias voltage V to the sample, electrons will tunnel from the tip states to the unoccupied sample states, while using negative bias, electrons will tunnel from occupied sample states to tip sates. The resulting tunneling conductance $dI(V)/dV$ is proportional to the LDOS (see chapter 4 of this manuscript and [44, 157]). There are two ways to obtain dI/dV spectra: numerical differentiation of $I(V)$ curves or a lock-in amplifier technique. In the second case, a small ac-voltage modulation $V_{ac}\cos(\omega t)$ is superimposed on the sample bias V. The measured quantity is the corresponding modulation in the tunneling current. A simple Taylor expansion of the tunneling current shows that the component at frequency ω is proportional to the differential conductance:

$$I = I(V) + \left(\frac{dI}{dV}\right) V_{ac}\cos\omega t + O(V_{ac}^2). \tag{5.1}$$

This is true for $V_{ac} \ll V$ and if $I(V)$ is smooth enough. Typical values for V_{ac} are in the few hundreds μV range, and a general rule for optimal energy resolution is that it should never be greater than $k_B T$. The advantage of this technique is that the measurement sensitivity can be enhanced, since the frequency ω is selected far from the noise frequencies.

5.1.3 Spectroscopic imaging

Defining a uniform grid of points on the sample surface, it is possible to run a *current-imaging tunneling spectroscopy* (CITS) experiment [163]. During this measurement the bias voltage is set to a certain value V_{im} and the tip scans the sample surface like in usual topographic imaging. At each point of the grid, the tip position is frozen and the voltage is swept to record an $I(V)$ (or a dI/dV or both). After the spectroscopy measurement, the bias voltage is set back to V_{im} and the feedback is turned on again to continue the surface scan. At the end the result will be a topographic image measured at V_{im} and a set of simultaneous spectroscopic images. A first example of the application of this technique is the measurement of the vortex-core states in $2H$-$NbSe_2$ [164, 165]. Another example is the study of Friedel-like spatial oscillations of the LDOS induced by the scattering of electrons by impurities [156, 166]. A Fourier Transform analysis of spectroscopic maps, characterised by a large enough field of view and high enough spatial resolution, allows k-space resolution [21, 167]. The Fermi-surface information extracted with this technique are compatible with ARPES, but with additional data about the empty-states. This powerful technique has been first applied to study the surface states of Be(0001) [168] and later extensively used on high T_C superconductors [21–24, 85, 169] and has recently been applied also on $2H$-$NbSe_2$ [25].

5.2 Sample growth, characterisation and surface preparation

$1T$-$TiSe_2$ and $1T$-Cu_xTiSe_2 single crystals were grown by iodine vapour transport by Alberto Ubaldini from University of Geneva and Helmut Berger from École Polytechnique fédérale de Lausanne (EPFL). In this method the precursor elements - Ti and Se for pristine samples - are sealed in an ampoule under vacuum ($\sim \times 10^{-5}$ mbar). This ampoule is heated up keeping a thermal gradient such that the side containing the starting materials is always at a temperature higher (source temperature) than the sublimation temperature of these compounds, while the other side is maintained at a lower temperature (growth temperature). In this way Se and Ti vapours migrate towards the colder side, where they react and crystallise into the $1T$-$TiSe_2$ phase. However, since the equilibrium vapour pressure of Ti is quite low even at high temperature, this method often generates only small crystals ([33, 170]). For this reason it is a common practice to add a “transport agent" to the starting mixture - molecular iodine in our case - with the role to react

with Ti and create highly volatile compounds: mainly TiI_4 and TiI_2. In this way titanium atoms can easily migrate to the cold side creating crystals of $TiSe_2$ while iodine is free to transport other Ti restarting the cycle. At the end of the process iodine mainly crystallises on the ampoule walls. Iodine can be easily removed from crystals with cycles of ultrasonic baths, first in acetone and then in ethanol. From X-Ray diffraction measurements (XRD) and Energy Dispersive X-ray analysis (EDX) there is no sign of a new phase $TiSe_{2-x}I_x$, even if a small contamination is still possible. Adding Cu to the starting mixture and tuning the growth parameters allow the growth of Cu intercalated samples.

The main parameters that can be used to control the growth are the source and growth temperature, the temperature gradient, the growth time and the ratio Ti/I_2. It has been shown by di Salvo *et al.* [33] that changing these parameters, and especially the maximum high temperature, is possible to tune the amount of intrinsic defects and CDW transition temperature. This point will be analysed and discuss in chapter 6.

All crystals (Fig. 5.3a) were fully characterised with the following techniques:

1. EDX: to determine the chemical composition
2. X-rays: to determine the crystal structure
3. Transport: a standard four-probe technique used to determine the CDW transition temperature
4. SQUID: used on Cu intercalated samples to determine the superconducting transition temperature

For the STM measurements, to look at a clean surface, samples were cleaved in low vacuum in the load lock, using a scotch tape or a post glued on top of it with a conductive epoxy glue. The cleaving process is getting more difficult with the increase of the Cu content: while pristine $1T$-$TiSe_2$ usually cleaves quite easily, leaving exposed large terraces, $1T$-Cu_xTiSe_2 is slightly harder to break and the surface often exhibits “nano-terraces", 10-nm width or even less (Fig. 5.3b and c).

5.3 DFT modelling

The contrast in an STM image is due to a convolution of both topography and electronic structure. A way to distinguish different chemical species is to compare the STM micrographs with Density Functional

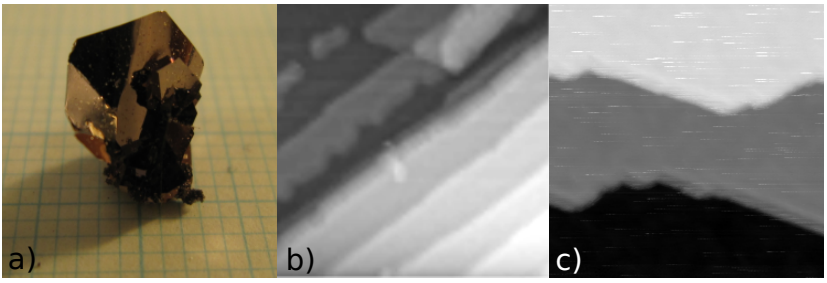

Figure 5.3: a) $1T$-$TiSe_2$ crystal. Growth temperature 800°C, ratio Ti : I_2 = 0.05, time = 24h. *Image courtesy of Dr. Alberto Ubaldini*. b) STM image of a 50×50 nm^2 surface of a $Cu_{0.07}TiSe_2$ single crystal : one-layer-nanoterraces are visible at the surface (V=100mV, I_t=60pA, T=4K). c) STM image of a 50×50 nm^2 surface of a $Cu_{0.07}TiSe_2$ single crystal : three terraces one layer thick (V=200mV, I_t=30pA, T=4K).

Theory (DFT) calculations [171, 172]. All DFT simulations presented in this work were performed by Dr. David R. Bowler and his team from University College London (UCL) and London Centre for Nanotechnology (LCN).
DFT model calculations were performed using the plane wave pseudopotential code VASP [173, 174], version 5.3.3. Projector-augmented waves [175] were used with the PBE [176] exchange correlation functional and plane wave cut-offs of 211eV ($1T$-$TiSe_2$, I substitutional) and 400eV (O). In the first model – DFT for defects identification [39] – two cell sizes were used: 12.26Å×14.16Å (small cell) and 24.52Å×28.32Å (large cell). The $1T$-$TiSe_2$ surface was modeled with four layers (for small cells) or two layers (for large cells) with the bottom layer of Se fixed. A Monkhorst-Pack mesh with 4×4×1 and 2×2×1 k points was used to sample the Brillouin zone of the small cell and the large cell respectively. In the second part – defects in presence of CDW and Cu intercalation [40] – the cell size was 28.035Å×28.035Å. The $1T$-$TiSe_2$ surface was modeled with two layers only and the bottom Se layer fixed. A Monkhorst-Pack mesh with $2 \times 2 \times 1$ k-points was used to sample the Brillouin zone of the cell. In all cases, the parameters gave energy difference convergence better than 0.01 eV. During structural relaxations, a tolerance of 0.03eV/Å was applied. STM images were generated using the Tersoff-Hamann approach [159] in which the current $I(V)$ measured in STM is proportional to the integrated LDOS of the surface using the BSKAN code [177].

Chapter 6

Intrinsic Defects and CDW in pristine 1T-TiSe$_2$

Physical properties of semiconductors/semimetals can be strongly influenced by the presence of dopants. The ability of controlling the nature of single dopants and their density has been the essential part in the advent of the semiconductor technology and the success of silicon technology for the development of new devices [26, 27]. A complete characterisation of intrinsic defects was still missing on 1T-TiSe$_2$, even if they strongly perturb the CDW transition in transport measurements (see chapter 3 and [33]). STM and STS are the perfect tools to get information on structural and spectroscopic properties at the atomic scale and comparison with DFT models allows to identify the atomic species most likely to be at the origin of a given STM pattern. Furthermore, these impurities/defects can be used as probes to gain insight into the electronic ordered phases of a material [20]. Indeed, STM has revealed a distorted superlattice in 1T-TaS$_2$ [178, 179] and a finite CDW amplitude in proximity of intrinsic defects in 2H-NbSe$_2$ above the bulk T_{CDW} [19].

In the first part of this chapter, a combined STM/STS characterisation of the intrinsic defects in 1T-TiSe$_2$ in the absence of CDWs is presented. All the experimental data are backed with DFT calculations. Then, in the second part, we report a detailed STM/DFT study of CDW in presence of these single atom defects. Most of the material shown in this chapter has already been published [39, 40]. The analysis of these data was done in collaboration with the group of Prof. P. Aebi from the University of Fribourg and of Dr. D. R. Bowler from University College

London.

6.1 Defects characterisation

This study has been carried out on stoichiometric crystals grown at 575°C and on crystals grown at 650°C and 900°C corresponding to an excess Ti up to 1.5%. In transport measurements this excess of Ti is reflected in an over 30% lowering of the typical peak in resistivity attributed to the CDW transition (Fig.6.1a and [33]). A model of the $1T$-$TiSe_2$ lattice is presented in Fig. 6.1b. The positions of different native defects (A-D) are shown, and, as we will see in the following, they correspond to Se surface vacancies (A), iodine (B) and oxygen (C) substitutions for bulk Se and titanium intercalated into the VdW gap (D).

All STM measurements were taken with a cut PtIr tip in constant current mode by applying a bias voltage to the sample. To avoid the contribution due to the CDW, micrographs were taken at $V_{bias} = \pm$ 1 V, far from the CDW gap which opens just below the Fermi energy and has a width (2Δ) of $\sim$100 meV [117, 128, 149, 180]. Indeed, at these bias voltages the CDW is not resolved in STM images. The differential conductance spectra were recorded using the standard lock-in method (bias modulation 20mV peak to peak at 965 Hz).

6.1.1 Defects signature in topography

STM micrographs of the $1T$-$TiSe_2$ surface are reported in Fig.6.2. The sample cleaving takes place in the van der Waals gap, exposing the topmost layer consisting of Se atoms (Se_{up}) [181]. However, relating an STM micrograph to the actual topography is not straightforward, since an STM image is a convolution of topography and pure electronic effects. If at the Fermi level there is a contribution coming also from the transition metal d-orbitals, as it happens for TMDs like $2H$-$NbSe_2$, $1T$-TaS_2 and also $1T$-$TiSe_2$, it is not clear a priori which layer the STM contrast is coming from [182–184]. We have been able to conclude that our STM micrographs can be attributed to Se atoms based on several considerations: first of all in filled-state images the main contribution to the tunneling current is coming from the $4p$ Se orbitals [185]; secondly, filled- and empty-state STM images show the same atomic symmetry and positioning (Figs.6.2c and d); finally, as we will see, the Se vacancies (defect A) are always in perfect registry with the lattice imaged by STM and all other defects signatures are compatible with a view from the topmost Se layer.

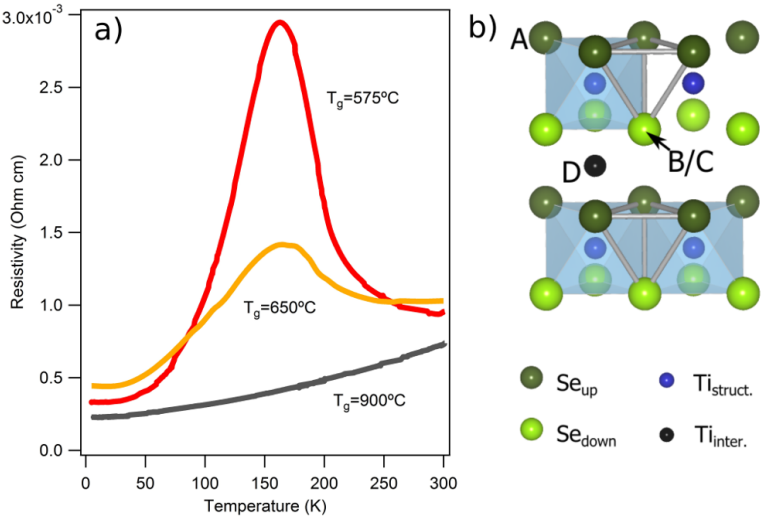

Figure 6.1: a) Resistivity measurements performed with a standard four probe technique on crystals grown at 575°C , 650°C and 900°C *Courtesy of A. Ubaldini and C. Barretau*. b) Ball-and-stick model of the $1T$-$TiSe_2$ lattice showing the positions of the native defects [39, 40].

Three distinct defects are clearly resolved (A, B, C) in the stoichiometric sample (Fig.6.2a and Fig.6.2b recorded at -1V and +1V respectively), while a fourth kind of defect D is detected on the sample grown at 650°C (Fig.6.2c recorded at -1V). Considering each protrusion and depletion as an atomic defect, a statistical estimation gives a density of 1%-2% of native defects in the stoichiometric sample. Hence these defects can strongly affect the electronic properties according to their doping nature.

Defects A, B and C appear like depletions in filled-state images (Figs.6.2a,c) with small variations in shape and darkness ($\Delta z_A > \Delta z_B > \Delta z_C$). The discrimination between defects A, B and C is possible only in empty-states images (Figs.6.2 b, d, e). Indeed, at positive bias defect A appears like a hole, defect B looks like a bright threefold star (Fig.6.2 b), while defect C corresponds to a bright central spot surrounded by three depletions. However, the ability to probe defect B strongly depends on the tip sensitivity to its associated orbitals. This explains why in Fig.6.2d it is almost invisible, while it reappears in Fig.6.2e acquired on the same surface after a slight modification of the tip apex. Defect D is visible only in filled-state images like a bright set of three atomic sites (Fig.6.2c), and it can be directly related to the ex-

cess of Ti in $Ti_{1+x}Se_2$. Indeed, only this defect is electron donor and, as expected [33], the density of this type of defect is higher in the crystal grown at 900°C than in the one grown at 650°C .

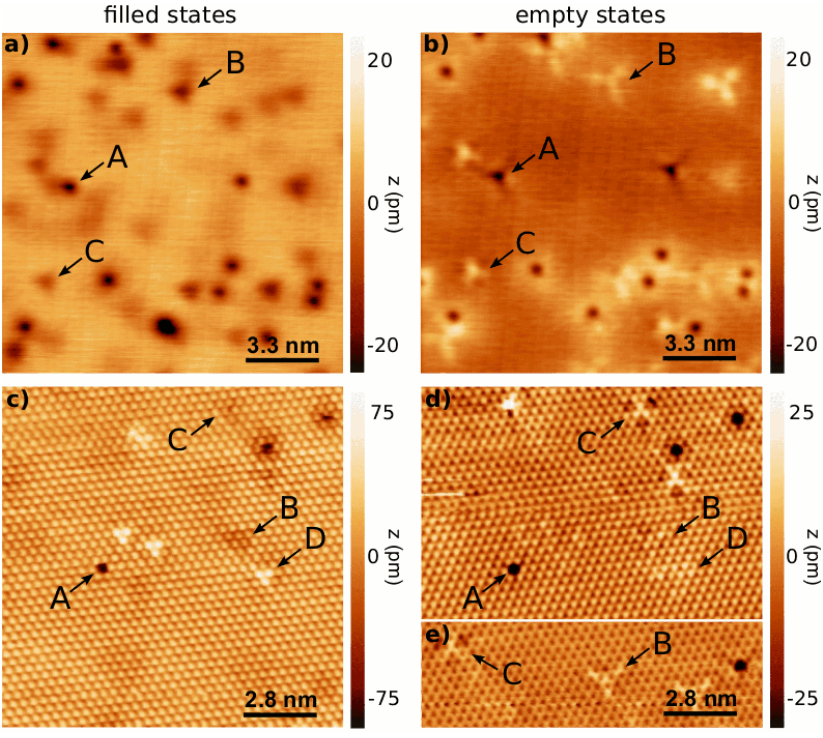

Figure 6.2: Filled and empty-state STM images of the same area of stoichiometric 1T-$TiSe_2$ grown at 575°C [(a) and (b)] and of Ti self-doped 1T-$TiSe_2$ grown at 650°C [(c) and(d)]. STM image (e) is from the same surface as (c) and (d) with another tip termination. Bias voltages : [(a) and (c)] -1 V and [(b), (d), (e)] +1 V. I_t=0.2 nA, T=4.7 K. Different defects are labelled A, B, C, D. *Image adapted from [39].*

High resolution STM micrographs of the 4 defects (middle row) are reported in Fig. 6.3, together with simulated STM images (bottom row) and the schematic top view representation of the structural conformation (top row). Based on the donor or acceptor character of the defect, only the most significant bias voltages are considered. Indeed, filled- and empty-state STM images can be used for highlighting donors and acceptors respectively, when protrusion and depletion do not correspond to simple topographic features [186].

Since defect A appears as a depletion at all bias voltages between

-1 and +1 V (Fig.6.2), it is attributed to a hole in topography, which is equivalent to a Se vacancy in the outermost Se layer (Se_{up}). Indeed, the atomically resolved STM micrograph of defect A (Fig.6.3A, center row) is in perfect agreement with the DFT simulation (Fig.6.3A, bottom row). Defects B and C are both centred at the atomic position of

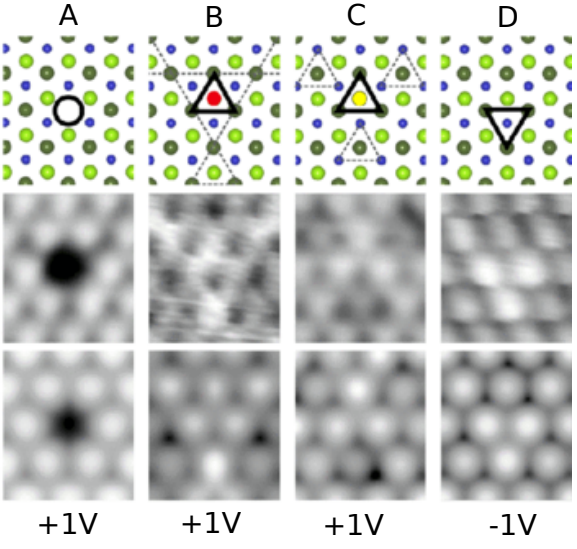

Figure 6.3: Atomically resolved STM micrographs (central row) (1.23 × 1.06 nm^2, I_t=200 pA, T=4.6 K), DFT simulated STM micrographs (bottom row), and schematic representation (top row) for the four kinds of native defects in 1T-$TiSe_2$. (A) Missing Se_{up} atom (Se in top layer), (B) Substitution of Se_{down} atom by an iodine atom, (C) Substitution of Se_{down} atom by an oxygen atom, (D) excess Ti intercalation. *Image adapted from [39].*

a Se atom belonging to the Se layer just above the VdW gap (Se_{down}) (Figs. 6.3B and C), and this is confirmed by the fact that they have the same relative orientation in all micrographs (Figs.6.2b,d,e). While at negative bias they appear like depletions, they show a different redistribution of the electron density at +1 V (Fig.6.2). Defect B corresponds to a bright threefold protrusion in all empty-state STM micrographs, thus showing an electron acceptor character (see Figs. 6.2b,d,e, and 6.3B). Iodine, a more electronegative element compared to Se, is used for the crystal growth and a residual iodine concentration of around 0.3 at.% (percentage of iodine atom relative to the total number of atoms) is unavoidable (see chapter 5 and [33]). Therefore, defect B

has been associated with iodine substitution for a Se atom belonging to the second Se layer. In fact, the presence of a stronger electronegative species increases the probability to inject electrons above this defect. As a consequence of this more electronegative element in the structure, the three neighbouring Ti atoms also have a lower negative charge. This affects the charge transfer to the other Se atoms since they should have less negative charge than in the absence of defects. The scanning tunneling microscope is more sensitive to the topmost layer and, therefore, it observes these modifications of the charge transfer via an increased probability of filling electrons on these Se atoms, which appear as protrusions in STM images at 1 V. The simulation of an I substitution (Fig.6.3) shows a similar behaviour.

In empty-state STM micrographs, defect C has also a bright signature (Figs. 6.2b, d, e, and 6.3C), characterised by a strong increase of the density of states localised on three neighbouring Se atoms of the topmost layer and three surrounding depletions. An oxygen substitution for a Se atom in the second layer is a good candidate since O has the same valence of Se and is a common impurity during the growth process. This hypothesis is confirmed by DFT calculations for O substitution (Fig. 6.3C, bottom row).

No substitution by iodine or oxygen has been observed in the topmost selenium layer. This is probably a consequence of the desorption of the least stable substituent shortly after cleaving at room temperature. Furthermore, this explains why Se vacancies are observed only in the topmost layer.

Defect D, which in filled-state STM images (negative bias voltages below -0.2 V) appears as a bright protrusion (Fig. 6.2c), corresponding to three bright neighbouring Se atoms of the outermost layer in the atomically resolved micrograph (Fig. 6.3D), becomes almost invisible (Fig. 6.2d) in empty-state STM images (positive bias voltages above 0.3 V). This means that defect D has an electron donor character, coinciding with the presence of an additional Ti atom, which locally modifies the hybridization with neighbouring Se atoms [187]. A comparison with total energy calculations shows that the additional Ti atoms should be placed in the VdW gap and in the alignment of Ti atoms from a top view (Figs. 6.1b and 6.3D, top row). The DFT simulation of an intercalated Ti atom in this conformation is in agreement with experiments. No intercalated Se atoms or Ti vacancies have been observed in our crystals.

6.1.2 Spectroscopic signature of defects

In Fig. 6.4 we show the differential tunneling conductance (dI/dV) measured on the atomic defects identified in the previous section. All spectra have been recorded in the CDW phase (4.7 K), where a gap (∼100mV [117, 128, 149, 180]) opens slightly below the Fermi level.

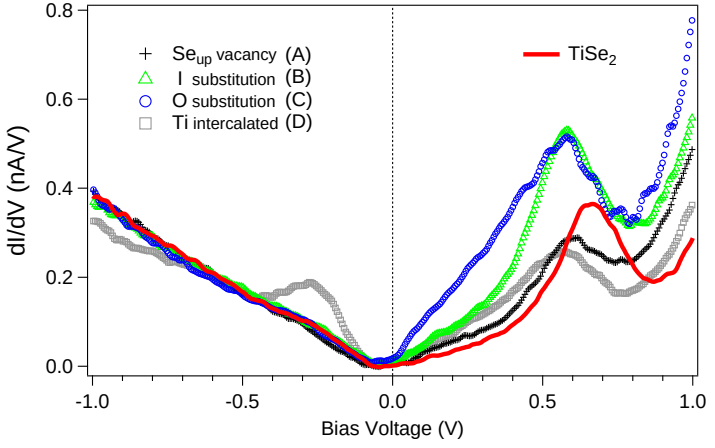

Figure 6.4: Experimental dI/dV curves obtained on 1T-TiSe2 and on top of the different defects. The red curve is obtained far away from the observed defects. (Averaging 10 spectra for each curve, T=4.6 K, $V_{set} = -1.1$ V, $I_t = 0.2$ nA). *Image adapted from [39].*

In the occupied states (negative bias voltage), all defects show almost the same behaviour of the LDOS as defect-free regions of 1T-TiSe$_2$, except for sites with intercalated Ti (defect D). In fact, defect D presents a well defined peak in occupied states. Therefore, while defects A-C do not strongly perturb the $4p$ Se bands below the Fermi level, the strong peak associated with defect D suggests the presence of a localised state that originates from the intercalated titanium $3d$ orbitals. The tunneling characteristic is consistent with the donor character of intercalated Ti (Figs. 6.2c and 6.3D).

Comparing the tunneling spectra of defect B and the stoichiometric 1T-TiSe$_2$ surface, it appears that an upward bending of the spectrum of the stoichiometric 1T-TiSe$_2$ surface in the empty-state region can bring both spectra to a match. Such a bending may be interpreted in terms of a local band bending of the structural $3d$ Ti bands, related to a strong modification of the local electronic potential. This local band bending would also explain the strong acceptor behaviour of this defect. The

spectrum acquired on defect C presents an even higher increase of the density of states in the unoccupied states than defect B. This might be due to a local shift of the titanium $3d$-bands towards the Fermi level induced by the strong electronegativity of oxygen.

6.2 CDW in presence of single atom defects

In the next sections, we will focus on the CDW instability in presence of single atom defects. If not specifically indicated, measurements were performed on crystals grown at 650 °C. All STM measurements were taken with a cut PtIr tip in constant current mode by applying a bias voltage to the sample. The defect nomenclature (A-B-C-D) is the same used in the previous section. In this work the DFT simulations are more precise, compared to the ones used in the previous section, since a larger cell has been used for calculations (see chapter 5).

6.2.1 Topography of single atomic defects in presence of CDW

An example of the $2a_0 \times 2b_0$ CDW superlattice is reported in Fig. 6.5a, while a region rich in defects, especially Ti in excess, is shown in Fig. 6.5b. Fig. 6.6 shows two high resolution STM micrographs of $1T$-$TiSe_2$ obtained at T=4.7K. They were taken simultaneously at positive and negative sample bias (positive bias in forward scan and negative in backward scan), and therefore we can assume that the tip was exactly the same for both micrographs. The bias voltages of ± 150mV have been selected to have a simultaneous resolution of the CDW and atomic lattice features at opposite polarities. Small variations in defect appearance between Fig. 6.6a and Fig. 6.5b are compatible with the different setpoint parameters (high current in Fig. 6.5b).

As we have seen in the previous section in the absence of a CDW ($V_{bias} = \pm 1$V) [39], DFT modelling allows us to identify the atomic lattice seen in STM maps with the Se surface layer also in presence of CDW ($\pm$150mV) by assigning the observed vacancies (defect A) to missing Se surface atoms. The commensurate in-plane $2a_0 \times 2b_0$ modulation (Fig. 6.7a,b) is in perfect registry with the Se atomic lattice, indicating that the CDW charge modulation detected by STM resides in the Se layer. This is an important result which clarify the debate about the location of the CDW modulation and the meaning of STM images in these materials. Indeed, STM measurements reported an asymmetry in the Se atom contrast that was attributed to a CDW located in the Ti plane [100, 185]. Another interpretation based on recent theoretical

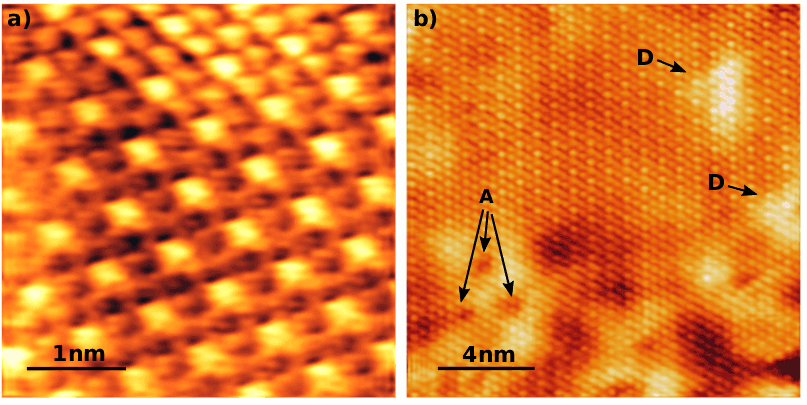

Figure 6.5: *a*) STM micrograph of a clean surface of $1T$-$TiSe_2$ single crystal grown at 575°C showing a perfect $2a_0 \times 2b_0$ CDW superlattice ($V_{bias} = -100$mV, I_t=1.5nA, T=78 K). b) STM micrograph of $1T$-$TiSe_2$ single crystal grown at 650°C (V_{bias}=100mV, I_t=700pA, T=4.7K).

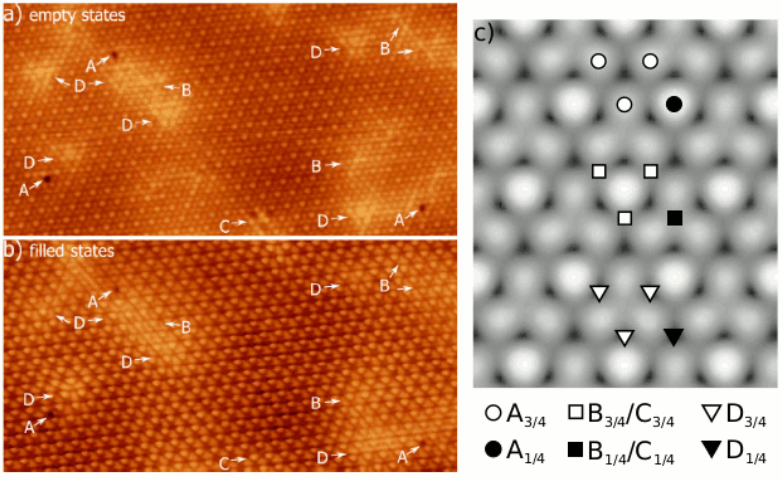

Figure 6.6: Simultaneously measured empty-states (a: V_{bias}=0.15V) and filled-states (b: $V_{bias} = -0.15$V) STM micrographs of a $1T$-$TiSe_2$ single crystal grown at 650°C . Image size: 22.2 nm×11.4 nm, I_t=0.2nA, T=4.7K. Native defects are labelled A, B, C, D. c) Model representation of the inequivalent $^1/_4$ (filled symbols) and $^3/_4$ (empty symbols) lattice sites for defects A-D in the commensurate CDW phase. *Image adapted from [40].*

calculations [37, 188] suggest that the CDW could reside on the bonds and not in a specific atomic layer. In this last case, the only possible explanation of the perfect alignment between the Se layer and the CDW superlattice is a specific orbital sensitivity of the tip.

As a consequence of the CDW modulation, there are two inequivalent sites in the unit-cell for each defect, with three times more $^3/_4$ than $^1/_4$ sites (Fig.6.6c). A survey of Se, O and Ti defects in a large area map (50×50nm^2, 23'000 unit cells, 177 defects in total) yields approximately three times more $^3/_4$ than $^1/_4$ configurations for each of them. This uniform statistical distribution of all native defects among $^3/_4$ and $^1/_4$ sites implies they do not interact strongly with the CDW in this crystal, even though the amplitude of its resistive CDW transition is reduced by over 30% compared to a sample with optimal stoichiometry (6.1a and [33]). If they were interacting, we would expect dislocations to enable the CDW lattice to accommodate the random defect landscape. Indeed, we find no systematic domain formation, dislocations or weakening of the CDW lattice due to native defects. This rigidity of the CDW can be directly linked to its commensurate nature in $1T$-TiSe$_2$ [53]. In the same survey, we count about 80 intercalated Ti (defect D), corresponding to 0.35% self doping, in excellent agreement with literature for samples grown at 650°C [33].

Se vacancies appear as well resolved dark sites independent on bias voltage and position at the surface (Figs. 6.7a-c). In contrast, defects B-D are mostly bright and best resolved and differentiated at positive V_{bias} (Fig. 6.6). Their characteristic patterns revealed by STM [39] are slightly modified in the presence of the CDW and depend on their $^1/_4$ or $^3/_4$ configuration (Figs. 6.7 and 6.8). Of all defects, iodine substitution for Se$_{down}$ (defect B) is the most difficult to identify. On the $^1/_4$ site, it appears as a faint enhancement of the three nearest CDW maxima (Fig. 6.7e). The $^3/_4$ configuration appears as a few atoms long brighter chain extending along one of the crystallographic direction (Fig. 6.7d). Similar bright atomic chain features are found around defect A (Figs. 6.7a and (j)). DFT simulations of defects A and B are in good agreement with these experimental observations (Figs. 6.7c and f). The linear features are reproduced in the model without including the CDW instability. This shows they are not a different CDW ground state (e.g. 1D-CDW), but reflect local strain due to the Se vacancy and the larger atomic radius of iodine compared to Se. In regions with higher defect densities, these chains cooperate to form stripy patches in the STM topography, but without disrupting the long range coherent CDW (Fig. 6.7(j)). The defects in these regions will produce an anisotropic deformation landscape explaining why these stripes do not always appear in

all three high symmetry directions with the same intensity. When the defect density is low and in the vicinity of intercalated Ti (defect D), these stripes are usually less or not visible (Fig. 6.6a). Defects C and D

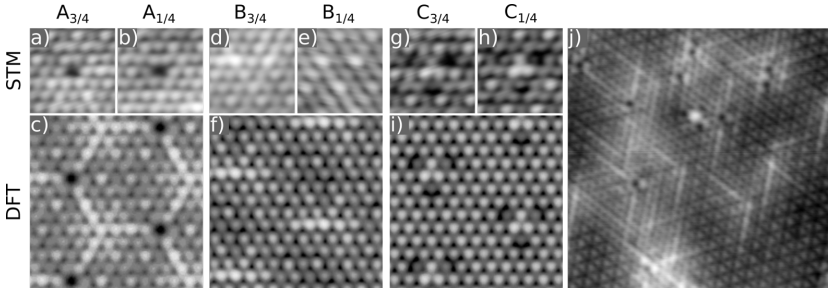

Figure 6.7: High resolution STM micrographs centered on Se vacancies (a,b), iodine (d,e) and oxygen (g,h) substitutions at $^3/_4$ sites (a,d,g) and $^1/_4$ sites (b,e,h) with corresponding DFT simulations calculated without including the CDW (c,f,i). (j) Linear features around defects A and B observed by STM on $1T$-$TiSe_2$ grown (11.5×11.5nm^2, $V_{bias} = +150$mV, I_t=0.2nA). All images are taken on crystals grown at 650°C except for image (j) recorded on a sample grown at 575°C to have a reduced number of intercalated Ti. *Image adapted from [40].*

show more complex triangular patterns without the linear atomic features found around defects A and B. Oxygen substitution for Se_{down} (defect C) is characterised by three bright central atoms centred on a larger, 60° rotated triangle of three dark atoms (Figs. 6.7g and h), in good agreement with DFT modelling (Fig. 6.7i). Titanium interstitials (defect D) appear as two concentric bright triangles centred on the defect (Fig. 6.8) [39], except for the $^1/_4$ configuration at $V_{bias} < 0$, which is not visible in experimental data (Fig.6.8a). The central triangles point in opposite directions in defect C compared to defect D, while the triangular outline of defects C and D always point in the same direction in a given experiment (Fig. 6.6), attesting the perfect crystalline structure of our $1T$-$TiSe_2$ specimen.

6.2.2 A new insight into the CDW phase

From this detailed analysis on defects in presence of CDW, we can extract some important information about the CDW. First of all, the unique triangle orientation of defect D and the perfect match between the data and the DFT models, which were all calculated in the $1T$-polytype structure, imply there are no $2H$-polytype inclusions where

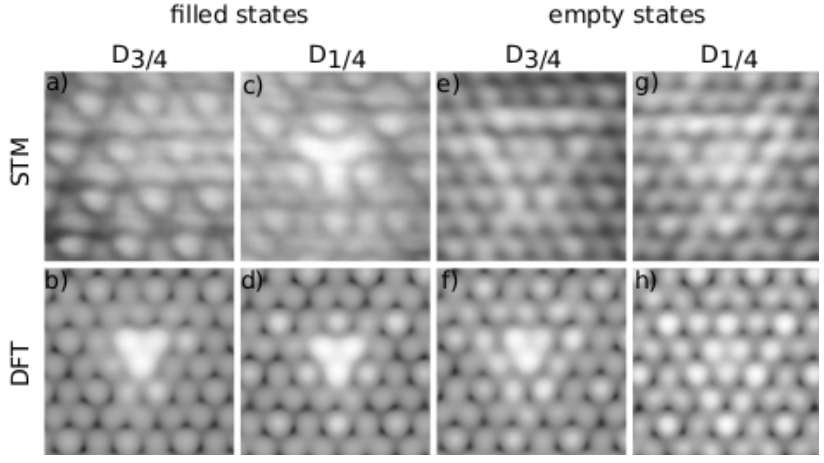

Figure 6.8: High resolution STM micrographs centered on intercalated Ti at $^3/_4$ sites (a,e) and $^1/_4$ sites (c,g) with corresponding DFT simulations in the presence of the CDW (b,d,f,h). $V_{bias} = -150$mV (a,b,c,d) and $V_{bias} = +150$mV (e,f,g,h), I_t=0.2nA. *Image adapted from [40].*

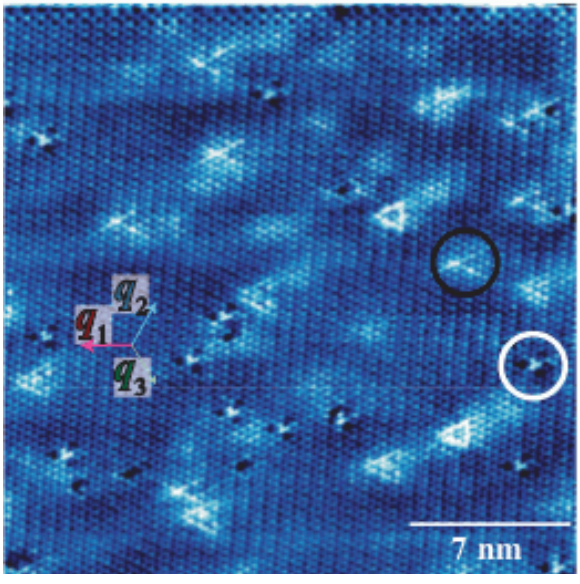

Figure 6.9: STM image at T=78K of chiral Friedel oscillation adapted from Ishioka *et al.* [41]. Black circle: “bright" chiral oscillation in the left-handed configuration associated with an intercalated Ti (defect B in our analysis); white circle: “dark" chiral oscillation in the right-handed configuration associated with a Ti vacancy (defect C in our analysis). Scanning parameters: V_{bias}=180mV, I_t=0.2nA.

the coordination of the Ti atom changes from octahedral ($1T$) to trigonal-prismatic ($2H$). A similar reasoning can be applied also to defects B and C, confirming the presence of a uniform polytype at the surface.

The appearance of all native defects, except surface Se vacancies (defect A), change slightly depending on their $^1/_4$ or $^3/_4$ configuration. At positive sample bias, the oxygen substitution (defect C) in the $^1/_4$ configuration totally obscures the amplitude of the three nearest CDW maxima (Fig. 6.7h) whereas iodine on the same location (defect B) enhances them slightly (Fig.6.7e). Intercalated titanium (defect D) has an unmistakable triangular signature, with very sharp vertices in the $^1/_4$ configuration that become nearly extinct in the $^3/_4$ configuration. These different appearances of native atomic defects depending on their configuration ($^1/_4$ or $^3/_4$) suggest another explanation for the recently reported chiral Friedel oscillations (Fig.6.9). Our data and DFT modelling show that the distinct left and right handed patterns discussed by Ishioka *et al.* [41] correspond in fact to different native defects (O and I-substitutions) in the two distinct $^1/_4$ and $^3/_4$ configurations, unrelated to chirality. Furthermore O and I-substitutions occupy the same position in the lattice and this is completely different from the situation of having an intercalated Ti and a Ti vacancy, as it was suggested. Thus the idea that an intercalated atom could induce a set of mirror planes and the consequent inversion of chirality is not working here. Finally we underline that, apart from the four defects described, we did not observe any other defect which could be attribute to a Ti vacancy.

The native defects are poorly resolved in the negative low bias STM micrographs discussed here, except for intercalated Ti (defect D) in the $^1/_4$ configuration and Se vacancies (defect A). The dark sites associated with Se vacancies (defect A) correspond to holes in the topography and are seen as such at both polarities. The other defect patterns are primarily electronic and their bias polarity dependent visibility observed here is consistent with a CDW gap that is biased towards occupied states at the Fermi level [149]. A striking exception to this behaviour is defect D which is nicely resolved in the $^1/_4$ configuration at $V_{bias} < 0$ (Figs. 6.6b and 6.8c), closely matching the DFT modelling. The donor nature of intercalated Ti contributing electron states just above the occupied edge of the CDW gap [39] can explain the finite contrast of defect D at negative bias inside the CDW gap. However, it is presently not clear why only the $^1/_4$ configuration is resolved at $V_{bias} = -150$mV (Fig.6.8c) while the $^3/_4$ configuration remains invisible (Fig. 6.8a). This question demands further investigations, in particular in the context of a proposed excitonic ground state [34, 189].

In general, the only change, besides the characteristic signatures

of each defect, is a locally enhanced brightness linked to their doping nature [39]. The theoretical proposal by McMillan [53] that atomic defects might trigger an incommensurate CDW is clearly not observed here. However we cannot exclude the possibility that a higher defect concentration could affect the CDW pattern.

6.3 Conclusion

Thanks to high resolution STM micrographs and DFT modelling, we have been able to identify, both in imaging and spectroscopy, four predominant defects in $1T$-$TiSe_2$: Se vacancies (defect A), Se substitution by residual iodine (defect B) and oxygen (defect C) atoms and intercalated Ti atoms (defect D) [39]. We found no trace of Ti vacancies as previously suggested [41]. Using this detailed surface characterisation, we have established that the lattice observed in STM micrographs belongs to the Se layer at all energies and that the CDW modulation seen by STM resides on this layer.

Furthermore, we have shown the great potential of high resolution STM imaging of the CDW in the presence of atomic defects to gain insight into this ordered phase. At least for a total defect concentration of $\sim$0.77% ($\sim$0.35% considering only Ti defects), we find that native defects have essentially no impact on the CDW lattice, while the corresponding phase transition is significantly reduced in transport measurements (Fig. 6.1) [33]. Comparison with DFT modelling further allows us to determine the precise position of intercalated Ti in the crystal structure and the specific crystal polytype, demonstrating that the observed defect patterns in the CDW phase are all consistent with the $1T$-polytype, excluding $2H$-polytype inclusions [190]. Finally, our study sheds a different light on recently published work on the chiral nature of Friedel oscillations in the vicinity of defects [41]. We find evidence that the left and right-hand patterns identified in that work are the signatures of different $1T$-$TiSe_2$ native defects located on inequivalent lattice sites with respect to the CDW modulation.

The identification of intrinsic defects in the pristine material has been the first fundamental step required in order to be able to study the specific properties of Cu intercalated $1T$-$TiSe_2$. Indeed, as we will see in the next chapter, this detailed “defects-catalogue" will help us in identifying the signature of Cu atoms and their peculiar effects on CDW. Furthermore, due to the stabilities of these defects at the surface, they can be used as a reference to select specific regions of the crystal during measurements.

Chapter 7

CDW phase in $1T$-Cu_xTiSe_2

CDW instabilities appear in many materials that undergo also a superconducting transition: a stripe charge order, possibly due to strain, has been observed in $2H$-$NbSe_2$ [191] and in intercalated graphite [17], CDW domains have been detected in $2H$-Mn_xNbSe_2 and $2H$-Co_xNbSe_2 [192], and different kinds of charge order have been discovered in High-Tc superconductors ([8–10] and chapter 2). In $1T$-$TiSe_2$, it is possible to move from the standard CDW to a superconducting ground state tuning pressure or Cu intercalation. In the literature there are already indications that the simple phase digram suggested by Morosan *et. al.*, with a CDW phase disappearing with the emergence of the superconducting dome, might be more complicated. Indeed, an incommensurate CDW have been observed in $1T$-$TiSe_2$ under pressure close to the superconducting dome, and Raman scattering measurements on $1T$-Cu_xTiSe_2 ($0.04 \leq x \leq 0.07$) suggest the coexistence of CDW fluctuations and superconductivity.

In this chapter we present a study of the CDW phase in $1T$-Cu_xTiSe_2 with a Cu concentration below the optimal value ($0 \leq x \leq 0.07$). The first achievement, which is fundamental for our following studies, is the identification of the topographic signature of Cu atoms along with their precise position in the crystal structure, obtained through the comparison of our STM micrographs with DFT calculations. This result allows us to determine the local level of doping and to study the effect of Cu on the CDW phase.

All STM measurements were taken with a cut PtIr tip in constant current mode. The defect nomenclature – A for selenium vacancies, B and C for iodine and oxygen substitution in the lower Se layer re-

spectively – is the same used in the previous chapter, except for excess Ti, which is labelled D_{Ti} to distinguish it from intercalated Cu (see Fig. 6.1b in chapter 6). Indeed, we will see that Cu atoms occupy the same octahedral site in the van der Waals (vdW) gap (position D) as excess Ti. This work has been a collaboration with the group of of Dr. D. R. Bowler from University College London, which provides us the DFT simulations.

7.1 Copper signature

High resolution STM micrographs of the cleaved surface of pristine $1T$-$TiSe_2$ recorded above and below T_{CDW} clearly reveal the commensurate $2a_0 \times 2b_0$ CDW phase transition (Fig. 7.1a,b). The doubling of the in-plane lattice parameters associated with the low temperature CDW superlattice is also obvious from the FFT of these images (Fig. 7.1c,d). The atomic lattice defects resolved in Fig. 7.1 have all been identified in a combined STM/DFT study ([39] and chapter 6) as Se vacancies in the surface layer (A), I and O-substitution for bulk Se (B and C) and Ti intercalated into the vdW gap (D_{Ti}). This DFT supported identification leads to the important conclusion that the CDW charge modulation resolved in the STM micrographs resides in perfect registry in the hexagonal Se surface layer [40].

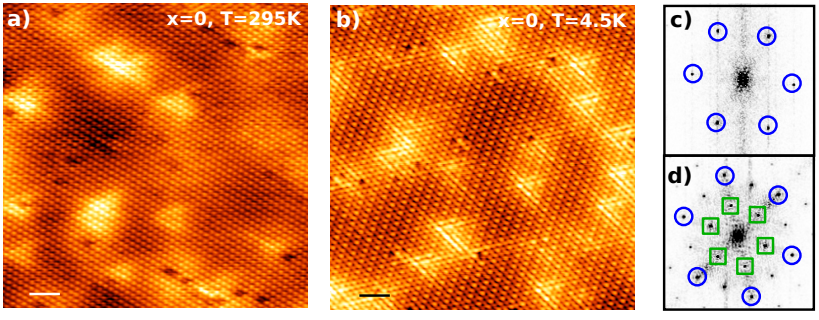

Figure 7.1: a) STM topography of pristine $1T$-$TiSe_2$ at 295 K. Scanning parameters: V_{bias}=100mV, I_t=100pA. b) STM topography of pristine $1T$-$TiSe_2$ at 4.5 K showing $2a_0 \times 2b_0$ reconstruction due to the CDW. The presence of defects does not influence the CDW periodicity. Scanning parameters: V_{bias}=150mV, I_t=100pA. c), d) Two dimensional Fourier transform of image a) and b) respectively. Circles highlight the reciprocal lattice spots while squares correspond to the reciprocal CDW superlattice spots. Scale bar in images a), b): 2 nm. *Image b): courtesy of Dr. Alessandro Scarfato.*

Intercalating copper into the vdW gap of $1T$-$TiSe_2$ triggers a significant modification of the low temperature STM micrographs. As it can be seen at 1.5K on a 7% copper intercalated crystal (Figs. 7.2,7.3), the image background shows inhomogeneous modulations and a new atomic defect besides those found in pristine specimen. Its triangular pattern (Fig. 7.2c) is a perfect match to the DFT prediction for a copper atom intercalated into the $1T$-$TiSe_2$ vdW gap right below a Ti lattice site (Fig. 7.2d). We did not identify any other atomic feature that could be related to Cu in a different lattice site. This assignment is further supported by the fact that we count about 200 such defects on a 18×18 nm^2 image (Fig. 7.3), in excellent agreement with the nominal 7% content of this crystal. According to our STM microscopy and DFT

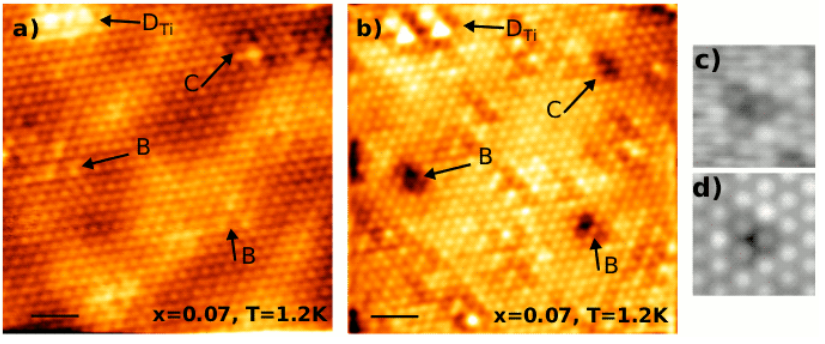

Figure 7.2: Surface characterisation of $1T$-$Cu_{0.07}TiSe_2$ at 1.2 K. a), b) STM topography. Scanning parameters: a) V_{bias}=150mV, I_t=30pA; b) $V_{bias} = -1.2$V, I_t=30pA respectively. Images a) and b) are taken on the same region at postive and negative bias. c) Zoom on Cu defects. Scanning parameters: $V_{bias} = -1.2$V, I_t=30pA d) DFT simulation of an intercalated Cu. Images a) and b) are FFT filtered to eliminate noise. Scale bar in images a) and b): 2 nm. (*DFT simulation courtesy of Dr. D.R. Bowler.*)

simulations, intercalated Cu and Ti atoms occupy the same octahedral site in the $1T$-$TiSe_2$ vdW gap (position D). These crystals are grown at 800°C and hence the concentration of excess Ti (defect D_{Ti}) should be 1% (meaning about 30 D_{Ti} defects in a 18×18 nm^2 area) [33]. The fact that this is not happening is another confirmation that Cu is occupying the sites taken by excess Ti in pristine crystals. Even if it is commonly accepted that in the $1T$-phase the intercalant atom is occupying the octahedral site in the vdW gap [139, 193, 194], this is the first time it is experimentally verified with atomic scale precision the Cu atom position in the crystalline structure.

Cu and Ti atoms have strikingly different microscopic signatures and

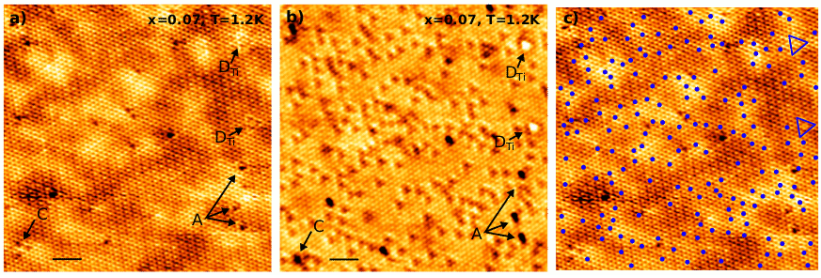

Figure 7.3: Surface characterisation of $1T$-$Cu_{0.07}TiSe_2$ at 1.2 K. a), b) STM topography. Scanning parameters: a) V_{bias}=150mV, I_t=30pA; b) $V_{bias} = -1.2$V, I_t=30pA respectively. Images a) and b) are taken on the same region at postive and negative bias. Scale bar in images a) and b): 2 nm. c) Intercalated Cu positions (dots) have been extrapolated from image b) and superimposed to image a) Triangles are Ti defects (D_{Ti}) used as a reference for the alignment of the two images.

effects on the physical properties of the host crystal. The signature of intercalated Ti in STM images is very sharp and localized and it has no effect on the CDW lattice seen by STM [40] up to several percent concentrations. In contrast, intercalated Cu exhibits a distinct STM signature only at a specific energy (-1.2V, Figs. 7.3b,c, 7.3b), while it is associated with an inhomogeneous background at low energies ($\pm$200mV)(Fig. 7.3a,c) .

7.2 CDW instabilities

Transport measurements did not reveal any CDW transition for crystals with a Cu concentration higher than 4%. From STM micrographs we see that intercalated copper has a strong impact on the CDW lattice, triggering dislocations and charge stripes even at very low concentrations.

At the lowest Cu concentration of 1% studied here, the CDW reveals a tendency to form charge stripes running along one of the CDW lattice vectors (Fig.7.4). The presence of well resolved single atom Se vacancies (A) in the same image excludes a tip artefact as the origin of this 1D feature. The absence of the standard CDW superlattice is verified by a FFT (Fig.7.4c) of this image. Increasing the Cu concentration up to 4.7%, stripes are less visible in topography due to the strong bright background coming from Cu (Fig.7.4b). However, a FFT of the topographic image confirms their presence (Fig.7.4d). Fig.7.5a) shows a

topography of a sample with 6.6% Cu. In this case no stripe is visible anymore, and at their place we usually see a bright background corresponding to high Cu concentration (Fig. 7.5). More precisely, although the standard $2a_0 \times 2b_0$ CDW superlattice is not clearly seen in the topographic image (Figs. 7.5a,d), it can remain as traces in the FFT (Figs. 7.5b,e) or it can form domains in the areas where the intercalated Cu atoms are absent/deficient (Figs. 7.5c,f). As expected, when CDW domains are large enough, like in Fig.7.5c, the FFT (Fig.7.5f) looks exactly the same as the one from a pristine sample (Fig.7.1d). The broad FFT spots observed Fig. 7.5e could be an indication of CDW fluctuations. These broad CDW spots in the FFT are visible only for images taken at negative bias ($V_{bias} = -100mV$). However, on the base of our data, we cannot exclude that they are present also at other energies. According to transport measurements, no CDW should be observed at all at this percentage of Cu (x=0.06) and at this temperature (T=78K), but local variations of the Cu concentration seem to be enough to induce CDW fluctuations or the complete reappearance of the CDW superlattice.

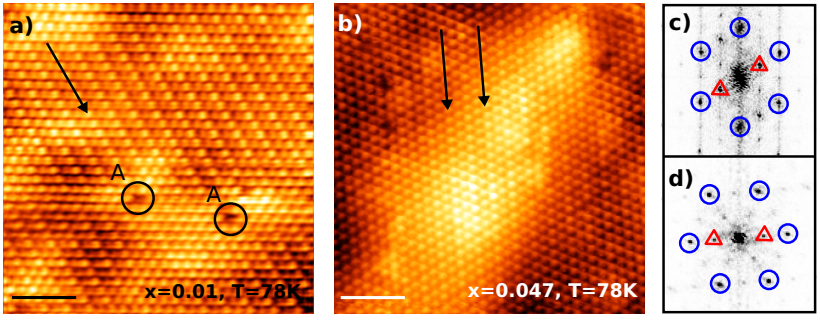

Figure 7.4: Stripe-region on the surface of Cu intercalated $1T$-$TiSe_2$ at 78 K. a) STM topography of $1T$-$Cu_{0.01}TiSe_2$. Scanning parameters V_{bias}=50mV, I_t=120pA. b) STM topography of $1T$-$Cu_{0.047}TiSe_2$. Scanning parameters V_{bias}=150mV, I_t=100pA. Scale bar in all images: 2 nm. Arrows indicate the stripe direction and circles indicate selenium vacancies. c),d) Two dimensional Fourier Transforms of images a), b). Circles correspond to the lattice, while triangles correspond to the stripe direction.

7.3 The role of disorder: CDW domains

As a result of the inhomogeneous Cu distribution at the local scale, CDW domains are present in all samples. In Fig.7.6 there are three typical examples at low (1% in Figs.7.6a and b) and high (7% in Fig.7.6c)

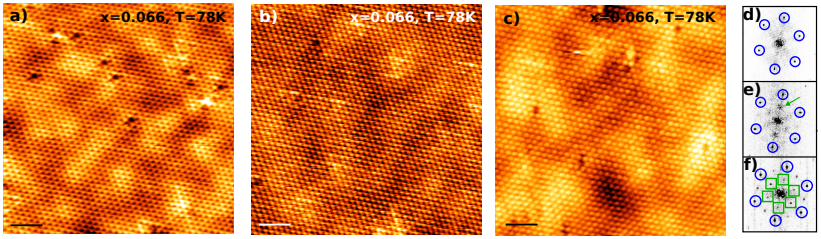

Figure 7.5: CDW patterns on $1T$-$Cu_{0.066}TiSe_2$ at 78K. a), STM topography of a region without CDW. Scanning parameters: V_{bias}=50mV, I_t=100pA. b), STM topography where CDW are not clearly seen. Scanning parameters: $V_{bias} = -100$mV, I_t=200pA. c), STM topographies where extended regions without CDWs are surrounded by residual CDW domains. Scanning parameters: V_{bias}=100mV, I_t=100pA. d), e), f) Fourier Transforms of images a), b), c) respectively. e) broad spots at the CDW wave vector positions are visible (arrow), even if CDWs are not visible in the real space image b). Circles highlight reciprocal lattice spots and squares to reciprocal CDW superlattice spots. Scale bar in all topographies: 2 nm.

Cu concentrations. Figs.7.6a and b show the coexistence of these domains with stripes in $Cu_{0.01}TiSe_2$ at 78K. Due to the low Cu concentration the standard CDW pattern is covering large portions of the sample and is usually not affected by the presence of stripes. Increasing the Cu concentration makes these CDW domains smaller and smaller (Figs. 7.3,7.5c,7.6c) and completely surrounded by regions rich in Cu. Upon increasing the Cu content, dislocations appear in the CDW lattice (blue/black dashed lines in Fig. 7.6c). In sample with low Cu concentration this shift in the CDW superlattice is rare but it can appear in case of a local higher amount of Cu (Fig. 7.6b).

A large concentration of Cu reduces or even suppresses the CDW, thus decoupling adjacent regions of $2a_0 \times 2b_0$ CDW domains. This effect due to impurities was predicted [53] and verified by STM [178, 192, 195, 196] in other dichalcogenides. However a commensurate CDW is considered more stable towards deformations [40, 54]. These local modifications of the CDW pattern could be due to the interaction of Cu with Se atoms, where the CDW modulation is located [39, 40]. Indeed, DFT simulations (our work and [140]) suggest a possible charge transfer from Cu to Se atoms with the formation of Cu-Se bonds. Furthermore Cu intercalation causes not only an expansion of the crystal structure in the c_0 direction, but also in the plane [38]. This behaviour seems consistent with a change in the electron-phonon coupling coefficient indicated by x-dependent Raman scattering [153].

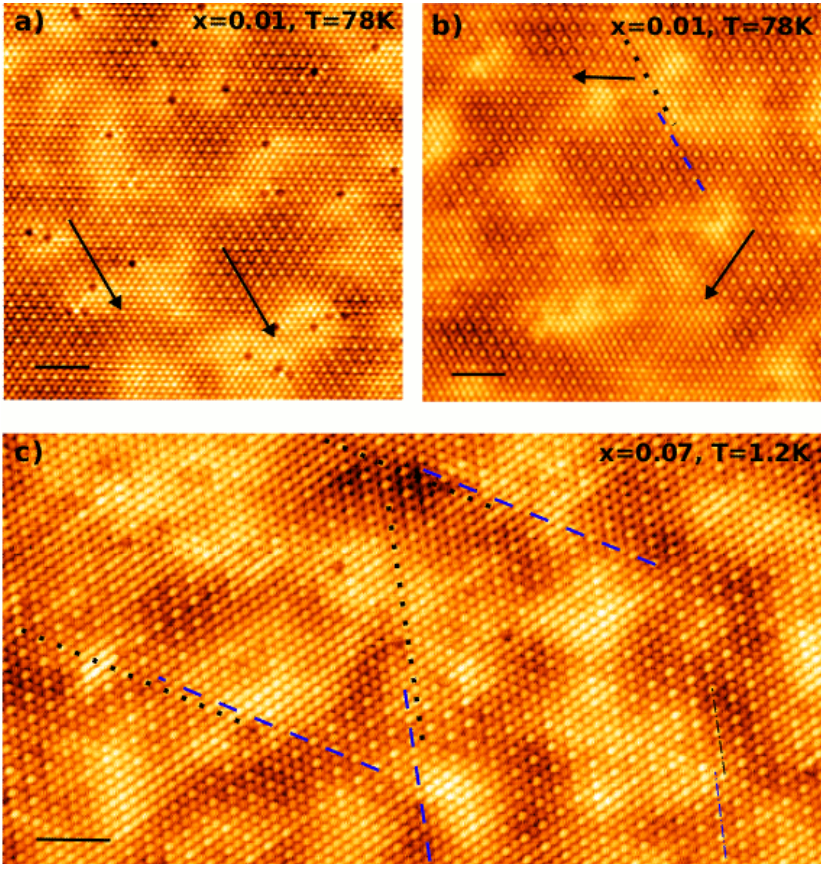

Figure 7.6: CDW domains on the surface of Cu intercalated $1T$-$TiSe_2$. a) STM topography of $1T$-$Cu_{0.01}TiSe_2$ at 78K . Scanning parameters V_{bias}=100mV, I_t=200pA. b) STM topography of $1T$-$Cu_{0.01}TiSe_2$ at 78K . Scanning parameters $V_{bias} = -50$mV, I_t=200pA. Black arrows indicate the stripe direction. c), STM topography of $1T$-$Cu_{0.07}TiSe_2$ at 1.2K. Scanning parameters V_{bias}=150mV, I_t=30pA. Dashed blue/black lines indicate the one atomic row shift between CDW domains. Going from one domain to the other a one-atomic-line shift of the CDW superlattice is observed. Scale bar in all images: 2 nm.

7.4 Scanning tunneling spectroscopy on 1T-Cu$_x$TiSe$_2$

Fig. 7.7 shows large range spectra ($\pm 1.3V$) taken on a 1T-Cu$_{0.07}$TiSe$_2$ crystal at 1.2K. While for Ti there is a specific peak around -200mV ([39] and chapter 6), no analogous peak is present for Cu intercalated samples. On this large scale STS spectra look quite similar to the one of pristine 1T-TiSe$_2$ [39], with a well-defined peak only in the unoccupied states centred at $\sim$+600mV. On the same surface, this peak is less pronounced in region lacking in Cu (Fig.7.7).

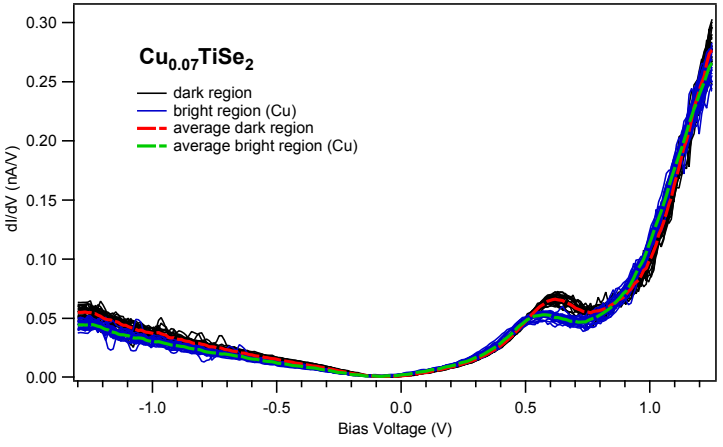

Figure 7.7: *dI/dV* curves obtained on 1T-Cu$_{0.07}$TiSe$_2$ on a region without Cu (dark region in topography) and a Cu-rich region (bright region in topography). The dashed lines are the average of 25 spectra, T=1.2K, V$_{set}$=1.3V, I_t=100pA. All spectra are obtained performing a numerical derivative of *I/V* curves.

Figs. 7.8c,d reports a 10$\times$10 nm^2 conductance maps taken on a 1T-Cu$_{0.066}$TiSe$_2$ crystal at 1.2K . Topographic images show the presence of 4 intercalated Ti defects, which are used as a reference (7.8a,b). Indeed the peak at ~ -200mV is always well visible in spectroscopy (7.8c). The distribution of Cu atoms is not uniform with brighter regions rich in Cu surrounded by darker regions (7.8b). No specific peak can be attributed to the presence of Cu atoms, however a general enhancement of the DOS around the Fermi level between $\sim +80$mV and ~ -150mV is observed in areas rich in Cu (7.8d). This is consistent with the bright background observed in topography and with the donor character of Cu atoms [38].

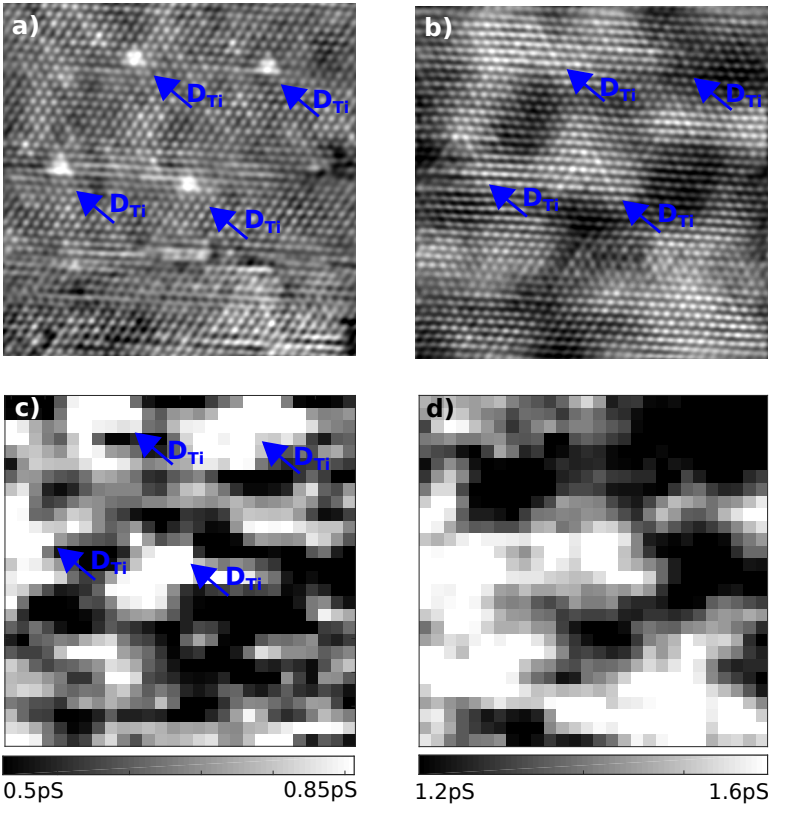

Figure 7.8: STM micrographs (a,b) and *dI/dV* maps (c,d) on $1T$-$Cu_{0.066}TiSe_2$ at 1.2K on a 10×10 nm^2 area. a) $V_{bias} = -1.1$V, I_t=30pA. b) V_{bias}=150mV, I_t=30pA. Blue arrows indicate excess Ti (D_{Ti}). c) *dI/dV* map at −255mV. at this energy Ti defects (D_{Ti}) are well visible. d) *dI/dV* map at −24mV. Two regions are clearly distinguishable, corresponding to the bright (rich in Cu) and dark (lacking in Cu) regions in topography. *dI/dV* curves are obtained with the lock-in technique: bias modulation 5mV at 918Hz, V_{set}=150mV, I_t=100pA.

A general depletion of the DOS below the Fermi energy, signature of the CDW-gap [104, 149] is still present, together with a small dip close to the Fermi energy. This dip has been already observed in previous STM measurements [149] and it has been attributed to the presence of disorder by point contact measurements [197].

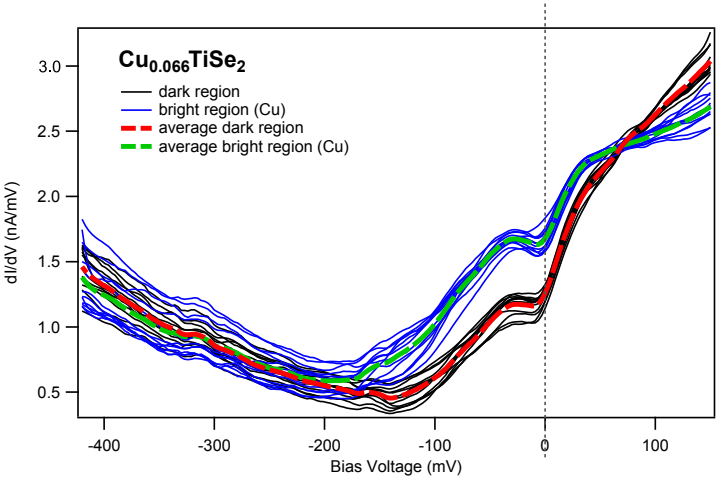

Figure 7.9: Experimental *dI/dV* curves obtained on $1T$-$Cu_{0.066}TiSe_2$ at 1.2K on a region lacking in Cu (dark region in topography) and rich in Cu (bright region in topography). Dashed lines are the average of 12 spectra obained with the lock-in technique: bias modulation 5mV at 918Hz, V_{set}=150mV, I_t=100pA.

7.5 Consequences for the phase diagram of $1T$-Cu_xTiSe_2

The picture, which is emerging from our measurements, is the one of a richer phase diagram (Fig. 7.10) compared to the phase diagram initially proposed by Morosan *et. al.* [38]. In the region between x=0.01 and x=0.05, we observe instabilities towards stripe formation in the CDW phase at 78K (purple dots in Fig. 7.10). We could not find any signature of stripes at 4K but more measurements are needed to exclude their presence. In the region between x=0.06 and x=0.07, we found traces of possible CDW fluctuations at 78K (blue dot in Fig. 7.10). In general, the transition region between the CDW and superconducting dome is strongly influenced by the random distribution of Cu atoms. Indeed CDW domains are observed everywhere, and they appear even

in crystals with a relatively high Cu concentration ($x > 0.06$) provided that the temperature is low enough (green dots in Fig. 7.10).

Indications for a more elaborated phase diagram compared to the first proposition [38] have been found already with other techniques, both in pristine $1T$-$TiSe_2$ under pressure and in Cu intercalated crystals. Indeed, CDW instabilities in the form of incommensurate CDW have been previously detected in pristine crystals of $1T$-$TiSe_2$ under pressure, above the superconducting dome and close to T_{CDW} [131]. The effects of pressure and Cu intercalation are known to be quite different [130]. In the first case it is possible to measure a shortening of the a_0 and c_0 lattice parameters, a positive hall coefficient, a shifting of the whole valence and conduction bands and an increase in their overlap, and a low critical field for superconductivity (200 Gauss at 3.5 GPa). In contrast, Cu intercalated $1T$-$TiSe_2$ is characterised by an increase in the a_0 and c_0 lattice parameters, a negative hall coefficient, a shift of the chemical potential within the fixed band and a higher critical field (1T for the optimal Cu concentration). However it is interesting to notice that in both cases superconductivity arises in proximity of instabilities in the CDW order.

A sign of CDW fluctuations is found for $x > 0.06$ at 78K, which might be consistent with what was observed in Raman scattering studies [153]. Barath *et al.* found hints for the existence of CDW fluctuations for Cu concentrations between 0.04 and 0.07 and a presence of a quantum critical point inside the superconducting dome for x=0.07. In this case it has been proposed that the phonon softening was associated with a substantial reduction in the electron-phonon coupling, possibly related with the expansion in the a-axis. This would be also consistent with our suggestion of a possible hybridisation between Cu and Se atoms, which can also influence the phonon spectrum.

The general behaviour of the phase diagram is in line with the one of other materials which exhibit charge order and superconductivity, such as $2H$-$NbSe_2$ [19, 191, 192], intercalated graphite [17], high-T_C superconductors [8–11, 14, 22, 78, 82, 93]. Understanding if there is a correlation between these two phases will be an important step to a better comprehension of the emergence of superconductivity in these materials.

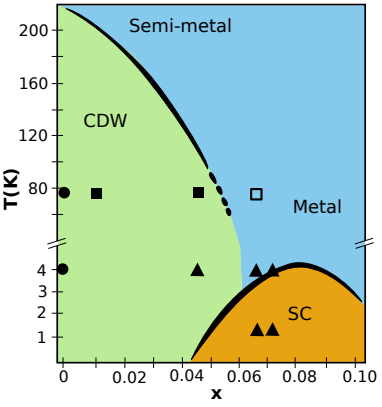

Figure 7.10: Phase-diagram for $1T$-Cu_xTiSe_2 adapted from Morosan *et al.* [38]. Markers corresponds to our measurements and we used the following code: circle = pristine $1T$-$TiSe_2$, filled square = stripes, empty square = fluctuations, triangle = CDW domains.

7.6 Conclusion

In this chapter we have shown the specific topographic signature of intercalated Cu atoms in $1T$-Cu_xTiSe_2, and we have revealed their precise position in the crystal structure, namely the octahedral sites in the van der Waals gap, which is the same location of Ti in excess. In contrast with excess Ti, we have found that the topographic signature of Cu atoms is well defined only at a specific bias ($V_{bias} = -1.2V$), while at other energies it is substituted by a general background increase. We did not associate Cu atoms with any specific spectroscopic signature except for a broad increase of the density of states close to the Fermi level, which is consistent with an increase of the electron population in the Ti conduction band observed by angle resolved photoemission spectroscopy.

We have looked at the CDW phase to study the effect of intercalated Cu atoms, and we have found that at a temperature of 78K and for Cu concentrations lower than 4%, a new one-dimensional CDW order develops (stripes). This suggests the existence of a possible intermediate CDW transition between the standard CDW and the disruption of the CDW phase, meaning a richer phase diagram compared to the one suggested by Morosan *et al.* [38]. Furthermore, we studied the role of disorder induced by a random distribution of Cu atoms and we found

that a local absence of Cu can cause the re-emergence of a CDW superlattice in samples with a relatively high Cu concentartion ($x>0.04$) provided that the temperature is sufficiently low.

Chapter 8

Superconductivity in 1T-Cu_xTiSe_2

The interplay between CDW and superconductivity and whether they are competing, cooperating or simply coexisting is still a matter of debate ([2–5] and chapter 2). Within this context, we decided to study Cu_xTiSe_2 crystals. CDW domains are always present in this compound at least for crystals with a Cu concentration lower than 8%, and thus it is possible to directly study the relation between CDW and superconductivity at the local scale. At the same time, a detailed analysis of the local changes of the superconducting gap is necessary to establish if the Cu_xTiSe_2 superconducting phase is influenced by inhomogeneities in the Cu distribution or by the presence of defects. In this chapter we report a preliminary STM/STS study of the superconducting gap Δ performed on slightly underdoped crystals ($Cu_{0.066}TiSe_2$, $Cu_{0.07}TiSe_2$) at 1.2K.

8.1 Superconducting transition

In Fig.8.1 we show the magnetic susceptibility of a $Cu_{0.066}TiSe_2$ crystal measured as function of temperature with a SQUID-VSM [Quantum Design]. The maximum superconducting transition temperature T_C is $\sim$ 2.6 K. The broad transition is due to the layered structure of this kind of crystals. The same measurement on a crystal of $Cu_{0.07}TiSe_2$ gives T_C $\sim$3K.

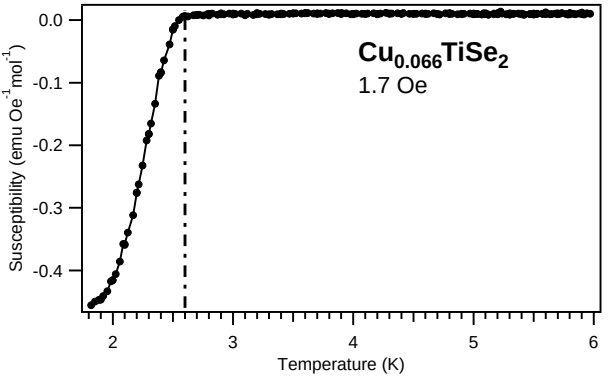

Figure 8.1: Magnetic susceptibility measured in a constant 1.7 Oe applied field on a crystal of $1T$-$Cu_{0.066}TiSe_2$.

8.2 Measuring the superconducting gap

Each *dI/dV* curve has been measured using the standard lock-in technique (see chapter 5). The acquired spectra have been smoothed with a Savitzky-Golay filter and fitted using a standard BCS model for a single s-wave gap taking into account inelastic scattering. According to this model we can write the DOS as:

$$D_S(E,\Gamma) = Re\left(\frac{E-i\Gamma}{[(E-i\Gamma)^2-\Delta^2]^{1/2}}\right), \tag{8.1}$$

where Γ is a parameter, which describes the lifetime effects of the quasiparticles at the gap edge [198]. This DOS has been convoluted with minus the derivative of the Fermi function to obtain the final fit equation for our *dI/dV* spectra (see chapter 4, derivative of Eq. 4.19). The temperature broadening, taken into account by the Fermi function, is of the order of $3k_BT$ ($\sim$0.3meV at T=1.2K) and thus it is of particular relevance in our case since it is comparable with the gap size.

8.2.1 The superconducting gap and the role of disorder

A *dI/dV* map (10$\times$10 nm^2, 28x28 spectra) has been measured on a $1T$-$Cu_{0.066}TiSe_2$ single crystal at 1.2K (lock-in parameters: bias modulation 80μV at 918Hz, V_{set}=3.5mV, I_s=60pA). A topography of the mapped area is reported in Fig.8.4a and it corresponds to the region measured in Fig. 7.8 as it is confirmed by the presence of the 4 intercalated Ti

defects (D_{Ti}). Two main regions can be distinguished: an upper region characterised by the presence of D_{Ti} defects and a less homogeneous Cu distribution, and a lower-right region with a uniform Cu distribution. The superconducting gap map is reported in Fig. 8.2b. Even if at the available resolution it is difficult to determine the presence of variations of the gap Δ, it is possible to recognise the two different areas individuated in topography and to associate lower values of Δ to the upper area characterised by higher disorder (Fig. 8.2c) . The corresponding histogram representing the distribution of the gap values is reported in 8.2d (same colour scale). To fit this distribution we performed a fitting with a bimodal gaussian distribution. The fit suggests the existence of two distinct peaks centred at Δ=0.31 meV (standard deviation σ of 0.02 meV) and at Δ=0.33 meV (standard deviation σ of 0.01 meV). Due to the small difference (3% percentage difference) and the relevance of the thermal broadening, a higher statistics is necessary to verify if it is correct to speak about two gaps or if there is a continuous distribution of gap values induced by disorder. The corresponding map and distribution for the parameter Γ are reported in Figs.8.3a,b. The distribution for the parameter Γ has an average value of 0.10meV with a standard deviation σ of 0.01meV.

In Fig. 8.4 we plot the normalised average (black line) of the 784 *dI/dV* spectra from the dI/dV map. The blue curve is the BCS fit (single s-wave gap, temperature used for the fit T=1.5K) of the average spectrum, which gives a value of 0.32 meV for the superconducting gap Δ. The good match between data and fit confirms, at least at the available resolution, that the gap is a single BCS gap with an s-wave symmetry as previously reported [141, 150, 152].Using this average Δ value, we have estimated the BCS ratio. Since we are measuring at a temperature which is $\sim$50% of T_C, considering a standard BCS temperature dependence for the gap, $\Delta(T=0)$ will be at most 10% larger. Using a $\Delta(T=0)$ value of 0.36 meV we calculate a BCS ratio $2\Delta/k_BT_C$ $\sim$3.2. This BCS ratio is compatible with heat capacity measurements [150] and only 10% off the standard BCS value of 3.5.

8.2.2 CDW and superconductivity

Fig. 8.5a shows a 10$\times$10 nm^2 STM micrograph of a $Cu_{0.07}TiSe_2$ crystal. On this area we distinguish regions rich in Cu, characterised by a bright background, and CDW domains corresponding to areas without Cu. We performed several STS measurements and then we divided the spectra in two groups according to the presence (red dots) or absence of Cu (blue dots) at the spectroscopy location. All spectroscopy

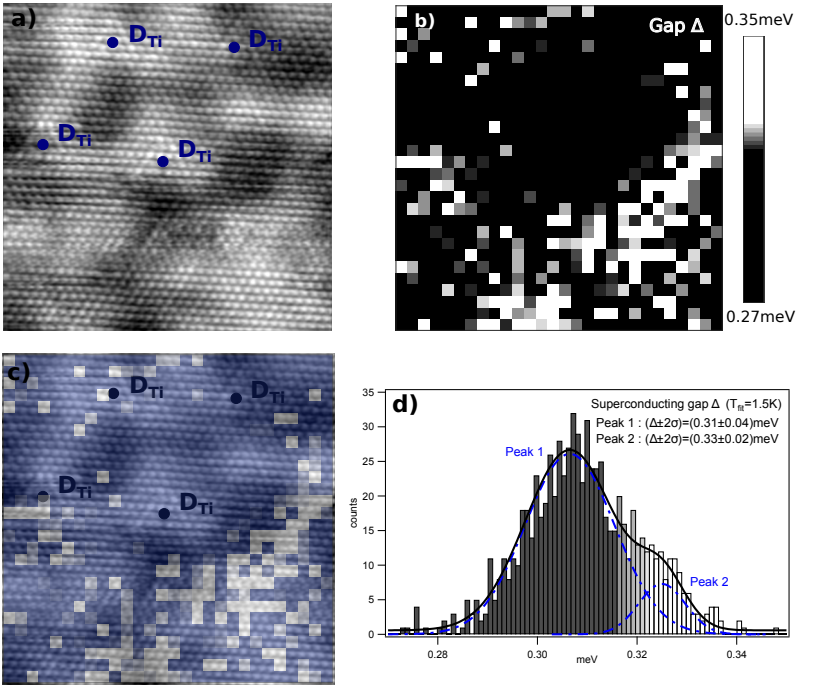

Figure 8.2: a) STM micrograph of a $1T$-$Cu_{0.066}TiSe_2$ crystal: 10×10 nm^2 area corresponding to the dI/dV map region. V_{bias}=150mV, I=30pA. Blue dots: intercalated Ti defects (D_{Ti}). b) 10×10 nm^2 Gap map. c) Superposition between the gap map in a) and the topography in Fig. 8.4a. d) Histogram of the superconducting gap Δ value fitted with a bimodal distribution (black line) made of two gaussian functions (dashed lines). The bin-colour scale corresponds to the one used in the gap maps.

measurements have been obtained using a lock-in technique with the following parameters: bias modulation 160μV at 918Hz, V_{set}=3mV, I_s=100pA. The resulting two average spectra are reported in Fig. 8.5b with the corresponding fit. No clear difference between the two group emerged, however we cannot exclude completely the existence of local variations, because the spectra corresponding to regions lacking in Cu are not taken at the centre of the domain but in proximity of the Cu rich region. The superconducting gap Δ is $\sim$0.22 meV, a value $\sim$30% smaller than the one obtained for $Cu_{0.066}TiSe_2$ crystals. This could be considered an unexpected result since T_C is $\sim$13% higher in $Cu_{0.07}TiSe_2$ crystals, but it is easily explained noticing that the local

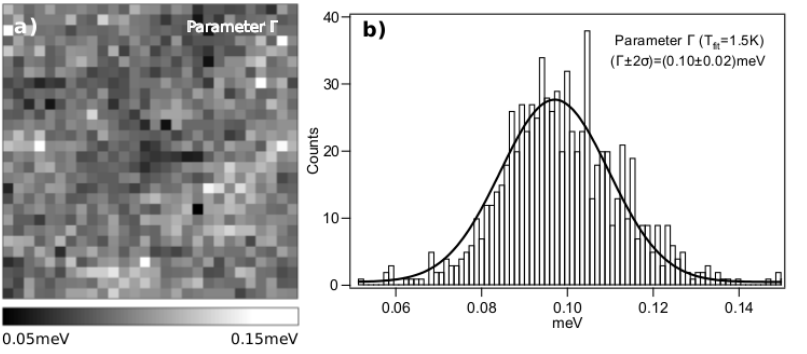

Figure 8.3: a)10 $\times$10 nm^2 map of the Γ parameter. b) Histogram of the distribution of the parameter Γ. The distribution is fitted with a Gaussian function.

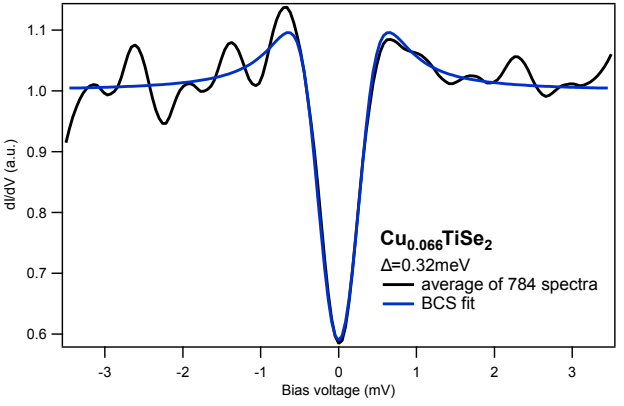

Figure 8.4: Normalized average of 784 *dI/dV* spectra and a BCS fit. Each *dI/dV* curve has been measured using the standard lock-in technique (bias modulation 80μV at 918Hz, V$_{set}$=3.5mV, I$_s$=60pA) and smoothed with a Savitzky-Golay filter before performing the average.

amount of Cu is quite low allowing the presence of CDW domains. Even if these are just preliminary data, the fact that the presence of CDW domains does not destroy completely the superconducting gap is already an important piece of information suggesting that CDW and superconductivity can coexist. This result might be in line with the idea that the CDW disappearing and the emergence of superconductivity are just a coincidence [105, 142]. Alternatively, the strong CDW

fluctuations associated with a quantum critical point inside the superconducting dome, as suggested by Raman measurements [153], could be the trigger of the superconducting phase.

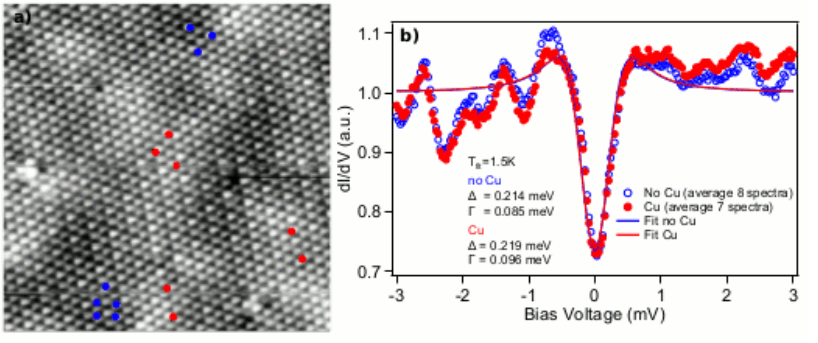

Figure 8.5: a) 10×10 nm^2 STM micrograph of a $1T$-$Cu_{0.07}TiSe_2$ crystal. Markers represent the spectroscopy locations from regions lacking or rich in Cu. V_{bias}=100 meV, I_t=60pA b) Fit of the average spectra coming from the two different regions. Each *dI/dV* curve has been measured using the standard lock-in technique (bias modulation 160μV at 918Hz, V_{set}=3mV, I_s=60pA) and smoothed with a Savitzky-Golay filter.

8.3 Conclusion

In this chapter we reported a preliminary STM/STS study on the role of disorder on the the superconducting gap and on the interplay between CDW domains and superconductivity. On the crystal studied (Cu concentartion 6.6% and 7%) and at the available resolution, we found that the gap is a single BCS gap with an s-wave symmetry confirming results found in literature [141, 150, 152]. We found that disorder seems to have an influence on the gap size, possibly determining the presence of two distinct gaps. We have shown that the presence of CDW domains does not destroy superconductivity suggesting a coexistence of the two phases. However, on the area considered, the gap is $\sim$30% lower than expected from the value of T_C, and this is possibly due to a locally lower Cu concentration, which allows also the presence of the CDW domains. At the available resolution and statistics, we did not identify any local variation of this gap that could be related to the presence of CDW.

From spectroscopy measurements on $1T$-$Cu_{0.066}TiSe_2$ we estimated an average value for the superconducting gap of $\sim$0.36meV at T=0 and thus a BCS ratio of $\sim$ 3.2, a value compatible with a standard BCS

superconductor and with the literature [141, 150]. The next step will be a detailed *dI/dV* mapping of the surface at higher spatial resolution to investigate the inhomogeneities of the superconducting gap and a study of this superconducting gap as function of intercalated Cu.

Chapter 9

Conclusions and Outlooks

We performed a complete surface characterisation of pristine $1T$-$TiSe_2$ and intercalated $1T$-Cu_xTiSe_2 by scanning tunneling microscopy and spectroscopy (STM/STS). The perfect match between our data and density functional theory (DFT) calculations has allowed us to identify the topographic and spectroscopic signatures of 4 different kinds of intrinsic defects in the pristine crystal: selenium vacancy, iodine or oxygen substitution of a selenium atom in the second selenium layer and intercalated titanium. We did not find any signature of Ti vacancies as previously suggested [41]. We analysed the CDW phase in presence of these defects and we have shown that the CDW superlattice is not distorted or pinned by any of these defects, while the amplitude of the peak in resistivity measurements, signature of the CDW transition, is reduced by over 30% at the studied Ti-self doping concentration of 0.35% (total amount of defects: 0.77%). Furthermore we gave a strong experimental proof that the CDW modulation, as seen by STM, is in perfect registry with the upper selenium lattice using the identification of defects in this layer as a reference. We did not find any $2H$-polytype inclusion as reported in room temperature measurements [190]. Although this finding cannot exclude an indirect Jahn-Teller mechanism [36, 127] as a possible origin for the CDW transition, the capability to locally identify the $1T$-phase may become a powerful tool in clarifying the role of local lattice modifications in the CDW formation. In addition we gave a different explanation of the defects attributed to chiral-Friedel-oscillations [41]. Indeed the right and left patterns previously identified [41] are actually signatures of two distinct native defects residing in inequivalent lattice sites with respect to the CDW modulation. The

only discrepancy between data and simulations occurred for intercalated Ti at negative bias (−150mV) in the $^3/_4$ configuration. Indeed, this configuration is invisible in STM topography. Further STS studies are necessary to understand this different behaviour between the titanium $^3/_4$ and $^1/_4$.

Starting from this detailed characterisation, we have identified the exact position of intercalated Cu atoms in the crystal structure, namely the octahedral sites in the van der Waals gap, the same as excess Ti. In contrast to excess Ti, we found that the topographic signature of Cu atoms is well defined only at a specific bias ($V_{bias} = -1.2V$), while at other energies we observed only an extended bright background centred on the Cu atoms. No specific spectroscopic signature can be attributed to Cu atoms except for a general increase of the density of states close to the Fermi level, which is consistent with an increase of the electron population in the Ti conduction band observed by angle resolved photoemission spectroscopy. Understanding the differences between excess Ti and intercalated Cu might be important in order to understand why superconductivity is absent in the pristine phase at ambient pressure and to shed some light on the mechanism at the origin of the CDW transition.

Knowing the signature of Cu atoms has been crucial to determine the local doping and the effect of intercalated Cu and disorder on the CDW. Indeed, we discovered the presence of CDW stripe instabilities in the underdoped region $0.01 \leq x \leq 0.05$ of the phase diagram, at least at 78K clearly related to the presence of Cu. Moreover, we found that, due to the not uniform distribution of intercalated Cu atoms, it is always possible to distinguish CDW domains even for relatively high Cu concentrations ($x \sim$0.07) if the temperature is low enough.

Finally we performed preliminary measurements in the superconducting phase of Cu_xTiSe_2 crystals investigating the role of disorder and of CDW domains. We found that on the crystals studied (x=0.066 and x=0.07) and at the available resolution, the superconducting gap is consistent with a single BCS gap with an s-wave symmetry. We showed that disorder and the local amount of Cu have an influence on the gap size and might even induced the appearance of two (or more) distinct gap values. Furthermore we found that the superconducting gap is not destroyed by the presence of CDW domains suggesting a coexistence of the two phases. According to our preliminary measurements, there is no difference in the gap size inside and outside domains. Even if we cannot exclude completely the presence of gap variations due to CDW domains, we showed that this difference is probably quite small. From an STS map performed on a $1T$-$Cu_{0.066}TiSe_2$ crystal, we extracted an

average value for the superconducting gap Δ of $\sim$0.36meV at T=0 corresponding to a BCS ratio of $\sim$ 3.2, a value compatible with a standard BCS superconductor and the value reported in literature [141, 150].

Our findings indicate that the phase diagram of $1T$-Cu_xTiSe_2 is richer than first predicted by Morosan *et al.*, suggesting possible similarities with the phase diagram of cuprates. However a lot of work has still to be done. We should study the stripe phase more in detail, especially as a function of temperature. Indeed, it would be interesting to see if there is a transition temperature, below which the crystal enters again in a standard CDW phase. We should also look more carefully in the boundary region of the phase diagram between CDW and superconductivity looking for possible CDW fluctuations. Lastly, a detailed spectroscopic study at low temperature and as function of Cu concentration is necessary to investigate the variations in the gap size due to disorder and to understand the relation between CDW and superconductivity.

In this work we present the potentialities of combined STM/STS/DFT studies in the characterisation of defects and dopants and in extracting information about the crystal structure. Furthermore we showed how these defects can help us in having an insight into other properties of the material like the CDW phase. In addition we also reveal new interesting aspects of the phase diagram of $1T$-Cu_xTiSe_2, which should be analysed more in details to better comprehend the relation between the CDW and superconducting ground states. There are still many open questions regarding this material and we hope to have shown the potentiality of $1T$-$TiSe_2$ and $1T$-Cu_xTiSe_2 as a playground for a better comprehension of the physics of quasi-2D crystals, with a particular focus on CDW and superconductivity.

Appendix A

Some properties of superconductors

The first signature of superconductivity, found by Onnes in 1911 [199], was the disappearance of electrical resistance in several metals below a critical temperature T_C. This discovery was followed by the measurement of perfect diamagnetism: a magnetic field not only cannot enter a superconductor but is also expelled as soon as the temperature is lower than T_C (*Meissner effect* [200]). Superconductivity can thus be destroyed by a *critical magnetic field* H_C with a temperature dependence that can be approximated by a parabolic law [45]:

$$H_C(T) \approx H_C(0) \left[1 - \left(\frac{T}{T_C}\right)^2\right]. \tag{A.1}$$

These two main properties were first described theoretically by the brothers F. and H. London in 1935 [45, 201], who wrote two equations for the microscopic electric and magnetic fields:

$$\boldsymbol{E} = \frac{\partial}{\partial t}\left(\Lambda \boldsymbol{J}_s\right) \tag{A.2a}$$

$$\boldsymbol{h} = -c\nabla \times \left(\Lambda \boldsymbol{J}_s\right) \tag{A.2b}$$

where the phenomenological parameter Λ is defined as:

$$\Lambda = \frac{4\pi\lambda^2}{c^2} = \frac{m}{n_s e^2} \tag{A.3}$$

with n_s the number density of superconducting electrons and λ the *penetration depth*. n_s is expected to vary continuously from 0 at T_C to

a limiting value of the order of the density of conduction electrons n at $T \ll T_C$. Eq. A.2a describes perfect conductivity, while combining Eq. A.2b with the Maxwell equation $\nabla \times \boldsymbol{h} = 4\pi \boldsymbol{J}/c$, they obtained an expression for the Meissner effect:

$$\nabla^2 \boldsymbol{h} = \frac{\boldsymbol{h}}{\lambda^2}, \tag{A.4}$$

where the penetration depth λ describes the penetration distance of a magnetic field inside a superconductor and has a temperature dependence approximately described by:

$$\lambda(T) \approx \lambda(0) \frac{1}{\sqrt{\left[1 - \left(\frac{T}{T_C}\right)^4\right]}}. \tag{A.5}$$

In 1950 Ginzburg and Landau [202] developed a phenomenological theory of superconductivity where the superconducting electrons are described by a complex pseudo-wavefunction ψ. In this framework the local density of superconducting electrons n_s is simply given by $|\psi|^2$. Using a variational principle and expanding the free energy in powers of ψ and $\nabla\psi$, they were able to derive a differential equation for ψ:

$$\frac{1}{2m^*}\left(\frac{\hbar}{i}\nabla - \frac{e^*}{c}A\right)^2 \psi + \beta|\psi|^2\psi = -\alpha(T)\psi \tag{A.6}$$

where α and β are the expansion coefficients in the series expansion of the free energy, and e^* and m^* are the particle charge and mass respectively. One of the main success of this theory was in describing the intermediate state of superconductors, where superconducting and normal domains coexist in the presence of $H \approx H_C$. An important physical parameter in this theory is the so called *Ginzburg-Landau coherence length*:

$$\xi(T) = \frac{\hbar}{\sqrt{|2m^*\alpha(T)|}} \tag{A.7}$$

which represents the distance from the surface necessary for the order parameter $\psi(\boldsymbol{r})$ to reach its bulk value. To highlight the fact that $\xi(T)$ diverges at T_C, we can rewrite the coherence length as:

$$\xi(T) = \xi(0)\sqrt{\left|\frac{T_C}{T - T_C}\right|} \tag{A.8}$$

where $\xi(0)$ is basically the *Pippard coherence length* (apart for a numerical factor of the order of unity). Pippard [203] pointed out that only

electrons within $\sim k_B T_C$ of the Fermi energy can have a role in a phenomenon which develops at T_C. The momentum of these electrons will vary in the range $\Delta p \approx k_B T_C / v_F$ with v_F the Fermi velocity. Therefore, the uncertainty principle will give:

$$\Delta x \gtrsim \hbar / \Delta p \approx \hbar v_F / k_B T_C \tag{A.9}$$

from which it follows the definition of the Pippard coherence length:

$$\xi_0 = a \frac{\hbar v_F}{k_B T_C} \tag{A.10}$$

where a is a numerical constant of the order of unity. In the presence of scattering we can rewrite this coherence length as:

$$\frac{1}{\xi(\ell)} = \frac{1}{\xi_0} + \frac{1}{\ell} \tag{A.11}$$

where ℓ is the mean free path. From this definition we can describe two limits related to the amount of impurities in the superconductor:

$$\textit{dirty limit}: \quad \xi(\ell) = \ell \quad \text{if} \quad \ell \ll \xi_0 \tag{A.12a}$$

$$\textit{clean limit}: \quad \xi(\ell) = \xi_0 \quad \text{if} \quad \ell \gg \xi_0. \tag{A.12b}$$

The ratio of the Ginzburg Landau penetration depth λ and the coherence length ξ is giving the so called *Ginzburg Landau parameter*:

$$\kappa = \frac{\lambda(T)}{\xi(T)}. \tag{A.13}$$

Both lengths diverge like $(T_C - T)^{-1/2}$ near T_C, therefore this ratio is independent of temperature. For superconductors with $\kappa > \frac{1}{\sqrt{2}}$ a different flux penetration behaviour has been observed [204]. These superconductors are called of *type II* in contrast to standard superconductors which are of *type I*. They are characterised by two critical fields, H_{C1} and H_{C2}. From the lower critical field H_{C1} there is a continuous increase of the flux penetration which arrives at the maximum value at the upper critical field H_{C2}. In the *mixed state* between these two critical fields, the flux penetrates in a regular array of flux cylinders, each carrying a quantum of flux. Around these cylinders there is a vortex of supercurrent with radius $\sim \xi(0)$. These vortices can be mobile, for example due to thermal fluctuations. As a consequence the resistivity of the superconductor can be different from zero. To avoid this energy dissipation coming from a movable vortex lattice, *pinning centres* are

needed, which correspond to impurities or crystal defects. The existence of vortices was confirmed experimentally by magnetic decoration measurements [205] and STM [164].

An important step forward in the understanding of superconductivity was done with the experimental determination of the existence of a gap through specific heat measurements [206,207]. According to these measurements, for $T < T_C$ the electronic specific heat (C_{es}) show an exponential T dependence:

$$C_{es} \approx \gamma T_c a e^{-b\frac{T_C}{T}}, \tag{A.14}$$

while the normal-state electronic heat (C_{en}) has a linear T dependence: $C_{en} = \gamma T$. a and b are numerical constants.

Acknowledgements

First of all I would like to thank Prof. Christoph Renner for giving me the possibility to do my PhD work in his group, for introducing me to the nano-world and for always pushing me to give my best. His passion for science, patience and contagious enthusiasm have been a great example to me. I would also like to thank Daniel and Sigrun, who helped me in moving my first steps in the lab and taught me the basics of STM, and especially Alessandro for his precious help in making the new STM working: his great technical expertise has been fundamental to get some of the results presented here.

This thesis work has been part of a collaboration with other three groups from three different institutions. First of all I would like to thank Alberto Ubaldini from University of Geneva/Salerno who believed in this "dichalcogenides-project" since the beginning, taking the challenge to grow the crystals for us. In particular, I would like to thank him for all the time he spent with me in answering all my infinite questions about the crystals growth and characterisation. Thanks also to Céline Barreteau who took over Alberto's work. She has been always available to answer all the remaining questions, to help me with the last minute characterisation measurements and to correct the "growth-subchapter". Secondly I would like to thank the group of Prof. Philipp Aebi at the University of Fribourg, who worked with us for the STM characterisation of the pristine sample. In particular I would like to thank Baptiste Hildebrand for all the discussions and the exchange of ideas. It has been a real pleasure working with him! Last but not least I would like to thank Prof. David Bowler from UCL, not only for his precious DFT calculations but also for being always available in answering my second list of infinite questions.

I would also like to thank Christophe Berthod and Ivan Maggio-Aprile who helped me a lot in writing this manuscript. They have been always available for discussions and full of useful comments and suggestions... I have learnt a lot from them!

A special thank is for Greg, who is not only a great technician but also a good friend, and thanks to Greg and Alex for all the "morning-coffees" we had together which helped me in starting the day always in a good mood even when nothing was working in the lab. A huge hug is for François, Renan, Arpad, Marcello, and Léo who shared with me the everyday PhD life and many lunches,coffees (I hope you enjoyed the biscuits!) and apéros. I could not make it without their support!

I would also like to thank all the members of the Photomedicine Lab at EPFL. Especially I would like to thank Prof. Hubert van den Bergh who has always been there to listen to my doubts, to answer my questions and to give me his feedback. I will never forget his infinite curiosity about nature and science. And thanks to Filippo, Blaise, Cédric, Senthil and Carla with whom I shared my first "Swiss-experience": I really enjoyed all the time I spent with them.

During these years I have met a lot of wonderful people. Above all, there are 4 girls who became my best-friends here in Geneva: Daniela, Stéphanie, Sandra and Wei (+Brian!). Thanks for all the unforgettable time we spent together, I will never forget them. Thanks also to Yuliya and Elisabeth, who has always been there for a chat, and to the "theory-office" (Emanuele, Laura and Noam) for their great support during the last months of my thesis work (and for the coffees and chocolate); to Virag and Dara for all the nice lunches and breaks and for sharing with me their different PhD experience; to Xavi and Timo who has always been able to make me laugh even in the darkest moment of my PhD path; to Yves, Chantal and Samuel for all the great dinner times I had with them: when will be the next pizza? I would like also to thank my Volleyball team – Genève-Ville – for the patience they showed each time I was late for the training because I was stuck in the lab. Thanks to the guys of the "Missione Cattolica Italiana di Ginevra" and in particular to Jessica, Luca, Chiara, Caterina, Cecilia&Riccardo, Letizia and Max. A special thanks is for Suor Cleo who has been always ready to listen to me every time I was suddenly bumping into her at University. Thanks to my old Lausanne-friends who has always been there even when I moved to Geneva (and when they moved away from Switzerland): Xiaoqing, Tina, Shan, Samantha, Jens, Mahshid&Arash, Maria, Stefano and Mariateresa. And of course thanks to my friends in my hometown who have never forgotten me even if I have been far away so long: Simo, Fra, Manu, Paolo, Rong, Alessio, Anna, Massi and Mariarita.

The final and greatest thanks are going to Dario and my family. Grazie Dario per l'infinita pazienza e per aver sempre creduto in me...Non ci sono parole per descrivere il grande sostegno che mi hai dato in questi lunghi mesi di fine dottorato: grazie mille!! E grazie alla mia famiglia

per aver sempre assecondato la mia passione per la scienza e per avermi spinta ad andare sempre oltre i miei limiti.

Thank you all!!!

This work has been financed by the Swiss National Science Foundation.

Bibliography

1. D. Baeriswyl and L. Degiorgi, *Strong Interactions in Low Dimensions*. (Springer Netherlands 2007).
2. A.M. Gabovich, A.I. Voitenko, T. Ekino, M. S. Li, H. Szymczak, and M. Pękałła, *Adv. Cond. Matter. Phys.* **2010**, 1–40 (2009).
3. O. Fischer, M. Kugler, I. Maggio-Aprile, C. Berthod, and Ch. Renner, *Rev. Mod. Phys.* **79**(1), 353–419 (2007).
4. M. Hashimoto, I. M. Vishik, R.-H. He, T. P. Devereaux, and Z.-X. Shen, *Nat. Phys.* **10**, 483–495 (2014).
5. B. Keimer, S. A. Kivelson, M. R. Norman, S. Uchida, and J. Zaanen, *Nature* **518**(7538), 179–186 (2015).
6. K. Rossnagel, *J. Phys.: Condens. Matter* **23**(21), 213001–213025 (2011).
7. X. Zhu, Y. Cao, J. Zhang, E. W. Plummer, and J. Guo, *Proc. Nat. Ac. of Sci.* **112**(8), 2367–2371 (2015).
8. T. Wu, H. Mayaffre, S. Kramer, M. Horvatic, C. Berthier, W. N. Hardy, R. Liang, D. A. Bonn, and M.-H. Julien, *Nature* **477**(7363), 191–194 (2011).
9. J. Chang, E. Blackburn, A. T. Holmes, N. B. Christensen, J. Larsen, J. Mesot, Ruixing Liang, D. A. Bonn, W. N. Hardy, A. Watenphul, M. von Zimmermann, E. M. Forgan, and S. M. Hayden, *Nat. Phys.* **8**(12), 871–876 (2012).
10. G. Ghiringhelli, M. Le Tacon, M. Minola, S. Blanco-Canosa, C. Mazzoli, N. B. Brookes, G. M. De Luca, A. Frano, D. G. Hawthorn, F. He, T. Loew, M. Moretti Sala, D. C. Peets, M. Salluzzo, E. Schierle, R. Sutarto, G. A. Sawatzky, E. Weschke, B. Keimer, and L. Braicovich, *Science* **337**(6096), 821–825 (2012).
11. E. H. da Silva Neto, P. Aynajian, A. Frano, R. Comin, E. Schierle, E. Weschke, A. Gyenis, J. Wen, J. Schneeloch, Z. Xu, S. Ono, G. Gu, M. Le Tacon, and A. Yazdani, *Science* **343**(6169), 393–396 (2014).
12. R. Comin, A. Frano, M.M. Yee, Y. Yoshida, H. Eisaki, E. Schierle, E. Weschke, R. Sutarto, F. He, A. Soumyanarayanan, et al., *Science* **343**(6169), 390–392 (2014).
13. W. Tabis, Y. Li, M. Le Tacon, L. Braicovich, A. Kreyssig, M. Minola, G. Dellea, E. Weschke, M. J. Veit, M. Ramazanoglu, A. I. Goldman, T. Schmitt, G. Ghiringhelli, N. Barišić, M. K. Chan, C. J. Dorow, G. Yu, X. Zhao, B. Keimer, and M. Greven, *Nat. Commun.* **5** (2014).
14. E. H. da Silva Neto, R. Comin, F. He, R. Sutarto, Y. Jiang, R. L. Greene, G. A. Sawatzky, and A. Damascelli, *Science* **347**(6219), 282–285 (2015).
15. T. Kiss, T. Yokoya, A. Chainani, S. Shin, T. Hanaguri, M. Nohara, and H. Takagi, *Nat. Phys.* **3**(10), 720–725 (2007).
16. K. E. Wagner, E. Morosan, Y. S. Hor, J. Tao, Y. Zhu, T. Sanders, T. M. McQueen, H. W. Zandbergen, A. J. Williams, D. V. West, and R. J. Cava, *Phys. Rev. B* **78**, 104520 (2008).

17. K. C. Rahnejat, C. A. Howard, N. E. Shuttleworth, S. R. Schofield, K. Iwaya, C. F. Hirjibehedin, Ch. Renner, G. Aeppli, and M. Ellerby, *Nat. Commun.* **2** (2011).
18. I. Zeljkovic, Z. Xu, J. Wen, G. Gu, R. S. Markiewicz, and J. E. Hoffman, *Science* **337**(6092), 320–323 (2012).
19. C. J. Arguello, S. P. Chockalingam, E. P. Rosenthal, L. Zhao, C. Gutiérrez, J. H. Kang, W. C. Chung, R. M. Fernandes, S. Jia, A. J. Millis, R. J. Cava, and A. N. Pasupathy, *Phys. Rev. B* **89**, 235115 (2014).
20. H. Alloul, J. Bobroff, M. Gabay, and P. J. Hirschfeld, *Rev. Mod. Phys.* **81**, 45–108 (2009).
21. J.C. Davis, *Acta physica Polonica. A* **104**(3-4), 193–204 (2003).
22. J. E. Hoffman, K. McElroy, D.-H. Lee, K. M Lang, H. Eisaki, S. Uchida, and J. C. Davis, *Science* **297**(5584), 1148–1151 (2002).
23. K. McElroy, R. W. Simmonds, J. E. Hoffman, D.-H. Lee, J. Orenstein, H. Eisaki, S. Uchida, and J. C. Davis, *Nature* **422**(6932), 592–596 (2003).
24. T. Hanaguri, C. Lupien, Y. Kohsaka, D.H. Lee, M. Azuma, M. Takano, H. Takagi, and J.C. Davis, *Nature* **430**(7003), 1001–1005 (2004).
25. C. J. Arguello, E. P. Rosenthal, E. F. Andrade, W. Jin, P. C. Yeh, N. Zaki, S. Jia, R. J. Cava, R. M. Fernandes, A. J. Millis, T. Valla, R. M. Osgood, and A. N. Pasupathy, *Phys. Rev. Lett.* **114**, 037001 (2015).
26. Q. H. Wang, K. Kalantar-Zadeh, A. Kis, J. N. Coleman, and M. S. Strano, *Nat. Nanotechnol.* **7**, 699–712 (2012).
27. P. M. Koenraad and M. E Flatté, *Nat. Mater.* **10**(2), 91–100 (2011).
28. K. S. Novoselov, D. Jiang, F. Schedin, T. J. Booth, V. V. Khotkevich, S. V. Morozov, and A. K. Geim, *Proc. Nat. Acad. Sci.* **102**(30), 10451–10453 (2005).
29. K. S. Novoselov, A. K. Geim, S. V. Morozov, D. Jiang, Y. Zhang, S. V. Dubonos, I. V. Grigorieva, and A. A. Firsov, *Science* **306**(5696), 666–669 (2004).
30. M. Chhowalla, H. S. Shin, G. Eda, L.-J. Li, Loh K. P., and H. Zhang, *Nat. Chem.* **5**, 263–275 (2013).
31. A.K. Geim and I.V. Grigorieva, *Nature* **499**(7459), 419–425 (2013).
32. J. Tersoff and D. R. Hamann, *Phys. Rev. B* **31**, 805–813 (1985).
33. F. Di Salvo, D. Moncton, and J. Waszczak, *Phys. Rev. B* **14**(10), 4321–4328 (1976).
34. J. A. Wilson, *Solid State Commun.* **22**, 551–553 (1977).
35. H. P. Hughes, *J Phys C: Solid State Phys.* **10**, 319–323 (1977).
36. M. H. Whangbo and E. Canadell, *J. Am. Chem. Soc.* **114**(24), 9587–9600 (1992).
37. J. van Wezel, P. Nahai-Williamson, and S. S Saxena, *Phys. Rev. B* **81**(16), 165109 (2010).
38. B. S. Dennis J. W. G. Bos Y. Onose T. Klimczuk A. P. Ramirez N. P. Ong E. Morosan, H. W. Zandbergen and R. J. Cava, *Nat. Phys.* **2**, 544 (2006).
39. B. Hildebrand, C. Didiot, A. M. Novello, G. Monney, A. Scarfato, A. Ubaldini, H. Berger, D. R. Bowler, C. Renner, and P. Aebi, *Phys. Rev. Lett.* **112**, 197001 (2014).
40. A. M. Novello, B. Hildebrand, A. Scarfato, C. Didiot, G. Monney, A. Ubaldini, H. Berger, D. R. Bowler, P. Aebi, and Ch. Renner, *Phys. Rev. B* **92**, 081101(R) (2015).
41. J. Ishioka, T. Fujii, K. Katono, K. Ichimura, T. Kurosawa, M. Oda, and S. Tanda, *Phys. Rev. B* **84**(24), 245125 (2011).
42. G. Grüner and A. Zettl, *Physics Reports* **119**(3), 117 – 232 (1985).
43. G. Grüner, *Rev. Mod. Phys.* **60**, 1129–1181 (1988).
44. C. Berthod, *Applications of the Many-Body Formalism in Condensed-Matter Physics*. (University of Geneva (lecture note), 2015).

45. M. Tinkham, *Introduction to Superconductivity: Second Edition*. (Dover Publications 2004).
46. Rudolf Ernst Peierls, *Quantum theory of solids*. (Clarendon 1955).
47. P. Aebi, Th. Pillo, H. Berger, and F. Lévy, *J. Electron Spectrosc. Relat. Phenom.* **117-118**(0), 433 – 449 (2001).
48. M.J. Rice and S. Strässler, *Solid State Commun.* **13**(1), 125 – 128 (1973).
49. M. D. Johannes and I. I. Mazin, *Phys. Rev. B* **77**, 165135 (2008).
50. S. K. Chan and V. Heine, *J. Phys. F: Met. Phys.* **3**(4), 795 (1973).
51. M. Calandra and F. Mauri, *Phys. Rev. Lett.* **106**, 196406 (2011).
52. F. Weber, S. Rosenkranz, J.-P. Castellan, R. Osborn, R. Hott, R. Heid, K.-P. Bohnen, T. Egami, A. H. Said, and D. Reznik, *Phys. Rev. Lett.* **107**, 107403 (2011).
53. W. L. McMillan, *Phys. Rev. B* **12**, 1187–1196 (1975).
54. W. L. McMillan, *Phys. Rev. B* **16**, 643–650 (1977).
55. J. Dai, E. Calleja, J. Alldredge, X. Zhu, L. Li, W. Lu, Y. Sun, T. Wolf, H. Berger, and K. McElroy, *Phys. Rev. B* **89**, 165140 (2014).
56. J. Bardeen, L. N. Cooper, and J. R. Schrieffer, *Phys. Rev.* **108**, 1175–1204 (1957).
57. F. Steglich, J. Aarts, C. D. Bredl, W. Lieke, D. Meschede, W. Franz, and H. Schäfer, *Phys. Rev. Lett.* **43**, 1892–1896 (1979).
58. D. Jerome, A. Mazaud, M. Ribault, and K. Bechgaard, *J. Physique Lett.* **41**(4), 95–98 (1980).
59. J.G. Bednorz and K.A. Müller, *Zeitschrift für Physik B Condensed Matter* **64**(2), 189–193 (1986).
60. Y. Maeno, H. Hashimoto, K. Yoshida, S. Nishizaki, T. Fujita, J. G. Bednorz, and F. Lichtenberg, *Nature* **372**(6506), 532–534 (1994).
61. S. L. Bud'ko, G. Lapertot, C. Petrovic, C. E. Cunningham, N. Anderson, and P. C. Canfield, *Phys. Rev. Lett.* **86**, 1877–1880 (2001).
62. H. Takahashi, K. Igawa, K. Arii, Y. Kamihara, M. Hirano, and H. Hosono, *Nature* **453**(7193), 376–378 (2008).
63. A.P. Drozdov, M.I. Eremets, and I.A. Troyan, *arXiv preprint arXiv:1412.0460* (2014).
64. M. Nuñez Regueiro, J. L. Tholence, E. V. Antipov, J. J. Capponi, and M. Marezio, *Science* **262**(5130), 97–99 (1993).
65. R. J. Creswich C. P. Poole Jr., H. A. Farach, *Superconductivity*. (Academic Press Inc. 1995).
66. Z.-X. Shen, D. S. Dessau, B. O. Wells, D. M. King, W. E. Spicer, A. J. Arko, D. Marshall, L. W. Lombardo, A. Kapitulnik, P. Dickinson, S. Doniach, J. DiCarlo, T. Loeser, and C. H. Park, *Phys. Rev. Lett.* **70**, 1553–1556 (1993).
67. T. Timusk and B. Statt, *Rep. Prog. Phys.* **62**(1), 61 (1999).
68. J.L. Tallon and J.W. Loram, *Physica C: Supercond.* **349**, 53 – 68 (2001).
69. I. M. Vishik, M. Hashimoto, R.-H. He, W.-S. Lee, F. Schmitt, D. Lu, R. G. Moore, C. Zhang, W. Meevasana, T. Sasagawa, S. Uchida, K. Fujita, S. Ishida, M. Ishikado, Y. Yoshida, H. Eisaki, Z. Hussain, T. P. Devereaux, and Z.-X. Shen, *Proc. Nat. Acad. Sci.* **109**(45), 18332–18337 (2012).
70. Q. Chen, J. Stajic, S. Tan, and K. Levin, *Phys. Rep.* **412**(1), 1 – 88 (2005).
71. V. B. Geshkenbein, L. B. Ioffe, and A. I. Larkin, *Phys. Rev. B* **55**, 3173–3180 (1997).
72. V. J. Emery and S. A. Kivelson, *Nature* **374**(6521), 434–437 (1995).
73. Y. Wang, S. Ono, Y. Onose, G. Gu, Yoichi Ando, Y. Tokura, S. Uchida, and N. P. Ong, *Science* **299**(5603), 86–89 (2003).

74. F. Rullier-Albenque, R. Tourbot, H. Alloul, P. Lejay, D. Colson, and A. Forget, *Phys. Rev. Lett.* **96**, 067002 (2006).
75. A. Kanigel, U. Chatterjee, M. Randeria, M. R. Norman, G. Koren, K. Kadowaki, and J. C. Campuzano, *Phys. Rev. Lett.* **101**, 137002 (2008).
76. H.-B. Yang, J. D. Rameau, P. D. Johnson, T. Valla, A. Tsvelik, and G. D. Gu, *Nature* **456**(7218), 77–80 (2008).
77. P. A. Lee, N. Nagaosa, and X.-G. Wen, *Rev. Mod. Phys.* **78**, 17–85 (2006).
78. J.M. Tranquada, B.J. Sternlieb, J.D. Axe, Y. Nakamura, and S. Uchida, *Nature* **375**(6532), 561–563 (1995).
79. V. J. Emery, S. A. Kivelson, and J. M. Tranquada, *Proc. Nat. Acad. Sci.* **96**(16), 8814–8817 (1999).
80. P. Abbamonte, A. Rusydi, S. Smadici, G.D. Gu, G.A. Sawatzky, and D.L. Feng, *Nat. Phys.* **1**(3), 155–158 (2005).
81. T. P. Croft, C. Lester, M. S. Senn, A. Bombardi, and S. M. Hayden, *Phys. Rev. B* **89**, 224513 (2014).
82. C. Howald, H. Eisaki, N. Kaneko, and A. Kapitulnik, *Proc. Nat. Acad. Sci.* **100**(17), 9705–9709 (2003).
83. S. A. Kivelson, I. P. Bindloss, E. Fradkin, V. Oganesyan, J. M. Tranquada, A. Kapitulnik, and C. Howald, *Rev. Mod. Phys.* **75**, 1201–1241 (2003).
84. J. A. Robertson, S. A. Kivelson, E. Fradkin, A. C. Fang, and A. Kapitulnik, *Phys. Rev. B* **74**, 134507 (2006).
85. W. D. Wise, M. C. Boyer, Kamalesh Chatterjee, Takeshi Kondo, T. Takeuchi, H. Ikuta, Yayu Wang, and E. W. Hudson, *Nat. Phys.* **4**, 696–699 (2008).
86. M. Vojta, *Adv. Phys.* **58**(6), 699–820 (2009).
87. C. V. Parker, P. Aynajian, E. H. da Silva Neto, A. Pushp, S. Ono, J. Wen, Z. Xu, G. Gu, and A. Yazdani, *Nature* **468**(7324), 677–680 (2010).
88. T. Wu, H. Mayaffre, M. Krämer, S. andHorvaticč, C. Berthier, P. L. Kuhns, A. P. Reyes, R. Liang, W. N. Hardy, D. A. Bonn, and M.-H. Julien, *Nat. Commun.* **4**, – (2013).
89. A. J. Achkar, R. Sutarto, X. Mao, F. He, A. Frano, S. Blanco-Canosa, M. Le Tacon, G. Ghiringhelli, L. Braicovich, M. Minola, M. Moretti Sala, C. Mazzoli, Ruixing Liang, D. A. Bonn, W. N. Hardy, B. Keimer, G. A. Sawatzky, and D. G. Hawthorn, *Phys. Rev. Lett.* **109**, 167001 (2012).
90. M. Le Tacon, A. Bosak, S. M. Souliou, G. Dellea, T. Loew, R. Heid, K-P. Bohnen, G. Ghiringhelli, M. Krisch, and B. Keimer, *Nat. Phys.* **10**(1), 52–58 (2014).
91. D. LeBoeuf, S. Kramer, W. N. Hardy, R. Liang, D. A. Bonn, and C. Proust, *Nat. Phys.* **9**(2), 79–83 (2013).
92. T. Wu, H. Mayaffre, S. Krämer, M. Horvatic, C. Berthier, W.N. Hardy, R. Liang, D.A. Bonn, and M.H. Julien, *arXiv preprint arXiv:1404.1617* (2014).
93. R. Comin, R. Sutarto, E. H. da Silva Neto, L. Chauviere, R. Liang, W. N. Hardy, D. A. Bonn, F. He, G. A. Sawatzky, and A. Damascelli, *Science* **347**(6228), 1335–1339 (2015).
94. D. Jariwala, V. K. Sangwan, L. J. Lauhon, T. J. Marks, and M. C. Hersam, *ACS Nano* **8**(2), 1102–1120 (2014).
95. X. Xu, W. Yao, Di Xiao, and T. F. Heinz, *Nat. Phys.* **10**(5), 343–350 (2014).
96. Yoffe A. D. Wilson J. A., *Adv. Phys.* **18**(73), 193–335 (1969).
97. R. B. Murray and R. H. Williams, *Philosophical Magazine* **29**(3), 473–492 (1974).
98. J.A. Wilson, F.J. Di Salvo, and S. Mahajan, *Adv. Phys.* **24**(2), 117–201 (1975).
99. F. Lévy, *Intercalated Layered Materials*. (Springer & Business Media 1979).

100. R.V. Coleman, B. Giambattista, P.K. Hansma, A. Johnson, W.W. McNairy, and C.G. Slough, *Adv. Phys.* **37**(6), 559–644 (1988).

101. K.-W. Benz and W. Neumann, *Introduction to Crystal Growth and Characterization*. (Wiley-VCH 2014).

102. K. Momma and F. Izumi, *J. Appl. Crystallogr.* **44**, 1272–1276 (2011).

103. K. F. Mak, C. Lee, J. Hone, J. Shan, and T. F. Heinz, *Phys. Rev. Lett.* **105**, 136805 (2010).

104. H. Cercellier, C. Monney, F. Clerc, C. Battaglia, L. Despont, M. G. Garnier, H. Beck, P. Aebi, L. Patthey, H. Berger, and L. Forró, *Phys. Rev. Lett.* **99**(14), 146403 (2007).

105. J. F. Zhao, H. W. Ou, G. Wu, B. P. Xie, Y. Zhang, D. W. Shen, J. Wei, L. X. Yang, J. K. Dong, M. Arita, H. Namatame, M. Taniguchi, X. H. Chen, and D. L. Feng, *Phys. Rev. Lett.* **99**(14), 146401 (2007).

106. J. Jinwon, J. Jinhwan, N. Han-Jin, B. K. Sung, and H.-D. Kim, *Phys. C: Superconductivity* **470**, S648–S650 (2010).

107. J. C. E. Rasch, T. Stemmler, B. Müller, L. Dudy, and R. Manzke, *Phys. Rev. Lett.* **101**(23), 237602 (2008).

108. P. P. Altermatt, A. Schenk, F. Geelhaar, and G. Heiser, *J. Appl. Phys.* **93**(3), 1598–1604 (2003).

109. N.W. Ashcroft and N.D. Mermin, *Solid State Physics*. (Holt, Rinehart and Winston 1976).

110. K. C. Woo, F. C. Brown, W. L. McMillan, R. J. Miller, M. J. Schaffman, and M. P. Sears, *Phys. Rev. B* **14**, 3242–3247 (1976).

111. J. Ishioka, Y. Liu, K. Shimatake, T. Kurosawa, K. Ichimura, Y. Toda, M. Oda, and S. Tanda, *Phys. Rev. Lett.* **105**, 176401 (2010).

112. J. Ishioka, Y.H. Liu, K. Shimatake, T. Kurosawa, K. Ichimura, Y. Toda, M. Oda, and S. Tanda, *Phys. B: Condensed Matter* **405**(11), S214–S216 (2010).

113. J. van Wezel, *Europhys. Lett.* **96**(6), 67011 (2011).

114. J. van Wezel, P. Nahai-Williamson, and S. S. Saxena, *Phys. Rev. B* **83**(2), 024502 (2011).

115. J. van Wezel, *Phys. B: Condensed Matter* **407**(11), 1779–1782 (2012).

116. M. Porer, U. Leierseder, J-M Ménard, H. Dachraoui, L. Mouchliadis, I.E. Perakis, U. Heinzmann, J. Demsar, K. Rossnagel, and R. Huber, *Nat. Mater.* **13**(9), 857–861 (2014).

117. C. Monney, H. Cercellier, F. Clerc, C. Battaglia, E. Schwier, C. Didiot, M. Garnier, H. Beck, P. Aebi, H. Berger, L. Forró, and L. Patthey, *Phys. Rev. B* **79**(4), 45116 (2009).

118. A. Zunger and A. J. Freeman, *Phys. Rev. B* **17**, 1839–1842 (1978).

119. C. M. Fang, R. A. de Groot, and C. Haas, *Phys. Rev. B* **56**, 4455–4463 (1997).

120. E. Pehlke, W. Schattke, O. Anderson, R. Manzke, and M. Skibowski, *Phys. Rev. B* **41**, 2982–2990 (1990).

121. R. Z. Bachrach, M. Skibowski, and Frederick C. Brown, *Phys. Rev. Lett.* **37**, 40–42 (1976).

122. O. Anderson, R. Manzke, and M. Skibowski, *Phys. Rev. Lett.* **55**, 2188–2191 (1985).

123. C. H. Chen, W. Fabian, F. C. Brown, K. C. Woo, B. Davies, B. DeLong, and A. H. Thompson, *Phys. Rev. B* **21**, 615–624 (1980).

124. N. G. Stoffel, S. D. Kevan, and N. V. Smith, *Phys. Rev. B* **31**, 8049–8055 (1985).

125. M. M. Traum, G. Margaritondo, N. V. Smith, J. E. Rowe, and F. J. Di Salvo, *Phys. Rev. B* **17**, 1836–1838 (1978).

126. G. Margaritondo, C. M. Bertoni, J. H. Weaver, F. Lévy, N. G. Stoffel, and A. D. Katnani, *Phys. Rev. B* **23**, 3765–3769 (1981).

127. K. Rossnagel, L. Kipp, and M. Skibowski, *Phys. Rev. B* **65**, 235101 (2002).

128. C. Monney, E. F. Schwier, M. G. Garnier, N. Mariotti, C. Didiot, H. Cercellier, J. Marcus, H. Berger, A. N. Titov, H. Beck, and P. Aebi, *New J. Phys.* **12**(12), 125019 (2010).

129. T. Kidd, T. Miller, M. Chou, and T.-C. Chiang, *Phys. Rev. Lett.* **88**, 226402 (2002).

130. A. F. Kusmartseva, B. Sipos, H. Berger, L. Forró, and E. Tutiš, *Phys. Rev. Lett.* **103**(23), 236401 (2009).

131. Y. I. Joe, X. M. Chen, P. Ghaemi, K. D. Finkelstein, G. A. de la Pena, Y. Gan, J. C. T. Lee, S. Yuan, J. Geck, G. J. MacDougall, T. C. Chiang, S. L. Cooper, E. Fradkin, and P. Abbamonte, *Nat. Phys.* **10**(6), 421–425 (2014).

132. M. Sasaki, A. Ohnishi, T. Kikuchi, M. Kitaura, Ki-Seok Kim, and Heon-Jung Kim, *Phys. Rev. B* **82**, 224416 (2010).

133. M. Sasaki, A. Ohnishi, T. Kikuchi, M. Kitaura, K. Shimada, and H.-J. Kim, *J. Low Temp. Phys.* **161**(3-4), 375–386 (2010).

134. Y. J. Uemura, *Nat. Mater.* **8**(4), 253–255 (2009).

135. G. Wu, H. X. Yang, L. Zhao, X. G. Luo, T. Wu, G. Y. Wang, and X. H. Chen, *Phys. Rev. B* **76**, 024513 (2007).

136. A. A. Titov, A. I. Merentsov, A. E. Kar'kin, A. N. Titov, and V.V. Fedorenko, *Metals And Superconductors* **51**, 230–233 (2009).

137. A.A. Titov, A.N. Titov, O.V. Bushkova, and V.A. Tsurin, *Phys. Solid State* **52**(8), 1577–1584 (2010).

138. A.S. Shkvarin, Yu M. Yarmoshenko, N.A. Skorikov, A.A. Titov, and A.N. Titov, *J. Exp. Theor. Phys.* **114**(2), 324–328 (2012).

139. A.S. Shkvarin, Yu.M. Yarmoshenko, M.V. Yablonskikh, N.A. Skorikov, A.I. Merentsov, M.V. Kuznetsov, and A.N. Titov, *J. Phys. Chem. Solids* **73**(12), 1562 – 1565 (2012).

140. R. A. Jishi and H. M. Alyahyaei, *Phys. Rev. B* **78**(14), 144516 (2008).

141. A. D. Hillier, P. Manuel, D. T. Adroja, J. W. Taylor, A. K. Azad, and J. T. S. Irvine, *Phys. Rev. B* **81**(9), 092507 (2010).

142. G. Li, W. Z. Hu, J. Dong, D. Qian, D. Hsieh, M. Z. Hasan, E. Morosan, R. J. Cava, and N. L. Wang, *Phys. Rev. Lett.* **99**(16), 167002 (2007).

143. P. Husaníková, J. Kačmarčik, V. Cambel, and G. Karapetrov, *Solid State Commun.* **151**(3), 227 – 228 (2011).

144. C. H. Wang, G. Y. Wang, Z. H. B. Song, Feng, S. Y. Li, and X. H. Chen, *Phys. Rev. B* **72**(13), 132506 (2005).

145. E. Morosan, Lu Li, N. P. Ong, and R. J. Cava, *Phys. Rev. B* **75**, 104505 (2007).

146. M. Zaberchik, K. Chashka, L. Patlgan, A. Maniv, C. Baines, P. King, and A. Kanigel, *Phys. Rev. B* **81**, 220505 (2010).

147. D. Qian, D. Hsieh, L. Wray, E. Morosan, N. L. Wang, Y. Xia, R. J. Cava, and M. Z. Hasan, *Phys. Rev. Lett.* **98**(11), 117007 (2007).

148. D. Qian, D. Hsieh, L. Wray, Y. Xia, R.J. Cava, E. Morosan, and M.Z. Hasan, *Phys. B* **403**, 1002 (2008).

149. M. Iavarone, R. Di Capua, X. Zhang, M. Golalikhani, S. A. Moore, and G. Karapetrov, *Phys. Rev. B* **85**, 155103 (2012).

150. J. Kačmarčík, Z. Pribulová, V. Pal?uchová, P. Szabó, P. Husaníková, G. Karapetrov, and P. Samuely, *Phys. Rev. B* **88**(2), 020507 (2013).

151. P. Husaníková, J. Fedor, J. Dérer, J. Šoltỳs, V. Cambel, M. Iavarone, S.J. May, and G. Karapetrov, *Phys. Rev. B* **88**(17), 174501 (2013).
152. S. Y. Li, G. Wu, X. H. Chen, and Louis Taillefer, *Phys. Rev. Lett.* **99**, 107001 (2007).
153. H. Barath, M. Kim, J. F. Karpus, S. L. Cooper, P. Abbamonte, E. Fradkin, E. Morosan, and R. J. Cava, *Phys. Rev. Lett.* **100**, 106402 (2008).
154. G. Binnig and H. Rohrer, *Rev. Mod. Phys.* **59**, 615–625 (1987).
155. Y. Hasegawa and Ph. Avouris, *Phys. Rev. Lett.* **71**, 1071–1074 (1993).
156. M. F. Crommie, C. P. Lutz, and D. M. Eigler, *Nature* **363**(6429), 524–527 (1993).
157. C. J. Chen, *Phys. Rev. B* **42**(14), 8841–8857 (1990).
158. J. Bardeen, *Phys. Rev. Lett.* **6**, 57–59 (1961).
159. J. Tersoff and D. R. Hamann, *Phys. Rev. Lett.* **50**(25), 1998–2001 (1983).
160. G. Raj, *Advanced Physical Chemistry*. (Krishna Prakashan Media 1978).
161. P. A. Rock, *Chemical thermodynamics*. (University Science Books 1983).
162. S. W. Van Sciver, *Helium cryogenics*. (Springer Science & Business Media 2011).
163. R. J. Hamers, R. M. Tromp, and J. E. Demuth, *Phys. Rev. Lett.* **56**, 1972–1975 (1986).
164. H. F. Hess, R. B. Robinson, R. C. Dynes, J. M. Valles, and J. V. Waszczak, *Phys. Rev. Lett.* **62**, 214–216 (1989).
165. H. F. Hess, R. B. Robinson, and J. V. Waszczak, *Phys. Rev. Lett.* **64**, 2711–2714 (1990).
166. K. Kanisawa, M. J. Butcher, H. Yamaguchi, and Y. Hirayama, *Phys. Rev. Lett.* **86**, 3384–3387 (2001).
167. L. Petersen, Ph. Hofmann, E.W. Plummer, and F. Besenbacher, *J. Electron Spectrosc. Relat. Phenom.* **109**, 97 – 115 (2000).
168. P. T. Sprunger, L. Petersen, E. W. Plummer, E. Lægsgaard, and F. Besenbacher, *Science* **275**(5307), 1764–1767 (1997).
169. J.E. Hoffman, E.W. Hudson, K.M. Lang, V. Madhavan, H. Eisaki, S. Uchida, and J.C. Davis, *Science* **295**(5554), 466–469 (2002).
170. I. Taguchi, M. Asai, and M. Watanabe, Y .and Oka, *Physica B+C* **105**(1), 146–150 (1981).
171. P. Hohenberg and W. Kohn, *Phys. Rev.* **136**, B864–B871 (1964).
172. W. Kohn and L. J. Sham, *Phys. Rev.* **140**, A1133–A1138 (1965).
173. G. Kresse and J. Furthmüller, *Phys. Rev. B. Condens. Matter* **54**(16), 11169–11186 (1996).
174. G. Kresse and J. Hafner, *Phys. Rev. B* **47**(1), 558–561 (1993).
175. G. Kresse, *Phys. Rev. B* **59**(3), 1758–1775 (1999).
176. J. P. Perdew, K. Burke, and M. Ernzerhof, *Phys. Rev. Lett.* **77**(18), 3865–3868 (1996).
177. W.A Hofer, *Prog. Surf. Sci.* **71**(5-8), 147–183 (2003).
178. Xian-Liang Wu, Peng Zhou, and Charles M. Lieber, *Phys. Rev. Lett.* **61**, 2604–2607 (1988).
179. C. M. Lieber and X. L. Wu, *Acc. Chem. Res* **24**, 170–177 (1991).
180. G. Li, W. Z. Hu, D. Qian, D. Hsieh, M. Z. Hasan, E. Morosan, R. J. Cava, and N. L. Wang, *Phys. Rev. Lett.* **99**(2), 027404 (2007).
181. M.V. Kuznetsov, I.I. Ogorodnikov, A.S. Vorokh, A.S. Rasinkin, and A.N. Titov, *Surf. Sci.* **606**(23-24), 1760–1770 (2012).
182. A. Kikuchi and M. Tsukada, *Surf. Sci.* **326**, 195 – 207 (1995).

183. G. P. E. M. van Bakel, J. Th. M. De Hosson, and T. Hibma, *Appl. Phys. Lett.* **56**(24), 2402–2404 (1990).

184. H. Martinez, P. Azavant, and M. Loudet, *Surf. Sci.* **400**, 247 – 257 (1998).

185. C. G. Slough, B. Giambattista, A. Johnson, W. W. McNairy, C. Wang, and R. V. Coleman, *Phys. Rev. B* **37**(11), 6571–6574 (1988).

186. S. Loth, M. Wenderoth, K. Teichmann, and R.G. Ulbrich, *Solid State Communications* **145**(11-12), 551–555 (2008).

187. M.M. May, C. Brabetz, C. Janowitz, and R. Manzke, *J. Electron Spectrosc. Relat. Phenom.* **184**(3-6), 180 – 183 (2011).

188. J. Van Wezel, P. Nahai-Williamson, and S.S. Saxena, *Phys. Status Solidi (B)* **247**(3), 592–594 (2010).

189. J. A. Wilson, *Phys. Stat. Sol.* **86**(1), 11–36 (1978).

190. A. N. Titov, M. V. Kuznetsov, and a. S. Razinkin, *Phys. Sol. State* **53**(5), 1073–1077 (2011).

191. A. Soumyanarayanan, M. M. Yee, Y. He, J. van Wezel, D. J. Rahn, K. Rossnagel, E. W. Hudson, M. R. Norman, and J. E. Hoffman, *Proc. Nat. Acad. Sci.* **110**(5), 1623–1627 (2013).

192. U. Chatterjee, J. Zhao, M. Iavarone, R. Di Capua, J. P. Castellan, G. Karapetrov, C. D. Malliakas, M. G. Kanatzidis, H. Claus, J. P. C. Ruff, F. Weber, J. van Wezel, J. C. Campuzano, R. Osborn, M. Randeria, N. Trivedi, M. R. Norman, and S. Rosenkranz, *Nat. Commun.* **6**, – (2015).

193. S. E. Stoltz, H. I. Starnberg, and L. J. Holleboom, *Phys. Rev. B* **71**, 125403 (2005).

194. C. Ramírez, R. Adelung, R. Kunz, L. Kipp, and W. Schattke, *Phys. Rev. B* **71**, 035426 (2005).

195. H. Bando, Y. Miyahara, H. Enomoto, and H. Ozaki, *Surf. Sci.* **381**(2), L609–L613 (1997).

196. H. Bando, K. Koizumi, Y. Miyahara, and H. Ozaki, *J. Phys.: Condens. Matter* **12**(19), 4353 (2000).

197. K. Luna, P. M. Wu, J. S. Chen, E. Morosan, and M. R. Beasley, *Phys. Rev. B* **91**, 094509 (2015).

198. R. C. Dynes, V. Narayanamurti, and J. P. Garno, *Phys. Rev. Lett.* **41**, 1509–1512 (1978).

199. H. K. Onnes, Technical report 124c (1911).

200. W. Meissner and R. Ochsenfeld, *Naturwissenschaften* **21**(44), 787–788 (1933).

201. F. London and H. London, pages 71–88. The Royal Society (1935).

202. V.L. Ginzburg, *Teor. Fiz* **20**, 1064 (1950).

203. A.B. Pippard, *Proc. R. Soc. Lond. A* **216**(1127), 547–568 (1953).

204. A.A. Abrikosov, *Sov. Phys. - JETP (Engl. Transl.)* **5:6** (1957).

205. U. Essmann and H. Träuble, *Phys. Lett. A* **24**(10), 526 – 527 (1967).

206. W. S. Corak, B. B. Goodman, C. B. Satterthwaite, and A. Wexler, *Phys. Rev.* **96**, 1442–1444 (1954).

207. W. S. Corak, B. B. Goodman, C. B. Satterthwaite, and A. Wexler, *Phys. Rev.* **102**, 656–661 (1956).